

**UCLA**

**UCLA Electronic Theses and Dissertations**

**Title**

Excitation of Electron Cyclotron Harmonic Waves in Earth's Magnetotail

**Permalink**

<https://escholarship.org/uc/item/0jc1b2z6>

**Author**

Zhang, Xiaojia

**Publication Date**

2014

Peer reviewed|Thesis/dissertation

UNIVERSITY OF CALIFORNIA

Los Angeles

**Excitation of Electron Cyclotron Harmonic Waves  
in Earth's Magnetotail**

A dissertation submitted in partial satisfaction of the requirements

for the degree Doctor of Philosophy

in Geophysics and Space Physics

by

**Xiaojia Zhang**

2014

© Copyright by

Xiaojia Zhang

2014

ABSTRACT OF THE DISSERTATION

**Excitation of Electron Cyclotron Harmonic Waves  
in Earth's Magnetotail**

by

**Xiaojia Zhang**

Doctor of Philosophy in Geophysics and Space Physics

University of California, Los Angeles, 2014

Professor Vassilis Angelopoulos, Chair

This dissertation investigates the generation mechanism, spatial distribution and characteristics of electrostatic electron cyclotron harmonic (ECH) waves under different plasma sheet conditions, and quantifies the role of these waves in producing the diffuse aurora. THEMIS observations from five magnetotail seasons, along with ray-tracing, and electron diffusion codes have been utilized towards that goal. By modeling the wave growth and quasi-linear pitch-angle diffusion of electrons with realistic parameters for the magnetic field, loss-cone distribution and wave intensity (obtained from observations as a function of magnetotail location), we estimate the loss-cone fill ratio and the contribution of auroral energy flux from wave-induced electron precipitation. We conclude that ECH waves are the dominant driver of electron precipitation in the middle to outer magnetotail.

The dissertation of Xiaojia Zhang is approved.

Margaret G. Kivelson

Robert J. Strangeway

Richard M. Thorne

Vassilis Angelopoulos, Committee Chair

University of California, Los Angeles

2014

# TABLE OF CONTENTS

<b>1 Introduction</b>	<b>1</b>
1.1 Plasma Waves in Earth's Magnetosphere	1
1.2 Wave-particle Interactions	5
1.3 ECH Waves	7
1.4 Association with Diffuse Aurora	10
1.5 Historical Review of Studies on ECH Waves	14
1.5.1 Observational Characteristics	14
1.5.2 Excitation Mechanism	15
1.5.3 Significance to Diffuse Aurora	18
1.6 Motivation	21
1.7 Objective and Organization of the Dissertation	22
<b>2 Estimation of ECH Wave Amplitudes during Quasi-steady, Marginally Unstable State of the Plasma Sheet</b>	<b>27</b>
2.1 Introduction	28
2.2 Methodology	29
2.2.1 Modeling Electron Diffusion Using Quasi-linear Theory	29
2.2.2 Fitting Electron Distribution Function	34
2.2.3 Evaluation of Wave Amplification Using HOTRAY Ray-Tracing Code	35

2.3	Results .....	38
2.4	Summary and Discussion .....	43
<b>3</b>	<b>ECH Wave Intensification Correlated with Electron Injections and Dipolarization Fronts .....</b>	<b>47</b>
3.1	Introduction .....	48
3.2	THEMIS Database and Instrumentation .....	51
3.3	Event Selection .....	52
3.4	Statistical Results .....	62
3.5	Summary and Discussion .....	72
<b>4</b>	<b>Extent of ECH Wave Emissions.....</b>	<b>76</b>
4.1	Introduction .....	77
4.2	Database and Methodology .....	79
4.3	Observation Results on ECH Wave Extent .....	81
4.4	Modeling ECH Wave Extent under Different Magnetic Field Topologies .....	91
4.5	Summary .....	100
4.6	Discussion and Conclusion .....	101
<b>5</b>	<b>Evaluation of ECH Wave Contribution to Diffuse Aurora.....</b>	<b>105</b>
5.1	Introduction .....	106
5.2	Modeling Diffuse Aurora Precipitation .....	107

5.3	Modeling ECH Wave Scattering of Plasma Sheet Electrons .....	110
5.3.1	Spatial Distribution of ECH Waves .....	110
5.3.2	Quantifying Diffusion Coefficients .....	116
5.3.3	Modeling Electron Diffusion Using Quasi-linear Theory .....	120
5.4	Estimated Precipitation due to ECH Wave Scattering .....	123
5.5	Summary and Discussion .....	126
<b>6</b>	<b>Summary and Future Work .....</b>	<b>130</b>
6.1	Summary .....	130
6.2	Future Work .....	133
6.2.1	Parametric Study on ECH Wave Growth Rate .....	133
6.2.2	ECH Wave Excitation and Scattering in the Inner Magnetosphere .....	133
6.2.3	Improved Model of ECH Wave Scattering Plasma Sheet Electrons .....	134
<b>Appendix A Bounce-averaged Diffusion Coefficients in a Non-dipolar Magnetic Field .....</b>		<b>136</b>
<b>Appendix B HOTRAY Ray-Tracing Code .....</b>		<b>139</b>
<b>Appendix C OVATION Prime Model .....</b>		<b>143</b>
<b>BIBLIOGRAPHY .....</b>		<b>145</b>

# LIST OF FIGURES

<b>1.1</b>	Three-dimensional cutaway view of the magnetosphere .....	2
<b>1.2</b>	Survey plot of the wave spectral intensity observed on CRRES during orbit 119 .....	4
<b>1.3</b>	Global distribution of ech waves .....	9
<b>1.4</b>	Average statistical X-ray aurora as a function of geomagnetic activity .....	11
<b>1.5</b>	Diffuse aurora hemispheric energy flux for low and high solar wind driving .....	13
<b>1.6</b>	Survey of $T_e/T_H$ dependence versus $n_e/n_H$ .....	17
<b>2.1</b>	Flow chart of methodology to estimate wave amplification corresponding to the prescribed wave amplitude.....	32
<b>2.2</b>	Bounce-averaged pitch-angle and momentum diffusion coefficients due to ech waves.....	33
<b>2.3</b>	The evolution of electron distribution due to interactions with ECH waves.....	39
<b>2.4</b>	Electron PSD after diffusion fitted to subtracted bi-maxwellians and the anisotropy .....	40
<b>2.5</b>	ECH wave amplification corresponding to different wave amplitudes .....	42
<b>3.1</b>	An ECH wave event correlated with electron injections captured by THEMIS probe P3 ...	57
<b>3.2</b>	An ECH wave event correlated with DFs captured by THEMIS probe P3 .....	60
<b>3.3</b>	Distribution of ECH event duration in five categories.....	62
<b>3.4</b>	Superposed epoch analysis ECH wave events correlated with injections .....	65
<b>3.5</b>	Superposed epoch analysis of ECH wave events correlated with DFs .....	66
<b>3.6</b>	Histograms of time shift for ECH wave events relative to injections and DFs .....	68
<b>3.7</b>	Distribution of ECH event response time lags for different MLTs.....	70
<b>3.8</b>	Time delays of ECH wave onset relative to injections and DFs .....	71

<b>4.1</b>	Distribution of ECH wave occurrence rate.....	82
<b>4.2</b>	2-D spatial distribution of dual-spacecraft measurements as a function of spacecraft separation in $Z$ .....	84
<b>4.3</b>	2-D spatial distribution of dual-spacecraft measurements as a function of spacecraft separation in $Z$ (represented by $\Delta\beta/\beta$ ).....	86
<b>4.4</b>	Occurrence rate of dual-spacecraft observations of ECH waves as a function of $ \Delta Z /L$ during different plasma sheet conditions.....	88
<b>4.5</b>	Occurrence rate of ECH waves as function of $\Delta Y$ and $\Delta X$ separations during different plasma sheet conditions. ....	90
<b>4.6</b>	Schematic depicting our distributed, multi-source modeling approach for ECH wave intensity reconstruction.....	96
<b>4.7</b>	Distribution of wave power ratio as a function of distance from the source.....	97
<b>4.8</b>	$Z$ -extent of ECH waves from single-ray tracing and multiple-source modeling.....	99
<b>5.1</b>	Electron diffuse aurora energy flux distribution for low and high solar wind driving mapped to the equatorial plane.....	109
<b>5.2</b>	Distribution wave, magnetic field, and plasma parameters during ECH intervals.....	112
<b>5.3</b>	Distribution of chorus wave occurrence rate.....	114
<b>5.4</b>	Distribution of plasma parameters in the central plasma sheet.....	115
<b>5.5</b>	Distribution of latitudinal confinement of ECH waves.....	117
<b>5.6</b>	Bounce-averaged due to ECH waves in comparison with strong diffusion rate.....	119
<b>5.7</b>	Evolution of electron distribution due to interactions with ECH waves.....	122
<b>5.8</b>	Estimated electron differential energy flux within the loss cone.....	124

**5.9** Distribution of ECH wave-induced electron precipitation ..... 125

## LIST OF TABLES

<b>2.1</b>	Parameters of electron components used to model the diffused suprathermal electron phase space density for the case in Figure 2.3 .....	41
<b>2.2</b>	Assumed values of plasma sheet electron (100eV-10keV) fluxes from THEMIS observations and estimated precipitated electron energy flux for relatively quiet and active times with different diffusion extents at L=8, L=12, and L =16 .....	46
<b>3.1</b>	Number of ECH events and percentage in the each category .....	61
<b>4.1</b>	Parameters of electron components used in the HOTRAY ray-tracing code .....	93

## ACKNOWLEDGEMENTS

The work in this dissertation would not have been possible without the encouragement, support and guidance of my advisor, Prof. Vassilis Angelopoulos. I will always remember the countless hours he has spent in guiding my research and discussing scientific problems, the priceless trust and patience that helped me get through frustrations, his passion that inspired me to enjoy and appreciate the outcome, and his wisdom that cleared up my doubts and difficulties. He has also kindly imparted to me many writing and presentation skills that help a lot in scientific communications. It is a privilege to have his mentorship on my Ph.D. journey.

I really appreciate the generous help from Dr. Binbin Ni and Prof. Richard Thorne, who have aroused my interest in settling on this topic for my thesis, taught me the basics when I just started, and devoted their precious experience and expertise into my dissertation work. I would also like to thank Prof. Richard Horne, who has shared his profound knowledge and the HOTRAY code with me. This work substantially benefited from collaborations and discussions with them.

I am also very thankful to Dr. Lunjin Chen for fruitful discussions regarding wave growth and modeling, Dr. Xin Tao for elaborations on numerical modeling of multi-dimensional diffusion, Dr. Wen Li for helpful discussion on data analysis, Dr. Patrick Newell for sharing with me the OVATION Prime model and his illuminating thoughts on diffuse aurora, Dr. Andrei Runov for patient guidance of my first study on dipolarization fronts, Prof. Larry Lyons for insightful comments on my work, Dr. Jiang Liu for valuable discussions on dipolarization fronts, Dr. Xuzhi Zhou for useful skills in coding, Dr. Drew Turner for explanations on THEMIS data processing, and Dr. Christine Gabrielse for suggestions on selecting electron injections.

I am also grateful to many faculty members in UCLA (Margaret Kivelson, Richard Thorne, Robert Strangeway, George Morales, Robert McPherron, etc), who have taught me the basics of plasma physics and inspired me with their intelligence and enthusiasm. I greatly appreciate help from Ray Walker in preparing my field exam. My deep gratitude always goes to them whenever I move forward in science.

I thank many scientists for providing the tools and data used in my study. I acknowledge NASA THEMIS contract NAS5-02099 for financial support during my doctoral studies. I am grateful to John W. Bonnell and Forrest S. Mozer for use of the THEMIS EFI data. I thank Davin Larson and Robert P. Lin for use of THEMIS SST and Charles W. Carlson and James P. McFadden for use of ESA data. I am grateful to Karl-Heinz Glassmeier, Uli Auster, and Wolfgang Baumjohann for the use of FGM data provided under the lead of the Technical University of Braunschweig and for financial support through the German Ministry for Economy and Technology and the German Center for Aviation and Space (DLR) under contract 50 OC 0302. I am grateful to Patrick Cruce, Cindy Russell, Brian Kerr, Aaron Flores, and the rest of the THEMIS programmer team for helps in using these data.

I am very thankful to Judy Hohl, who has patiently helped me with her expertise in scientific writing and refined my manuscripts in all aspects (word choice, structure, format, etc).

As I reflect on my years of doctoral studies, my great appreciation goes to my good friends, especially Shanshan Li and Hairong Lai, who have accompanied me through the graduate school, supported me during good or bad times, and shared achievements and challenges in my study and my life.

I am very grateful to my parents and my brother for their long term encouragement, support and love. My final and deepest appreciation goes to my husband, whose love and support have always been the sunshine of my life.

Xiaojia Zhang

May 13th, 2014

Chapter 2 is a version of “Zhang, X.-J., V. Angelopoulos, B. Ni, R. M. Thorne, and R. B. Horne (2013), Quasi-steady, marginally unstable electron cyclotron harmonic wave amplitudes, *J. Geophys. Res. Space Physics*, 118, 3165-3172, doi:10.1002/jgra.50319”.

Chapter 3 is a version of “Zhang, X.-J., and V. Angelopoulos (2014), On the relationship of electrostatic cyclotron harmonic emissions with electron injections and dipolarization fronts, *J. Geophys. Res. Space Physics*, 119, doi:10.1002/2013JA019540”.

Chapter 4 is a version of “Zhang, X.-J., V. Angelopoulos, B. Ni, R. M. Thorne, and R. B. Horne (2014), Extent of ECH Wave Emissions in Earth's Magnetotail, *J. Geophys. Res. Space Physics*, under review”.

## VITA

- 2004-2008 Bachelor of Science in Space Physics  
School of Earth and Space Sciences, Peking University
- 2008-2010 Master of Science in Geophysics and Space Physics  
Department of Earth, Planetary and Space Sciences  
University of California, Los Angeles
- 2008-2014 Graduate Student Researcher  
Department of Earth, Planetary and Space Sciences  
University of California, Los Angeles

## PUBLICATIONS

**Zhang, X.-J.**, V. Angelopoulos, B. Ni, R. M. Thorne, and R. B. Horne (2014), Extent of ECH Wave Emissions in Earth's Magnetotail, *J. Geophys. Res. Space Physics*, under review.

**Zhang, X.-J.**, and V. Angelopoulos (2014), On the relationship of electrostatic cyclotron harmonic emissions with electron injections and dipolarization fronts, *J. Geophys. Res. Space Physics*, 119, doi:10.1002/2013JA019540.

Yao, Z.-H., W.-J. Sun, S.-Y. Fu, Z. Y. Pu, J. Liu, V. Angelopoulos, **X.-J. Zhang**, X. N. Chu, Q.-Q. Shi, R. L. Guo, Q.-G. Zong (2013), Current structures associated with dipolarization fronts, *J. Geophys. Res. Space Physics*, 118, 6980-6985, doi:10.1002/2013JA019290.

**Zhang, X.-J.**, V. Angelopoulos, B. Ni, R. M. Thorne, and R. B. Horne (2013), Quasi-steady, marginally unstable electron cyclotron harmonic wave amplitudes, *J. Geophys. Res.*, *118*, doi:10.1002/jgra.50319.

Ni, B., R. Thorne, J. Liang, V. Angelopoulos, C. Cully, W. Li, **X.-J. Zhang**, M. Hartinger, O. Le Contel, and A. Roux (2011), Global distribution of electrostatic electron cyclotron harmonic waves observed on THEMIS, *Geophys. Res. Lett.*, *38*, L17105, doi:10.1029/2011GL048793.

Runov, A., V. Angelopoulos, X.-Z. Zhou, **X.-J. Zhang**, S. Li, F. Plaschke, and J. Bonnell (2011), A THEMIS multicasestudy of dipolarization fronts in the magnetotail plasma sheet, *J. Geophys. Res.*, *116*, A05216, doi:10.1029/2010JA016316.

**Zhang, X.-J.**, V. Angelopoulos, A. Runov, X.-Z. Zhou, J. Bonnell, J. P. McFadden, D. Larson, and U. Auster (2011), Current carriers near dipolarization fronts in the magnetotail: A THEMIS event study, *J. Geophys. Res.*, *116*, A00I20, doi:10.1029/2010JA015885.

Lun Xie, **XiaoJia Zhang**, ZuYin Pu, YongFu Wang, SuiYan Fu, and QiuGang Zong (2008), Ultra low frequency waves observed by Double Star TC-1 in the plasmasphere boundary layer, *Science in China Series E: Technological Sciences*, Volume 51, Number 10, doi:10.1007/s11431-008-0263-x.

# CHAPTER 1

## Introduction

### 1.1 Plasma Waves in Earth's Magnetosphere

Earth's magnetosphere is the region in space dominated by the geomagnetic fields, but its dynamics is governed by the region's interaction with the sun. The solar wind, a stream of charged particles emitted by the sun, compresses the geomagnetic field on the dayside up to a standoff distance of about 10 earth radii ( $R_E$ ) and stretches the magnetic field on the nightside to more than 200 earth radii, creating a tail-like structure in the anti-sunward direction. This magnetotail consists of two lobes containing tenuous plasma, and a region of denser ( $\sim 0.1 \text{ cm}^{-3}$ ) and hotter ( $\sim \text{keV}$ ) sheet of plasma (the plasma sheet) sandwiched between the lobes, as illustrated in Figure 1.1. Since the magnetic field lines in each of the two lobes of the tail (the northern and the southern lobe) originates from the two opposite magnetic poles of the Earth, a region of field reversal, known as the neutral sheet, is also contained at the lobe-lobe interface, the plasma sheet. A cross-tail current flows westward, along the neutral sheet (often called the neutral sheet current, denoted by the thick dark lines in Figure 1.1) and returns eastward over the northern and southern magnetopause (tail current in Figure 1.1), which maintains the magnetic configuration of the tail.

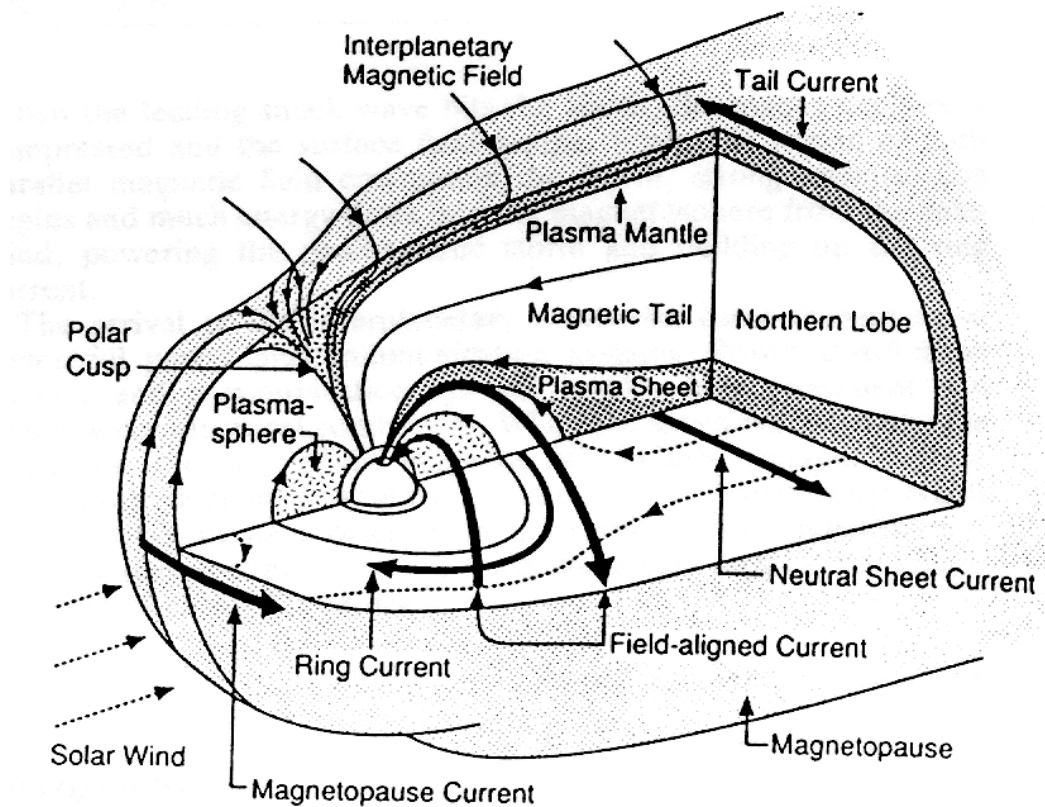


**Figure 1.1:** (After *Kivelson and Russell* [1995]) Three-dimensional cutaway view of the magnetosphere showing the major current systems (denoted by the thick lines), fields, and plasma regions.

The Earth's magnetosphere supports a variety of naturally excited and some artificial plasma waves, whose characteristics vary considerably with location. Figure 1.2 exemplifies wave electric field spectra for the different plasma waves occurring in space, as captured on single orbit of the CRRES spacecraft. The waves observed, from closer to Earth moving outwards are: Plasmaspheric hiss, an incoherent, broadband electromagnetic wave, is typically confined within the high-density plasmasphere (the high-density plasma region dominated by ionospheric plasma that remains for time-scales of days on the field lines and corotates with Earth) and plumes

(pieces of the plasmasphere that emerge towards higher radial distances due to dynamic events such that enhanced convection or magnetospheric compressions). Hiss is usually observed in the frequency range of about 100 Hz to a few kHz, which appears to be unrelated to any of the characteristic frequencies of the plasma [Meredith *et al.*, 2004]. This wave plays a significant role in creating the slot-region between the inner and outer radiation belts by pitch-angle scattering energetic electrons [Lyons and Thorne, 1973]. Whistler mode chorus is an electromagnetic emission typically observed in the frequency range from  $0.1-0.8 f_{ce}$  (where  $f_{ce}$  denotes electron gyrofrequency), with a gap at  $0.5 f_{ce}$  separating the emissions into lower band ( $0.1f_{ce} < f < 0.5f_{ce}$ ) and upper band ( $0.5f_{ce} < f < f_{ce}$ ) chorus [e.g., Tsurutani and Smith, 1974; W. Li *et al.*, 2011]. It is generated outside the plasmopause near the geomagnetic equator by cyclotron resonant interaction with suprathermal electrons that are injected into the inner magnetosphere during storms and substorms [Santolik *et al.*, 2003; Meredith *et al.*, 2002; Li *et al.*, 2009a]. Consequently, chorus is observed predominantly outside the plasmopause and is substorm-dependent, with the largest amplitudes observed during active conditions. Chorus waves play a dual role in radiation belt dynamics contributing to both acceleration and loss of relativistic electrons. Electrostatic electron cyclotron harmonic (ECH) waves are observed outside the plasmopause, in bands between the harmonics of the electron gyrofrequency ( $f_{ce}$ ), with the dominant wave power centered around  $(n+1/2)f_{ce}$  [Kennel *et al.*, 1970; Roeder and Koons, 1989; Meredith *et al.*, 2009]. These emissions have been attributed to the loss-cone instability of the ambient plasma sheet electron distribution [Ashour-Abdalla and Kennel, 1978]. ECH waves propagate almost perpendicularly to the ambient magnetic field and are confined close to the magnetic equator. They can resonate with plasma sheet electrons (in the hundreds to several thousand eV energy range), scatter these electrons into the loss cone, and lead to the diffuse

auroral precipitation. The horizontal line between 10 and 25 kHz before 1830 UT and after 0200 UT are from ground-based VLF transmitters used for navigation and communication.

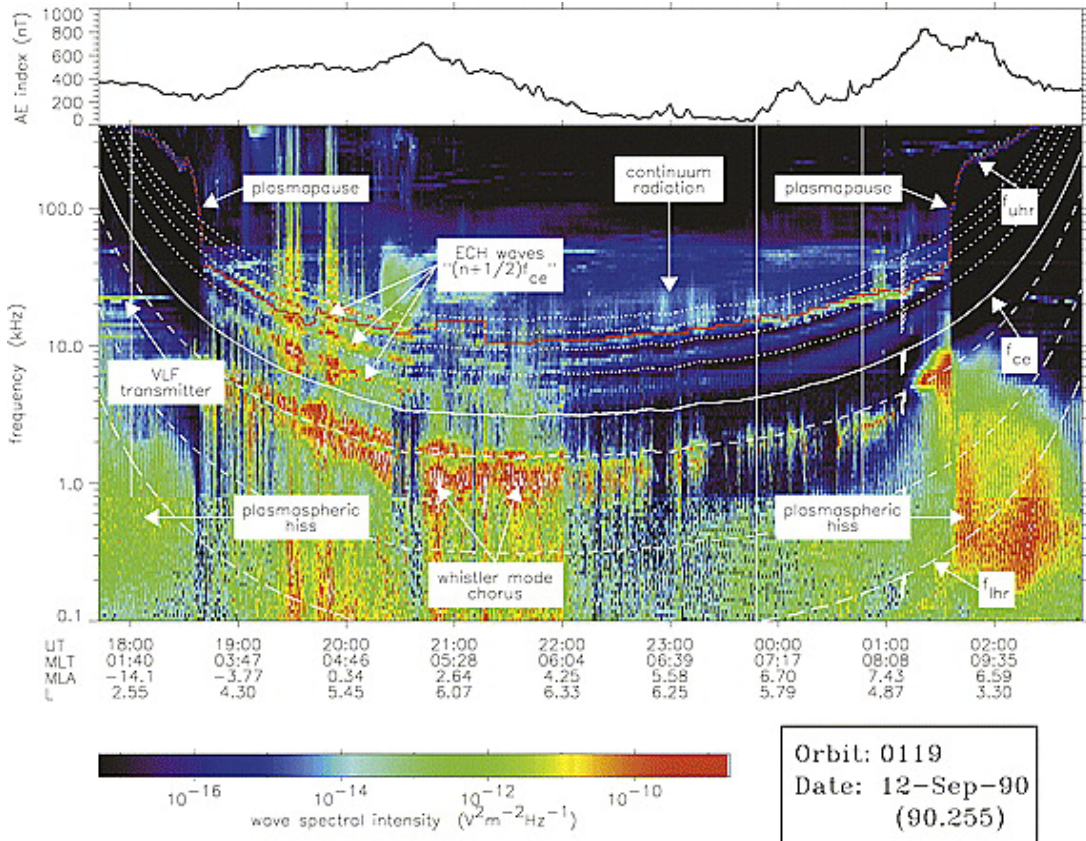


**Figure 1.2:** (After Meredith et al. [2004]) Survey plot of the wave spectral intensity observed on CRRES during orbit 119. AE index is shown on the top. Plasmaspheric hiss is the unstructured emission below a few kHz, which is primarily confined to the plasmasphere. The solid white line represents the local electron gyrofrequency  $f_{ce}$ . Dashed lines from bottom to top represent the local lower hybrid resonance frequency  $f_{LHR}$ ,  $0.1f_{ce}$ , and  $0.5f_{ce}$ . The first four harmonics of  $f_{ce}$  are represented by the dotted lines and the local upper hybrid resonance frequency  $f_{UHR}$  indicating the plasma density is shown in red.

## 1.2 Wave-particle Interactions

Trapped particles in Earth's magnetosphere undergo three types of quasi-periodic motions: gyration around magnetic field lines, bounce motion between the mirror points, and azimuthal drift around the Earth. Each periodic motion is associated with an adiabatic invariant. When the electric and magnetic field forces vary on a time scale compared to the characteristic period of a particle motion, the corresponding invariant is violated. On the other hand, spatial variations of the force field that are abrupt on a length scale comparable to the gyroradius can also violate adiabatic invariants [*Schulz and Lanzerotti, 1974*].

Pitch-angle diffusion occurs when the first adiabatic invariant (related to particle gyration) is violated, which affects particle distributions, leads to plasma instabilities, and enhances the precipitation to the ionosphere. Two collisionless scattering mechanisms have been proposed: one is the wave-particle interaction; the other is chaotic scattering in inhomogeneous magnetic field. The main distinction between these two mechanisms is that wave-particle scattering is limited by the wave intensity, while chaotic scattering only depends on the magnetic field inhomogeneity and particle energy.

The parameter that controls the degree of chaotic scattering is  $\kappa = R_c / \rho$ , where  $R_c$  is the field line radius of curvature at the equator,  $\rho$  is the particle gyroradius at the equator. The critical value corresponding to a transition from the weakly scattering condition from a strongly scattering condition is  $\kappa = 8$  [e.g., *Sergeev et al., 1983*]. Chaotic scattering in the equatorial current sheet of the magnetotail plays a crucial role in determining the scattering rate of energetic protons into the loss cone and the resultant proton auroral precipitation, during both active and

quiet geomagnetic conditions [Sergeev *et al.*, 1983; Gilson *et al.*, 2012]. Due to the much smaller gyroradius of plasma sheet electrons (the energy range of interest in this dissertation is 0.1-30 keV) compared to the field line curvature radius, however, the precipitation of diffuse electrons is attributed to wave-induced scattering.

Wave-particle interactions are important in Earth's magnetosphere, which can couple waves and particles, leading to wave growth and particle scattering, and can thus modify the dynamics of the plasma environment. When the wave frequency matches the characteristic frequency of one of the particle's periodic motions, the corresponding adiabatic invariant can be violated and particle diffusion in phase space can take place from higher to lower phase space density regions due to the random exchange of energy between waves and particles. Through such a resonance, particle populations with unstable velocity space densities (exhibiting a gradient in the direction of constant energy in the wave's frame of reference) can efficiently interact with plasma waves, leading to wave growth or damping.

For electrons, gyro-resonance requires that the Doppler-shifted frequency match an integer multiple of the electron cyclotron frequency:

$$\omega - k_{\parallel}v_{\parallel} = n\Omega_e, \quad n = 0, \pm 1, \pm 2, \dots \quad (1.1)$$

where  $k_{\parallel}$  ( $k_{\perp}$ ) is the component of the wave vector parallel (perpendicular) to the ambient magnetic field  $B_0$ ,  $\Omega_e = \left| \frac{eB_0}{\gamma m_e} \right|$  is the relativistic angular electron gyrofrequency. Landau resonance ( $n=0$ ) occurs when the electrons travel along the ambient magnetic field with the wave parallel phase speed.

Gyro-resonant interactions lead to particle diffusions in pitch angle and/or energy, potentially resulting in wave amplification or damping. Whether a wave grows or is damped is determined by the behavior of the particle distribution function near the resonant velocity, defined by Equation (1.1). For the interaction with a wave mode of a particular  $\omega$  and  $k_{\parallel}$ , diffusion curves [e.g., *Gendrin*, 1981; *Walker*, 1993; *Summers et al.*, 1998], along which the particles are constrained to move during resonant scattering, can be easily found in the velocity space,  $(v_{\parallel}, v_{\perp})$ : In the wave rest frame, moving parallel to the magnetic field with phase speed  $\omega/k_{\parallel}$  (assuming  $\omega/k_{\parallel} \ll c$ ), the particle kinetic energy is conserved; in the plasma frame, this condition becomes:

$$\left(v_{\parallel} - \frac{\omega}{k_{\parallel}}\right)^2 + v_{\perp}^2 = \text{const.} \quad (1.2)$$

The preferential direction for diffusion along this so called “diffusion surface” is dictated by the gradient in phase space density (PSD) along this surface. The net energy and pitch angle diffusion direction can thus be obtained by analyzing the particle diffusion direction relative to constant energy curves in velocity space [e.g., *Gendrin*, 1981]. Wave instability is often associated with anisotropic distributions, with a temperature anisotropy ( $T_{\perp} > T_{\parallel}$ ) or loss cone feature, both of which exhibit such gradients along the diffusion surfaces for interaction with specific wave modes.

### 1.3 ECH Waves

Electron cyclotron harmonic waves are electrostatic emissions observed in bands between the harmonics of the electron gyrofrequency ( $f_{ce}$ ), first reported by *Kennel et al.* [1970] using OGO-5

data. Their dominant wave power is centered around the odd integral half-harmonics of the electron gyrofrequency,  $(n+1/2)f_{ce}$  [Kennel *et al.*, 1970; Roeder and Koons, 1989; Meredith *et al.*, 2009]. These waves propagate in large wave normal angles with respect to ambient magnetic field,  $\sim 90^\circ$ .

Statistical studies on the global distribution of ECH waves illustrate that these waves are localized to within a few degrees of the magnetic equator, and are seen most frequently in the night and dawn regions ( $\sim 2100$ - $0600$  MLT) for  $4 < L < 10$  [Roeder and Koons, 1989; Meredith *et al.*, 2009; Ni *et al.*, 2011a], as shown in Figure 1.3. By examining the intensity of ECH emissions under different levels of geomagnetic activity, Meredith *et al.* [2009] contended that ECH waves exist in the magnetotail for various geomagnetic conditions, but intensify considerably during enhanced geomagnetic activity levels.

The excitation of ECH waves has been attributed to the loss-cone instability of the ambient, hot plasma sheet electron distribution [Ashour-Abdalla and Kennel, 1978; Horne, 1989; Horne *et al.*, 2003]. During earthward convection, Kennel *et al.* [1970] argued, plasma sheet electrons from the geomagnetic tail are expected to generate ECH waves, which can scatter these electrons (in cyclotron resonance with the waves) into the loss cone. Loss cone filling and plasma sheet electron drainage are thus consistent with the rate of earthward convection. Therefore, ECH emissions could be of great significance to the energy budget and dynamics of Earth's inner magnetosphere.

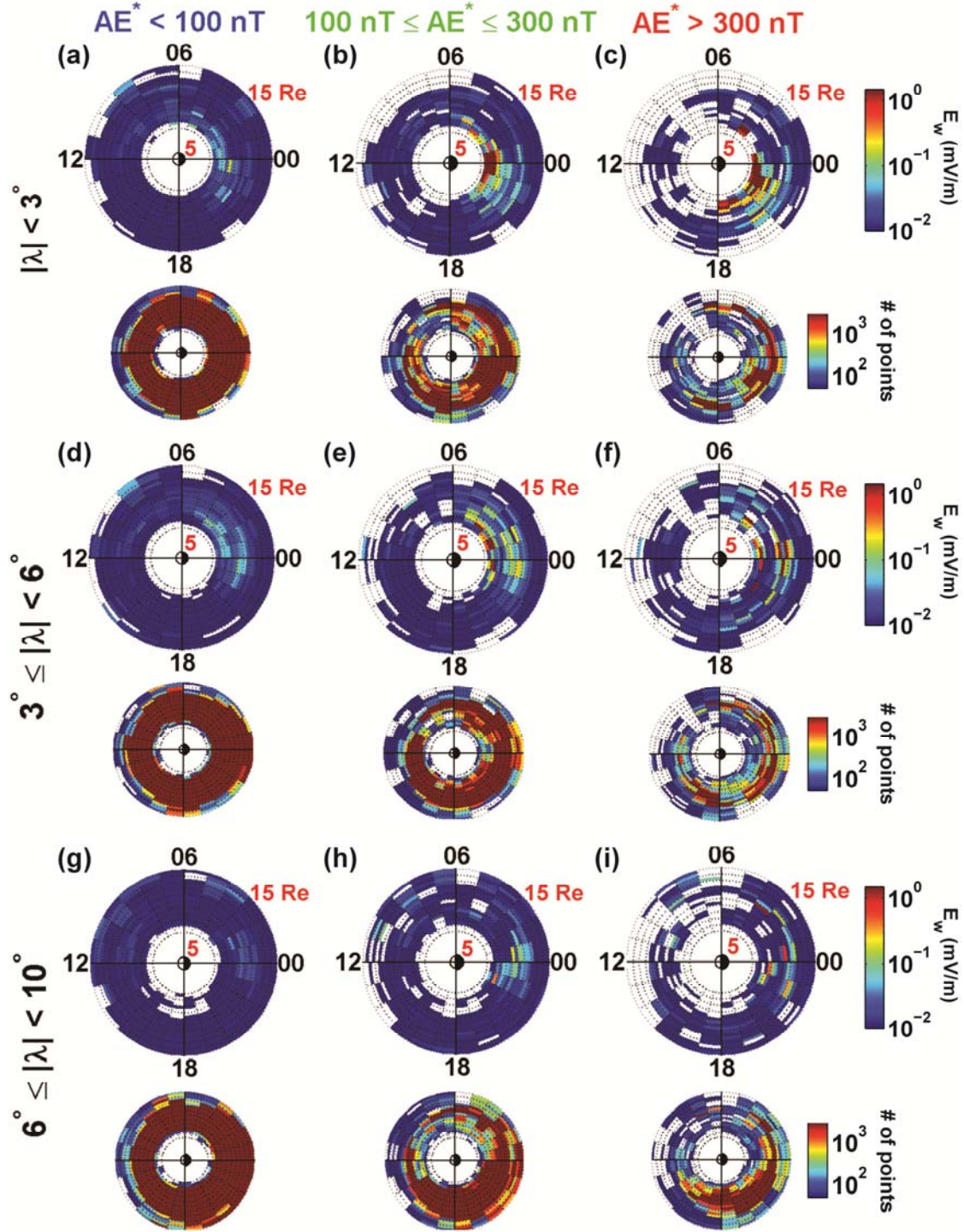


**Figure 1.3:** (After *Ni et al.* [2011a]) Global distribution of ECH waves as a function of L-shell and MLT under different geomagnetic conditions categorized by  $AE^*$  (from left to right: quiet, moderate, and active) for three specified magnetic latitude intervals: (a, b, c)  $|\lambda| < 3^\circ$ , (d, e, f)  $3^\circ$

$\leq |\lambda| < 6^\circ$ , and (g, h, i)  $6^\circ \leq |\lambda| < 10^\circ$ . The larger plots show the root-mean-square ECH wave electric field amplitudes  $E_w$  (in units of mV/m) and the smaller plots indicate the number of total samples in each bin.

## 1.4 Association with Diffuse Aurora

This dissertation mainly focuses on the generation mechanism of ECH waves, due to their potential role in supplying the dominant particle energy precipitation into the ionosphere, i.e., the diffuse aurora.

The diffuse aurora is a belt of weak emissions extending around the entire auroral oval [Horne *et al.*, 2003]. Although both ions and electrons contribute to the diffuse aurora, electron precipitations are dominant in both number flux and energy flux [Hardy *et al.*, 1985, 1989; Newell *et al.*, 2009]. So in this dissertation, we focus on diffuse electron precipitations. Using POLAR PIXIE X-ray observations, *Petrinec et al.* [1999] statistically examined the auroral intensity caused by energetic electron (2-25 keV) precipitations at different geomagnetic activities (as shown in Figure 1.4) and found out it intensifies significantly with increasing geomagnetic activity levels (denoted by AE and Dst indices).

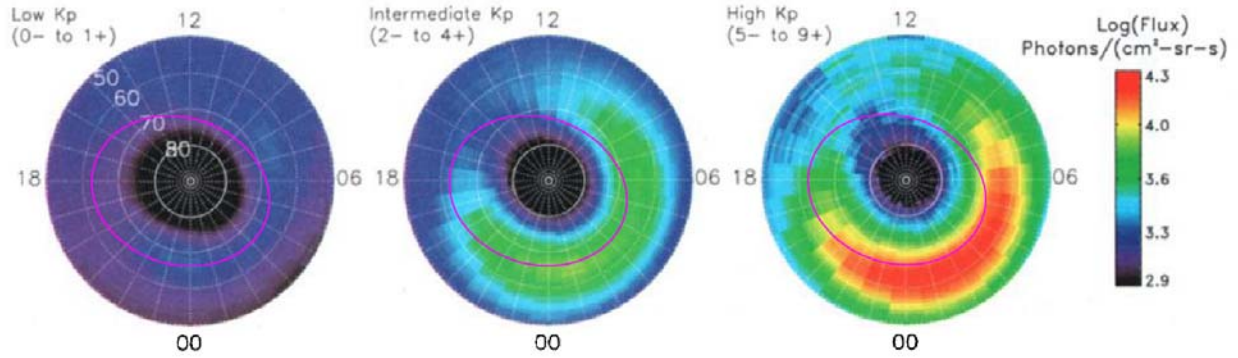


**Figure 1.4:** (Adapted from *Petrinec et al.* [1999]) Average statistical X-ray aurora (northern hemisphere) observed by PIXIE instrument onboard POLAR, as a function of geomagnetic activity as determined by the Kp index. The magenta ovals mark the latitudes which map to equatorial radial distance of  $8 R_E$  in T89 magnetic field model.

A recent statistical study on precipitation from different types of aurora, based on 11 years of DMSP observations, shows that the diffuse aurora constitutes 84% of the energy flux into the ionosphere during low solar wind driving conditions and 71% of that during high solar wind driving conditions [*Newell et al.*, 2009]. Figure 1.5 shows the pattern of electron diffuse aurora in the ionosphere. Their energy flux is enhanced by a factor of three from low to high solar wind driving conditions. The diffuse aurora extends over a latitude range of  $5^\circ$  to  $10^\circ$  and maps along the magnetic field lines from the outer radiation belts ( $L \sim 4$ ) to the entire central plasma sheet [*Meredith et al.*, 2009], with significant precipitations from middle to outer magnetotail ( $L > 8$ ) during low solar wind driving. However, as shown in Figures 1.4 and 1.5, such a contribution from middle to outer magnetotail decreases during moderate and active times. Latitudinal ranges and peak energy flux location of diffuse aurora vary with solar wind conditions and seasonal

changes [*Newell et al.*, 2009, 2010]. The dissipation is generally predominant in the pre-midnight to dawn sectors, consistent with eastward drift of plasma sheet electrons on the night side.

It is now accepted that diffuse aurora is caused by pitch-angle scattering of plasma sheet electrons in the hundreds to several thousand eV energy range into the atmospheric loss cone by wave-particle interactions [*Fontaine and Blanc*, 1983]. Both ECH waves and whistler-mode chorus resonate with electrons in this energy range [*Anderson and Maeda*, 1977]. In addition, both of these two wave modes have a similar distribution to diffuse aurora, with intensifications during active times [*Thorne et al.*, 2010]. Consequently, both chorus and ECH waves have been considered as mechanisms for plasma sheet electron precipitations. But which of these two waves is more important in driving the diffuse aurora has remained controversial for over 40 years.

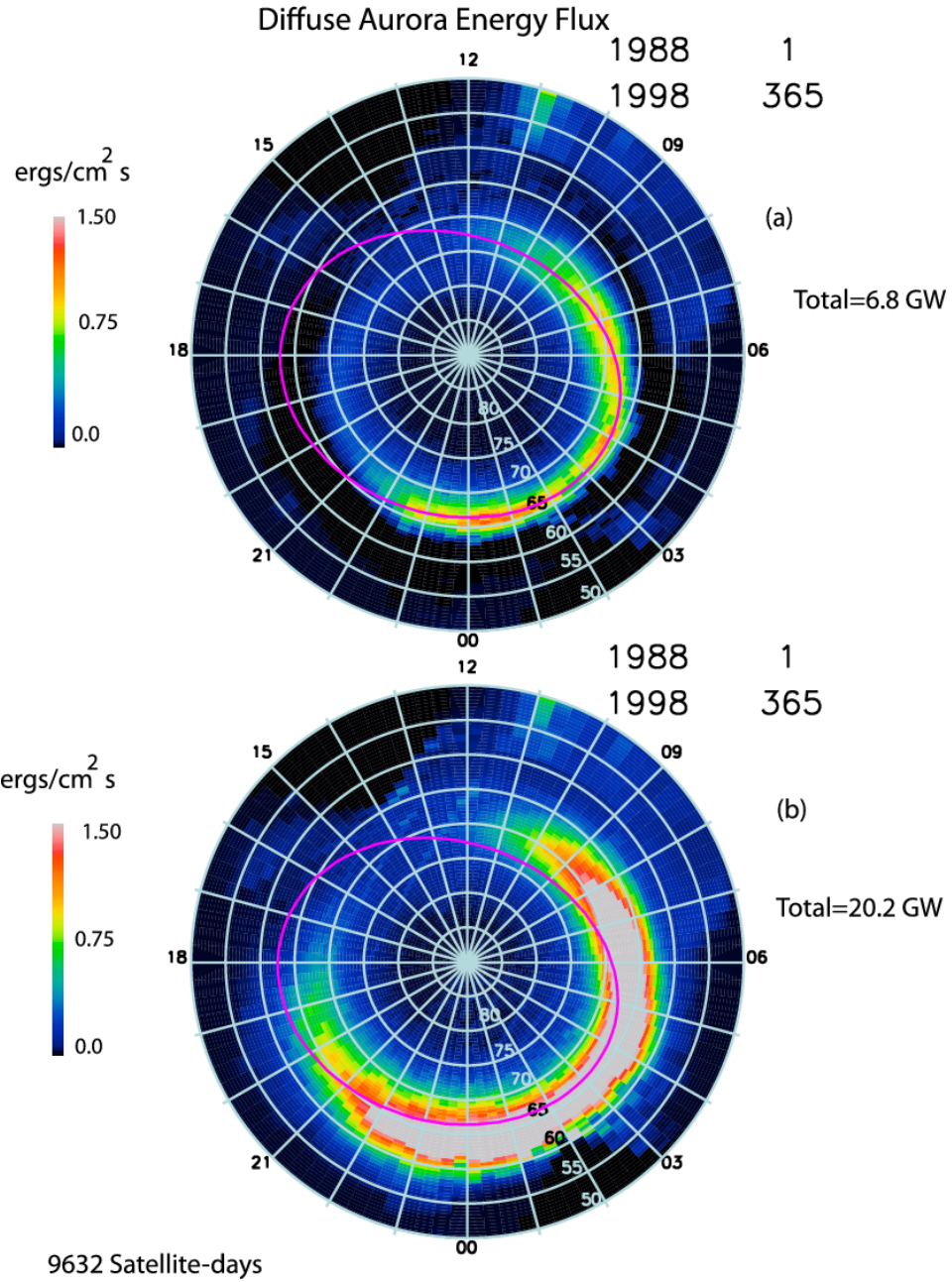


**Figure 1.5:** (Adapted from *Newell et al.* [2009]) Diffuse aurora hemispheric energy flux for (a) low and (b) high solar wind driving. The magenta ovals mark the latitudes which map to equatorial radial distance of  $8 R_E$  in T89 magnetic field model.

## 1.5 Historical Review of Studies on ECH Waves

Here I outline historically our developing understanding of the ECH wave since its first discovery. The community has focused on three questions: what are the properties and spatial distribution of these waves? what drives them unstable? what are the effects of the waves on the electrons?

### 1.5.1 Observational Characteristics

The phenomenology of ECH emissions in the Earth's magnetosphere was established directly from spacecraft observations. The electric field instrument onboard OGO-5 spacecraft, the first to operate successfully beyond the plasmopause, detected the characteristics of these emissions: electrostatic emissions with frequencies between electron cyclotron harmonics [*Kennel et al.*, 1970]. Using the SCATHA and AMPTE data, a subsequent statistical study by *Roeder and Koons* [1989] demonstrated that ECH waves usually occur in the 0300-0600 MLT sector between  $4 R_E$  and  $8 R_E$ , confined to  $\pm 10^\circ$  of the magnetic equator. But their database only adopted four equal L-shell bins and eight evenly spaced local time bins. To improve the crude spatial resolution, a recent study using CRRES wave data showed that ECH emissions are captured most frequently in the 2100-0600 MLT sector for  $4 < L < 7$ , typically confined to  $\pm 3^\circ$  of the magnetic equator [*Meredith et al.*, 2009]. This study also revealed that ECH waves intensify with increasing geomagnetic activity, with amplitudes exceeding 1 mV/m in the night-to-dawn sector. However, the CRRES data coverage was restricted within  $7 R_E$  and had a pronounced gap in the pre-noon sector for  $L > 5$ . To compensate for this, *Ni et al.* [2011a] updated the statistical distribution of ECH emissions using the THEMIS database; they found that most intense ECH waves were typically seen in the 2100-0600 MLT sector for  $L = 5-10$ , confined to  $\pm 3^\circ$  of the

magnetic equator (Figure 1.3). Beyond L=10, moderately strong (~0.1 mV/m) ECH emissions can still be observed up to L~12 (near the pre-midnight sector) during active times. For ECH emissions beyond L=12 (up to L=15), the wave amplitudes are close to the noise level. ECH waves within  $3^\circ \leq |\lambda| < 6^\circ$  are much weaker but still well above the noise level, especially for L = 5-12 near midnight.

### 1.5.2 Excitation Mechanism

In studying the ECH wave generation, theory preceded observations. Most researchers assumed a specific (unstable) distribution function and analyzed its consequences using the dispersion relation. In the absence of distribution function measurements within the loss cone, that are needed to guide further development in theory, no truly general understanding of the ECH excitation mechanism has emerged thus far. Nonetheless, these efforts provided insight into the causes of cyclotron harmonic instabilities. The “loss cone distribution” has been extensively used for instability studies, exploring parameters that are plausible in Earth’s magnetosphere. *Ashour-Abdalla and Kennel* [1978] (following *Young et al.* [1973]) implemented the basic mathematical representation for this distribution function ( $f$ ). Their model, used in most subsequent theoretical calculations of ECH waves, consists of a mixture of a cold electron plasma, with number density  $n_c$  and temperature  $T_c$ , and a hot electron plasma, with density  $n_H$  and temperature  $T_H$ , with a loss cone property:

$$f = n_c f_c + n_H f_H.$$

They represented the hot electron loss cone distribution by a sum of subtracted bi-Maxwellians:

$$f_H = \sum_i f_i,$$

where each component is expressed by:

$$f_i(v_{\parallel}, v_{\perp}) = \frac{n_i}{\pi^{2/3} \alpha_{\perp i}^2 \alpha_{\parallel i}} \exp\left(-\frac{v_{\parallel}^2}{\alpha_{\parallel i}^2}\right) \cdot \left[ \Delta_i \exp\left(-\frac{v_{\perp}^2}{\alpha_{\perp i}^2}\right) + \frac{(1-\Delta_i)}{(1-\beta_i)} \cdot \left( \exp\left(-\frac{v_{\perp}^2}{\alpha_{\perp i}^2}\right) - \exp\left(-\frac{v_{\perp}^2}{\beta_i \alpha_{\perp i}^2}\right) \right) \right]. \quad (1.3)$$

Here  $n_i$  is the electron density,  $\alpha_{\perp i}$  and  $\alpha_{\parallel i}$  are the thermal velocities perpendicular and parallel to the ambient magnetic field, and  $\beta_i$  and  $\Delta_i$  essentially determine the depth and width of the loss cone, respectively.

*Ashour-Abdalla et al.* [1979] adopted the electron distribution in Equation (1.3) to numerically calculate spatial growth rates for multi-harmonic ECH waves, demonstrating that non-convective instability (where  $\frac{\partial \omega}{\partial k_{\perp}} = 0$  coincides with  $\frac{\partial \omega}{\partial k_{\parallel}} = 0$  on the dispersion curve) is possible when the temperature ratio between cold and hot electrons ( $T_c/T_H$ ) is small enough. They conducted a parametric survey of convective growth rate dependence on  $n_c/n_H$  and  $T_c/T_H$  (results shown in Figure 1.5), showing that when  $n_c/n_H \leq 1$ , non-convective instability is possible in harmonic bands below or including the cold upper hybrid frequency, provided  $T_c/T_H$  is not too large ( $\leq 0.05$  in this case); when  $n_c/n_H > 1$ , non-convective instability is possible only in the band containing the cold upper hybrid frequency; increasing  $T_c/T_H$  removes the non-convective property eventually. *Ashour-Abdalla et al.* [1979] also suggested that when  $n_c/n_H$  becomes too

large ( $\sim 3-5$ ), the non-convective instability disappears, explaining the absence of ECH waves within the plasmasphere or near the auroral ionosphere.

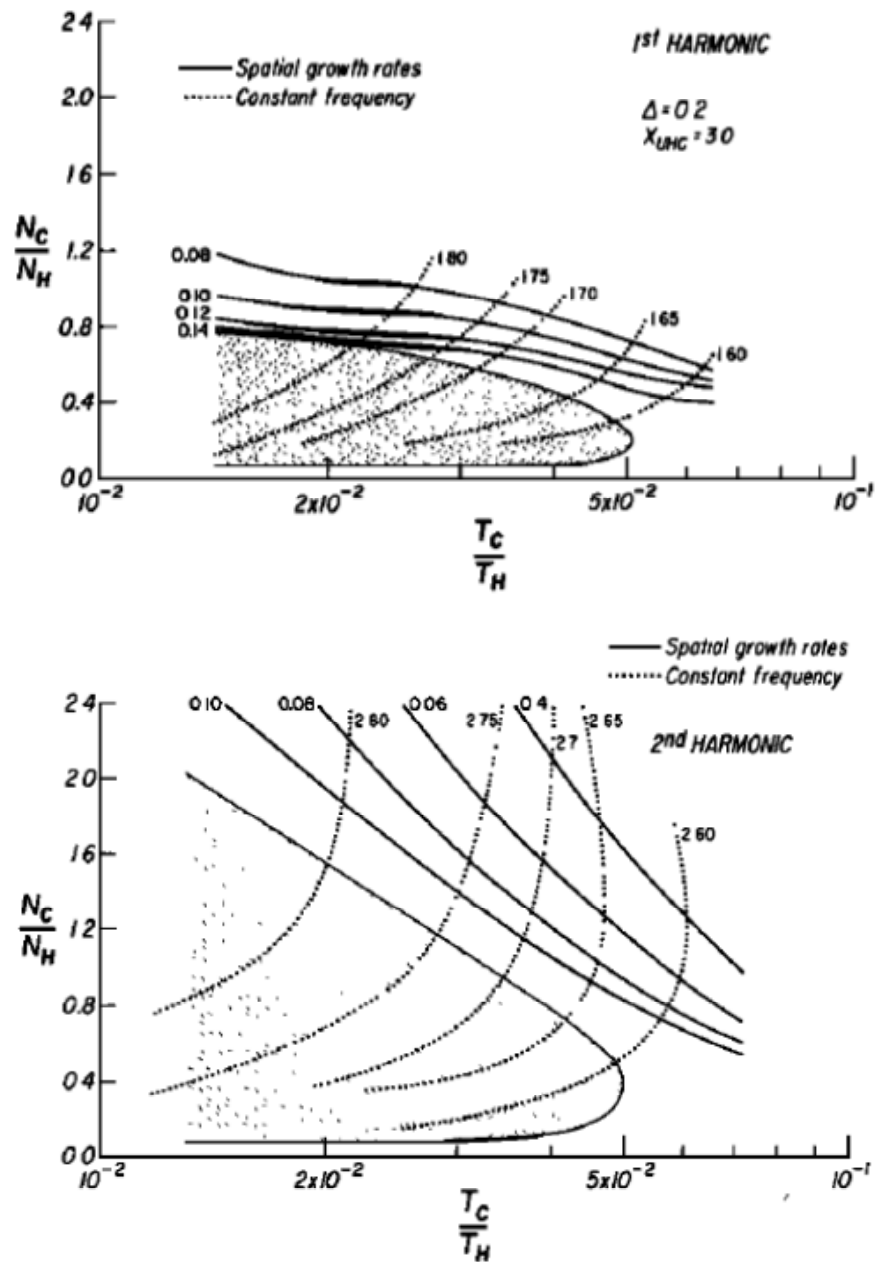


**Figure 1.6:** (Adapted from *Ashour-Abdalla et al.* [1979]) Survey of  $T_c/T_H$  dependence versus  $n_c/n_H$ . Shown here are the results of a complete parameter search. Keeping the ratio of cold upper hybrid frequency to the cyclotron frequency  $X_{UHC}=3$ , and  $\Delta=0.2$ , the entire unstable region was

calculated for each  $n_c/n_H$  and  $T_c/T_H$ , and the non-convective or fastest spatially growing modes were identified. The non-convective zones are shaded. Outside these zones, the solid lines are contours of constant maximum  $k_i\rho_H$ , the imaginary part of the spatial growth rate normalized to the hot electron cyclotron radius  $\rho_H$ . The dotted lines show the frequencies of the fastest growing or non-convective modes. The first harmonic is the top panel, and the second is the bottom one. The third harmonic always remained convective. Both the first and second harmonics turned convective at about the same  $T_c/T_H$ . At the convective transition, the frequencies were slightly above the odd half harmonics.

### 1.5.3 Significance to Diffuse Aurora

The observational and theoretical progresses on the role of ECH waves in driving diffuse aurora went hand in hand over the past 40 years. Since the first report of ECH observations in space, it has been suggested that these emissions may be responsible for the auroral electron ( $\sim 1-10$  keV) precipitation through pitch angle scattering, due to their large electric field amplitudes (1-10 mV/m) captured by OGO-5 spacecraft [*Kennel et al.*, 1970]. Using these wave amplitudes, *Lyons* [1974] quantified the associated bounce-averaged diffusion coefficients and indicated that the emissions reported by *Kennel et al.* [1970] could cause strong pitch angle diffusion for electrons in the hundreds to several thousand eV energy range, which soon were recognized as the typical energies implicated in the formation of diffuse aurora [*Eather and Mende*, 1972; *Eather et al.*, 1976; *Meng et al.*, 1979; *Fontaine and Blanc*, 1983]. However, the importance of ECH scattering was challenged by a following statistical analysis based on the GEOS-2 data [*Belmont et al.*, 1983], which showed that within  $3^\circ$  of the magnetic equator in the region 2200-0600 MLT, 88% of the time the wave amplitude was  $<0.1$  mV/m. Since the ECH wave amplitude estimated for

strong diffusion of  $\sim 1$  keV electrons ( $\geq 2\text{mV/m}$ ) was not reached during most of the investigated intervals (91%), *Belmont et al.* [1983] concluded that ECH waves are not intense enough to account for continuous electron precipitation in diffuse aurora and other mechanisms should be included. Predominance of weak ECH emissions was also shown later by *Roeder and Koons* [1989] using the SCATHA and AMPTE Ion Release Module (IRM) data, and by *Koons and Roeder* [1990] using the SCATHA data.

The seeming contradiction between different datasets may result from different spacecraft orbits: SCATHA ( $7.8 R_E$  apogee) and GEOS-2 (geostationary orbit) were too close to Earth, so their sampling of the neutral sheet beyond  $7 R_E$  was scarce, while ECH wave database from OGO-5 was at  $4 < L < 10$ ; AMPTE/IRM was in a highly elliptical orbit ( $28.6^\circ$  inclination) and did not spend much time at the neutral sheet.

A follow-on study by *Meredith et al.* [2000] using CRRES data demonstrated that ECH wave amplitudes following substorm activities were typically above  $1\text{mV/m}$ ; this led to a resurgence of interest in ECH waves. *Horne and Thorne* [2000] then evaluated the bounce-averaged pitch angle diffusion rate for representative ECH wave frequencies and found that substorm-related ECH waves have sufficient power ( $1\text{ mV/m}$ ) to cause strong diffusion near the loss cone for electrons below  $500\text{ eV}$ . This conclusion was further confirmed by *Horne et al.* [2003], who investigated wave propagation and resonant electron scattering for a weak substorm injection event and suggested that ECH waves were responsible for the diffuse aurora in that particular case. A statistical survey of upper band chorus and ECH waves using CRRES data [*Meredith et al., 2009*] revealed that the global distribution of the two wave modes and the electron fluxes are

similar to the morphology of the diffuse aurora, indicating that both wave modes are important in driving the diffuse aurora at CRESS distances, inside of  $L=7$ .

Apparently it was thought in the early studies, that ECH wave scattering must approach strong diffusion limit in order for these waves to cause sufficient diffuse aurora. In modeling the convection and resonant diffusion of plasma sheet electrons, *Fontaine and Blanc* [1983] also noticed that the strong diffusion assumption might overestimate the efficiency of wave-particle interactions. A similar conclusion was reached by *Chen and Schulz* [2001a, 2001b], who modeled the distribution of precipitating energy flux under various pitch angle diffusion rates and concluded that scattering below the strong diffusion limit was needed to best simulate electron precipitations near dawn and in the morning sector. This indicates the importance of quantifying the scattering rates of plasma sheet electrons with a more realistic wave model.

More recent studies, combining CRRES observations of ECH and chorus wave distributions and theoretical modeling [*Thorne et al.*, 2010; *Ni et al.*, 2011b, 2011c; *Tao et al.*, 2011] have shown that whistler mode chorus is the dominant driver of the diffuse aurora on the nightside in the inner magnetosphere ( $L < \sim 8$ ), because only chorus can explain the observed pancake electron distribution left behind in space after electrons at smaller pitch angles have been removed by scattering into the loss cone. The mechanism of the diffuse auroral precipitation at higher  $L$ -shells, however, remains unclear. A recent survey of chorus waves using THEMIS observations [*Li et al.*, 2009b] has demonstrated that the occurrence rate of moderately intense chorus emissions ( $\geq 10$  pT) drops significantly beyond  $\sim 8 R_E$ . Moreover, average wave amplitudes are below a few pT throughout the night-to-dawn sector, i.e., insufficient to cause efficient diffuse aurora at this region. On the other hand, moderately strong ECH emissions ( $\sim 0.1$ - $1.0$  mV/m)

have been reported to extend up to  $\sim 12 R_E$  [Roeder and Koons, 1989; Ni et al., 2011a], and may thus drive electron precipitations in these high L-shells (8-12). Furthermore, Ni et al. [2012a] have evaluated the precipitation flux due to ECH waves in a detailed case study at  $L=11.5$ , showing that the resultant auroral brightness agrees with auroral observations at the magnetic foot point.

Therefore, it is possible that ECH waves could be significant for diffuse aurora generation in the middle to outer magnetotail (beyond  $\sim 8R_E$ ), especially during an active plasma sheet. However, only a careful and comprehensive study of the wave occurrence, amplitudes, linear theory and precipitation modeling can resolve this issue. This is what we attempt to do in this dissertation.

## 1.6 Motivation

Although the relative importance of ECH waves for diffuse aurora generation has been intensively evaluated in past studies, the answers have been contradictory in the middle to outer magnetosphere. Furthermore, most of these studies have been focused on observations; the few theoretical studies have failed to systematically explain all the observations. For instance, from the statistical plot of precipitated diffuse auroral energy flux (Figure 1.5), we can see the diffuse aurora is still very intense in higher magnetic latitudes, between  $65^\circ$  and  $70^\circ$ , which maps to the plasma sheet from  $L\sim 8$  to beyond  $L\sim 15$ . With potential driver attributed to ECH waves, this indicates that there should be ECH waves in such high L-shells. But recent statistical survey of ECH waves [Ni et al., 2011a] showed that these waves are relatively scarce in such high L-shells, implying that the wave excitation mechanism and amplitude responsible for filling the loss cone and the loss-cone properties resulting in the observed precipitation rates are far from understood.

The main reason causing this discrepancy is lack of equatorial observations of ECH waves and accompanying electron distributions. Comprehensive observations from this region are a prerequisite to an investigation of the excitation mechanism of these waves. Furthermore, quantitative evaluation of plasma sheet electron interactions with a more realistic ECH wave model is required to better evaluate these waves' contribution in driving the diffuse aurora. THEMIS, which was launched on February 17, 2007, consists of five identical satellites (probes) equipped with comprehensive particles and fields instrumentation [Angelopoulos *et al.*, 2008], measuring ions and electrons from  $\sim 5$  eV to  $\sim 1$  MeV and electromagnetic waves from DC to  $> 4$  kHz (up to 8 kHz from 2010). Its near-equatorial orbits with apogees above  $10 R_E$  and perigees below  $2 R_E$ , are ideal for capturing ECH emissions in the equatorial magnetosphere. With its prolonged residence time in the plasma sheet, THEMIS provides routine observations of ECH waves together with corresponding electron distributions directly applicable to the study of 0.1-4 kHz waves in the plasma sheet. Therefore, for the first time, we could extend observations of ECH waves to the middle and outer magnetosphere (beyond  $L \sim 8$ ), characterize ECH waves on a large dataset near the equatorial region, examine the generation of these emissions, and investigate the detailed contribution of ECH waves to the diffuse aurora especially at high  $L$ -shells.

Specific definitions of middle and outer magnetosphere may vary in different studies. To be consistent in terminology within this dissertation, we define inner magnetosphere as the region with equatorial crossings  $< 8R_E$ , middle as between  $8 R_E$  and  $12 R_E$ , and outer as beyond  $12 R_E$  (up to  $35 R_E$  in our database).

## **1.7 Objective and Organization of the Dissertation**

The contradiction between continuous precipitation drizzling down into the ionosphere at high latitudes and the scarcity of ECH observations at high L-shells indicates the source of scattering at these high L-shells still remains unknown. Tied to the global particle energy budget, this brings an important question to the forefront: what causes the pitch-angle scattering of the plasma sheet electrons in these high L-shells? To answer this question thoroughly, we need to first understand the excitation mechanism and the features of ECH waves, which are the potential driver of the diffuse aurora outside the inner magnetosphere.

Taking advantage of the new data available in the plasma sheet from THEMIS and existing theoretical tools (dispersion relation solvers, ray tracing, diffusion modeling), the main objective of this dissertation is to understand the excitation of ECH emissions in the middle to outer magnetosphere under a variety of geomagnetic conditions. We first investigate the excitation of ECH waves theoretically during quiet plasma sheet and then examine the wave intensification observationally during active times. After characterizing theoretically the presence and amplitude of ECH waves at realistic, high curvature geometry, with low B field (small loss cone) and establishing the correlation between wave intensification and plasma sheet dynamics, we study in detail the distribution and extent of ECH waves, critical parameters for modeling their contribution to electron scattering and to diffuse auroral precipitations. In order to understand the wave intensification in the aftermath of dipolarization fronts (DFs), which may cast light on the excitation of ECH waves in general, we also model them.

Based on the obtained ECH wave features from the above studies, we then model these waves' interaction with plasma sheet electrons realistically throughout the entire magnetotail, in order to

resolve the long-standing question of the role that ECH waves play in diffuse auroral precipitation.

This dissertation is organized into six chapters:

After this introduction, in Chapter 2, I conduct a comprehensive study of wave growth and quasi-linear diffusion to estimate of the amplitude of loss-cone-driven ECH waves during quasi-steady state of the plasma sheet, when diffusion and growth balance but before convection or losses alter the background hot plasma sheet population. We expect such a quasi-steady state to be the most common state of the plasma sheet between episodes of fast convection. For any given wave amplitude, I model electron diffusion caused by interaction with ECH waves using a 2-D bounce-averaged Fokker-Planck equation. After fitting the resultant electron distributions as a superposition of multi-component subtracted bi-Maxwellians, I estimate the maximum path-integrated gain using the HOTRAY ray-tracing code. I then infer the wave amplitude during quasi-steady state from the gain-amplitude curve. During quasi-steady state, ECH wave amplitudes can be significant ( $\sim 1$  mV/m) at  $L \sim 8$  but drop to very low values ( $< \sim 0.1$  mV/m) in the outer magnetotail ( $L \sim 16$ ) and likely fall below the sensitivity of typical instrumentation relatively close to Earth mainly because of the smallness of the loss cone. This result reinforces the potentially important role of ECH waves in driving diffuse aurora and suggests that ECH emissions at high  $L$ -shells ( $L > \sim 12$ ) may be present, and may thus be responsible for the observed diffuse aurora precipitation during quiet times, even though evidence of these waves may be scarce at current data sets due to their small amplitudes.

In Chapter 3, I statistically investigate the relationship between ECH wave intensifications and electron injections, and dipolarization fronts in the plasma sheet using THEMIS observations,

which may help us better understand the wave excitation in general. I find that >70% of ECH waves are correlated with injections and >50% of the waves are correlated with DFs. ECH waves start after local particle injections and DF onsets by  $\sim 500$  s and  $\sim 60$  s, respectively. When ECH waves are correlated with both DFs and injections, injections are observed to occur first, then DFs, shortly followed by ECH waves. I hypothesize that the along with injected electrons, resonant electron fluxes at the edge of the loss cone are also enhanced, contributing to ECH wave intensification along their drift paths, while DFs reduce the field line curvature and lead to a broader latitudinal spreading of these waves around the magnetic equator. Thus, I suggest that waves are both easier to excite and also to observe under such conditions, consistent with previous observational studies.

After examining the excitation of ECH waves during quiet times and the wave intensification during active times, I investigate observationally (in Chapter 4) the occurrence rate distribution of ECH waves, the extent of individual wave intensifications under various plasma sheet conditions, and the mechanism leading to different wave Z-extent under various plasma sheet conditions. Single-spacecraft data analysis shows that ECH waves occur frequently in the midnight and post-midnight magnetotail and that their occurrence rates decrease with increasing radial distance from Earth. Excluding ECH wave emissions concurrent with local plasma sheet activations (known to peak in occurrence rate near pre-midnight), I find that quiet plasma sheet ECH wave emissions are preferentially observed at the dawn side of the plasma sheet. This preference suggests a close relationship between these waves and the drift paths of injected electrons. Dual-spacecraft data analysis shows that the Z-extent is  $\sim 0.5 R_E$ , the Y-extent is  $\sim 2 R_E$ , and the X-extent is at least  $4 R_E$ . During locally quiet plasma sheet conditions, ECH waves exhibit a smaller Z- and X-extent, but the Y-extent is similar during all conditions. By modeling

the wave power distribution as a function of distance from the neutral sheet under different magnetic field topologies, I find a linear correlation between the wave  $Z$ -extent and field line curvature radius ( $R_c$ ), confirming our previous hypothesis that ECH intensification following DFs is in part due to increased  $R_c$ .

Using the established features of ECH waves in the magnetotail from the above three studies, I then evaluate the plasma sheet electron precipitation by modeling ECH wave interactions with these electrons, aiming to answer the question of the ECH contribution to the diffuse aurora in Chapter 5. I first model the diffuse aurora precipitation in the ionosphere using the OVATION Prime model and then map this distribution to the neutral sheet using empirical Tsyganenko magnetic field models. I show that the proportion of precipitation beyond  $8 R_E$  on the nightside is significant especially during low solar wind driving conditions. By modeling the ECH wave interactions with plasma sheet electrons, I estimate the loss cone fill ratio and the resultant precipitating energy flux at different regions of the tail. I find the spatial distribution of the latter resembles the equatorially mapped distribution of diffuse aurora precipitation. I find that the ECH wave contribution to the total diffuse aurora precipitation energy flux increases with distance from the Earth mainly due to smaller loss cone size, even though the wave amplitude decreases with distance. This suggests that ECH waves play a dominant role in driving diffuse aurora in the middle to outer magnetotail, beyond  $\sim 8 R_E$ .

In Chapter 6, I summarize the results presented in Chapters 2-5 and discuss promising future work.

## CHAPTER 2

### **Estimation of ECH Wave Amplitudes during Quasi-steady, Marginally Unstable State of the Plasma Sheet**

The goal of this chapter is to address the apparent contradiction between the scarcity of observations of ECH emissions in the outer magnetotail and the presence of diffuse auroral precipitation at higher latitudes (up to about  $70^\circ$  MLAT). We estimate the ECH wave amplitude during the quasi-steady state of interactions of those waves with plasma sheet electrons, when particle diffusion and wave growth balance with each other. We found that as we move to higher L-shells, smaller wave amplitudes are required to establish the quasi-steady state, suggesting that such ECH emissions at high L-shells may be present and may thus be responsible for the observed precipitation, even though evidence of these waves may be scarce at current datasets due to their small amplitude. The result in this chapter reinforces the potentially important role of ECH waves in driving diffuse aurora.

We present a brief introduction on the background of our work in Section 2.1, including the motivation for such a comprehensive study of wave growth and quasi-linear diffusion. Section 2.2 describes how we estimate the ECH wave amplitude. Modeling results are shown in Section 2.3. In section 2.4, we summarize this study and discuss the implications for the ECH waves' contribution to diffuse aurora.

## 2.1 Introduction

As discussed in Section 1.5.3, both ECH waves and whistler-mode chorus have been considered as potential drivers for diffuse aurora, which are the dominant contributor to hemispheric energy flux precipitating into the ionosphere [Newell *et al.*, 2009]. The relative importance of ECH waves to diffuse auroral precipitation has been controversial for over four decades [e.g., Kennel *et al.*, 1970; Lyons, 1974; Belmont *et al.*, 1983; Roeder and Koons, 1989; Horne and Thorne, 2000; Horne *et al.*, 2003; Meredith *et al.*, 2009]. Recent studies have shown that ECH waves are the potential driver of diffuse aurora in the middle to outer magnetosphere [Ni *et al.*, 2011a; Ni *et al.*, 2012a], whereas whistler-mode chorus waves play a dominant role in the inner magnetosphere ( $< \sim 8 R_E$ ) [Thorne *et al.*, 2010; Ni *et al.*, 2011b, 2011c].

The statistical study by Newell *et al.* [2009] revealed contradictory observational evidence regarding the propensity and importance of ECH wave emissions at high L-shells. Diffuse auroral precipitation is both statistically significant and energetically efficient at higher latitudes, since about half the emissions are contributed by precipitation at magnetic latitudes from  $> 65^\circ$  to  $\sim 70^\circ$  across  $\sim 17$  hours of magnetic local time (MLT) centered at  $\sim 3$  MLT (see Figure 1.3). These latitudes are expected to map outside the inner magnetosphere from  $L \sim 8$  to beyond  $L \sim 15$ . On the other hand, according to Ni *et al.* [2011a], ECH waves at high L-shells (especially  $> \sim 12$ , see their Figures 1 and 2) are relatively scarce. Other free energy sources for electron scattering, such as whistler-mode chorus, are also absent at high L-shells [Li *et al.*, 2009b]. The observations therefore suggest that although electron scattering into the loss cone persists at high L-shells, the wave mode, excitation mechanism and amplitude responsible for filling the loss cone and loss-cone properties resulting in the observed precipitation rates are far from

understood. Since the electron loss cone still exists in the outer magnetosphere, providing free energy for ECH wave excitation, it is reasonable to assume that these electrostatic waves still exist there. We evaluate ECH wave electric field amplitudes during quasi-steady state at different magnetotail locations using idealized but physically accurate models of the interplay between magnetic field strength and curvature, wave growth and propagation, and electron diffusion and loss-cone evolution, to establish trends that may help explain the above observational discrepancy. We find that ECH wave amplitudes consistent with quasi-steady state decrease with increasing L value and likely fall below the instrument detection level reasonably close to the inner edge of the plasma sheet.

## **2.2 Methodology**

The methodology to evaluate the wave amplification corresponding to the prescribed electric field amplitude is summarized in the flow chart in Figure 2.1. It involves repeated cycles of the following three steps: modeling the electron diffusion using quasi-linear theory, fitting the electron distribution function, and evaluating the wave amplification using the HOTRAY ray tracing code.

### **2.2.1 Modeling Electron Diffusion Using Quasi-linear Theory**

We modeled the evolution of the electron pitch-angle distribution caused by interactions with ECH waves using Equation (2.1), the 2-D bounce-averaged Fokker-Planck equation [*Tao et al.*, 2011; *Ni et al.*, 2012b], to obtain the electron phase space density (PSD)  $f$  in a marginally unstable state

$$\begin{aligned} \frac{\partial f}{\partial t} = & \frac{1}{S_0 \sin \alpha_{eq} \cos \alpha_{eq}} \frac{\partial}{\partial \alpha_{eq}} (S_0 \sin \alpha_{eq} \cos \alpha_{eq} \langle D_{\alpha\alpha} \rangle \frac{\partial f}{\partial \alpha_{eq}}) \\ & + \frac{1}{p^2} \frac{\partial}{\partial p} (p^2 \langle D_{pp} \rangle \frac{\partial f}{\partial p}) - \frac{f}{\tau}. \end{aligned} \quad (2.1)$$

Here  $p$  is the particle momentum,  $\alpha_{eq}$  is the equatorial pitch angle,  $S_0$  is the bounce period-related term, and  $\langle D_{\alpha\alpha} \rangle$  and  $\langle D_{pp} \rangle$  are the bounce-averaged pitch-angle and momentum diffusion coefficients, respectively. Mixed diffusion terms  $D_{ap}$  were omitted in this equation. The loss time  $\tau$  is set to one quarter of the bounce period if  $\alpha_{eq}$  is less than the local loss-cone angle  $\alpha_{lc}$  and infinity otherwise. Our neglect of mixed diffusion terms simplified the algorithm and reduced the computation time, while retaining the dominant diffusion process that affects plasma sheet electrons [e.g., *Albert and Young, 2005*].

To account for the stretched configuration of a realistic magnetotail, we adopted the Dungey magnetic field model [*Dungey, 1961*], which consists of a dipole magnetic field and a uniform southward magnetic field. The stretching of the Dungey field relative to the dipole field is controlled by the intensity of the superimposed southward magnetic field ( $B_{z,0}$ ), described by the parameter  $b = (M / B_{z,0})^{1/3}$  ( $M$  is the dipole magnetic moment). Smaller  $b$  values result in more stretched fields. When  $b$  goes to infinity, the Dungey field reduces to a dipole field. The magnetic field-related parameters ( $S_0$  and  $\alpha_{lc}$ ) in Equation (2.1) were evaluated for this model using the equations given by *Ni et al. [2012b]*. Because the magnetic field intensity in the Dungey field decreases at lower latitudes (within about  $\pm 15^\circ$ ) but increases at higher latitudes compared to the dipole configuration, the loss-cone size ( $\alpha_{lc}$ ) at a given L-shell is smaller for the

Dungey model than for the dipole. In addition, the particle bounce period decreases due to the stretched field lines. The latitudinal wave vector distribution was obtained using the ray-tracing code HOTRAY [Horne, 1989] for a fixed wave frequency (we used  $f=1.2f_{ce}$  for the equatorial wave frequency based on typical values of such waves in the observations). Following Ni *et al.* [2011b, 2012a], we calculated the bounce-averaged diffusion coefficients in the Dungey fields, shown in Figure 2.2 (for one case at L=16 with wave electric field amplitude  $E_w = 0.1\text{mV/m}$ ), using the UCLA Full Diffusion Code [Ni *et al.*, 2008; Shprits and Ni, 2009]. Bounce-averaged diffusion coefficients spread over a broader energy and pitch-angle range with a Dungey field than with a dipolar field, and the rates increase, especially at lower energy levels, mainly due to smaller magnetic field intensity.

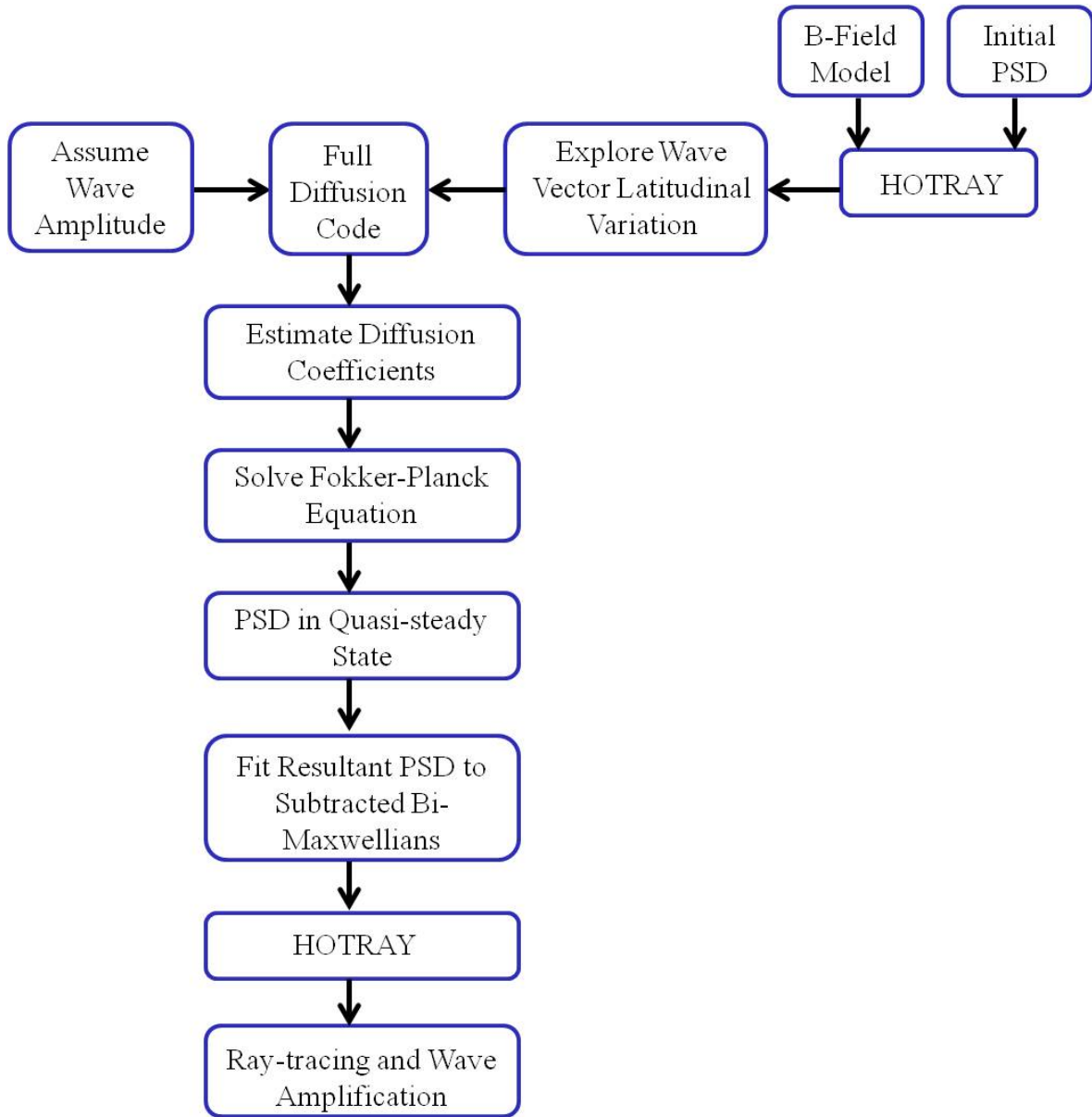


**Figure 2.1:** Flow chart of methodology to estimate wave amplification corresponding to the prescribed electric field amplitude.

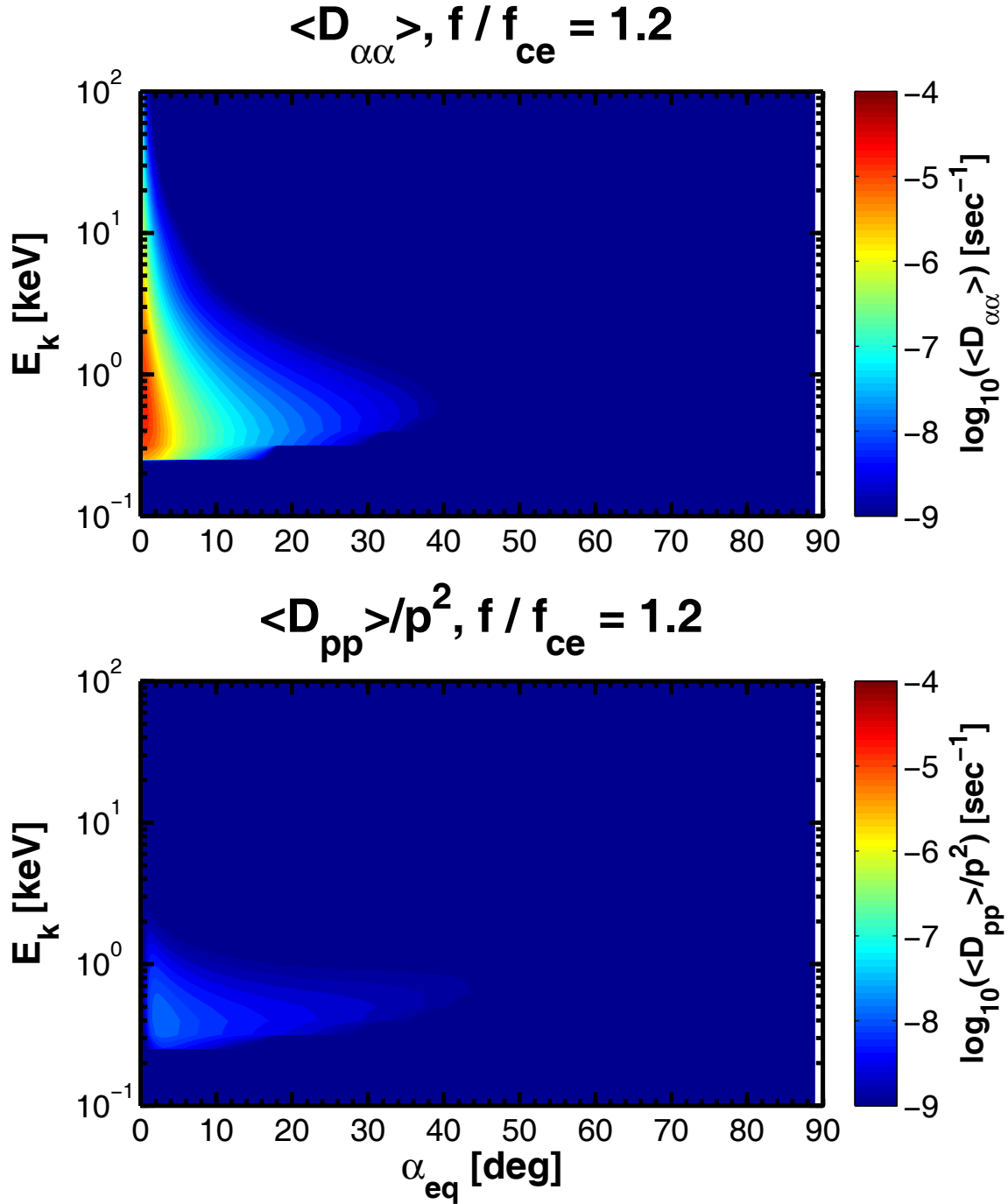


**Figure 2.2:** Bounce-averaged pitch-angle (upper panel) and momentum (lower panel) diffusion coefficients as a function of equatorial pitch angle and electron kinetic energy due to ECH waves ( $L=16, E_w=0.1\text{mV/m}$ ).

The alternative direction implicit method [Xiao *et al.*, 2009; Tao *et al.*, 2011] was used to numerically solve Equation (2.1). The initial conditions were taken from THEMIS observations, after suppressing anisotropies of the hot component outside the loss cone, recognizing that such anisotropies are variable and not permanent in the plasma sheet. Boundary conditions for the pitch-angle operator were:  $\partial f / \partial \alpha_{eq} = 0$  at  $\alpha_{eq} = 0^\circ$  and at  $\alpha_{eq} = 90^\circ$ . For  $\alpha_{eq} = 0^\circ$ , a zero PSD boundary condition ( $f = 0$ ) can be used only for weak pitch angle diffusion due to losses of electrons within the loss cone; a zero gradient boundary condition can be used for both strong and weak pitch angle diffusions, which requires enough pitch angle grid points to resolve the loss cone. Because pitch angle diffusion rates may exceed the strong diffusion limit when we vary the wave amplitude, we used the zero gradient condition at the low pitch angle boundary in this study. For the energy diffusion operator, the lower boundary was held constant at 47 eV because the diffusion timescale of these electrons is much longer than that of typical plasma sheet electrons; the upper boundary was also held fixed at 26 keV, well above typical resonant energies of ECH waves with plasma sheet electrons (hundreds of eV to several keV). Although electron diffusion lasts for hours, basic loss-cone properties are established rather quickly (minutes to tens of minutes); after that, the drainage of electrons at larger pitch angles takes place very slowly, over timescales of many hours to days. We assume that the marginally unstable state has been reached when the electron PSD over potentially resonant energies changes less than 10% in 1 hour.

### 2.2.2 Fitting Electron Distribution Function

To evaluate the amplification of ECH emissions using the HOTRAY ray-tracing code, we need to model the PSD of resonant electrons. The electron PSD ( $f$ ) within the boundaries of

potentially resonant energies was fitted as a sum of subtracted bi-Maxwellians [e.g., *Ashour-Abdalla and Kennel, 1978; Horne et al., 2003; Li et al., 2009a*] given by

$$f = \sum_i f_i,$$

where each component is expressed by:

$$f_i(v_{\parallel}, v_{\perp}) = \frac{n_i}{\pi^{2/3} \alpha_{\perp i}^2 \alpha_{\parallel i}} \exp\left(-\frac{v_{\parallel}^2}{\alpha_{\parallel i}^2}\right) \cdot \left[\Delta_i \exp\left(-\frac{v_{\perp}^2}{\alpha_{\perp i}^2}\right) + \frac{(1-\Delta_i)}{(1-\beta_i)} \cdot \left(\exp\left(-\frac{v_{\perp}^2}{\alpha_{\perp i}^2}\right) - \exp\left(-\frac{v_{\perp}^2}{\beta_i \alpha_{\perp i}^2}\right)\right)\right]. \quad (2.2)$$

Here  $n_i$  is the electron density,  $\alpha_{\perp i}$  and  $\alpha_{\parallel i}$  are the thermal velocities perpendicular and parallel to the ambient magnetic field, and  $\beta_i$  and  $\Delta_i$  essentially determine the depth and width of the loss cone, respectively.

### 2.2.3 Evaluation of Wave Amplification Using HOTRAY Ray-Tracing Code

Using the above-modeled electron distributions and the HOTRAY code, we simulated ECH wave propagation in Dungey fields as follows: at every step along each ray path, the hot plasma dispersion relation for electrostatic ECH waves was solved to obtain amplification of the wave electric field over a ray path  $\mathbf{r}$  (path-integrated gain  $G$  in dB) [*Horne and Thorne, 1997; Li et al., 2009a*]:

$$G = 20 \log_{10}(E / E_0) = 8.6859 \int \mathbf{k}_i \cdot d\mathbf{r}. \quad (2.2)$$

Electron cyclotron harmonic waves typically refract once they are only a short distance away from the neutral sheet, due to field line bending, which modifies the wave normal angle to the field and thus the group velocity. Because of the larger curvature of the Dungey field configuration, the waves reflect at lower latitudes (closer to the neutral sheet) in a Dungey field than in a dipole field. Furthermore, Dungey field intensity along a ray path is different from that along a ray path in the dipole; this field intensity directly affects the local value of  $f/f_{ce}$  and thus the wavenumber and the magnitude of path-integrated gain. For a given electric field amplitude, the electron distribution was first evolved through quasi-linear diffusion to attain a marginally unstable state (see Figure 2.3). Then, using that evolved distribution as an input to the HOTRAY code, nineteen rays were launched from the magnetic equator with the same wave frequency ( $1.2f_{ce}$ ) and wave normal angle ( $89.8^\circ$ ), but propagating with different initial azimuthal angles ( $0^\circ$ - $180^\circ$  range) and thus into different magnetic field strengths and curvatures. We assume that the gain along the ray path can represent the final amplitude of the wave, in addition to the local wave growth. We also assume that this path-integrated gain dominates over changes in the wave energy density due to divergence of the rays. We thus recorded the maximum path-integrated gain for each azimuthal angle and computed the median value of these nineteen peak gains to represent the maximum amplification corresponding to the prescribed electric field amplitude and its accompanying electron distribution. By varying the wave electric field amplitude over a wide range of reasonable values, we determined the expected amplification (gain) of ECH waves from self-consistently evolved electron distributions.

Only one point on those gain-amplitude curves is expected to be consistent with a given set of ambient plasma sheet conditions for the quasi-steady state. That point is determined as a balance between the local plasma properties (i.e., the dispersion relation) affecting the wave vector, the

resonant energies and resonant particle number densities on the one hand and the properties of the surrounding medium (i.e., field curvature, gradients) controlling propagation, diffusion and amplification on the other. If amplification is lower than what is consistent with the quasi-steady state for these conditions, the local wave amplitudes will be lower; the electron distribution function will thus develop a deeper/sharper loss cone and then increase the wave growth rates. Consequently, the local amplitude will increase dramatically relative to the quasi-steady state as part of the quasi-linear feedback process. If the local wave amplitude becomes lower than what is consistent with quasi-steady state conditions, the loss cone will be depleted and amplification will increase rapidly. For random variations of the medium, the system will settle towards a state of minimum amplitude for a given source and minimum amplification for a given model that are consistent with each other. Thus, the quasi-steady state point for a prescribed set of plasma and medium conditions, which is expected to be an inflection point on the gain-amplitude curve, can be identified from such curves for different L-shells. We define the quasi-steady state as the transition point at which the path-integrated gain curve as a function of wave amplitude changes dramatically from sharply descending to almost flat. Specifically, we linearly fitted the gain-log(amplitude) (G-logA) curve before and after the transition point with two distinct slopes and determined the wave amplitude at the intersection of two fitted lines as the ECH wave amplitude at the quasi-steady state. We examined the G versus A behavior for three different L-shells, L=8, L=12, and L=16.

In each set of runs for a fixed L-shell, the electron distribution was assumed to be constant with latitude and unchanging through the entire propagation region ( $< \sim 1 R_E$ ). To avoid any variations in the path-integrated gain due to differences in cold electron density, we used the same cold electron density ratio for each set of L-shell runs.

## 2.3 Results

In this section, we present our model results of ECH wave amplification at three different L-shells. We used quasi-linear theory to model the evolution of electron pitch-angle distribution due to interactions with ECH waves. Figure 2.3 shows results for one case at L=16 with wave electric field amplitude  $E_w = 0.1$  mV/m ( $f/f_{ce} = 1.2$ ) after interaction with ECH waves for one hour (1h) and two hours (2h). Clearly seen in this figure is that ECH waves can only affect the PSD of electrons with pitch angles  $<20^\circ$  over a limited energy range, which is consistent with numerical results by *Thorne et al.* [2010] and *Tao et al.* [2011]. Comparing the evolution of electron distributions at 1h and 2h, we see that the shape of the electron distribution was already rather stable except for a slow decrease in the distribution at both low ( $<0.4^\circ$ , i.e., inside the loss cone) and relatively high ( $0.4^\circ$ - $10^\circ$ ) pitch angles due to precipitation. Thus, we defined this state with stabilized electron pitch-angle distribution as marginally unstable state at this given wave amplitude ( $E_w = 0.1$  mV/m). This modeling was applied to all wave amplitudes considered.

The marginally unstable electron PSD from our diffusion calculation was fitted over the resonant energies using Equation (2.2); the result for the specific amplitude and L-shell in Figure 2.3 is presented in Figure 2.4. Three components were used to fit the diffused electron pitch-angle distribution in velocity space (PSD in Figure 2.3c). Because ECH waves affect only electron distributions with pitch angles  $<20^\circ$  and these waves are excited by PSD gradients near the loss cone, we only fitted the distributions with pitch angles  $<20^\circ$ . Moreover, we increased computational efficiency by fitting only the resonant portion (100's eV-3 keV) of the energy spectrum at pitch angles  $<20^\circ$  (free energy source). Even without considering the observational constraints on the pitch-angle variation of the distributions, due to the limited angular resolution

of current instrumentation, previous modeling studies have been severely affected by the limited capability of a single set of subtracted bi-Maxwellians to fit any realistic loss cone in the outer magnetosphere. Our use of multiple subtracted bi-Maxwellians overcomes those limitations and increases the fidelity of the loss-cone modeling, which provides realistic estimates of the growth rate and the resulting amplification.

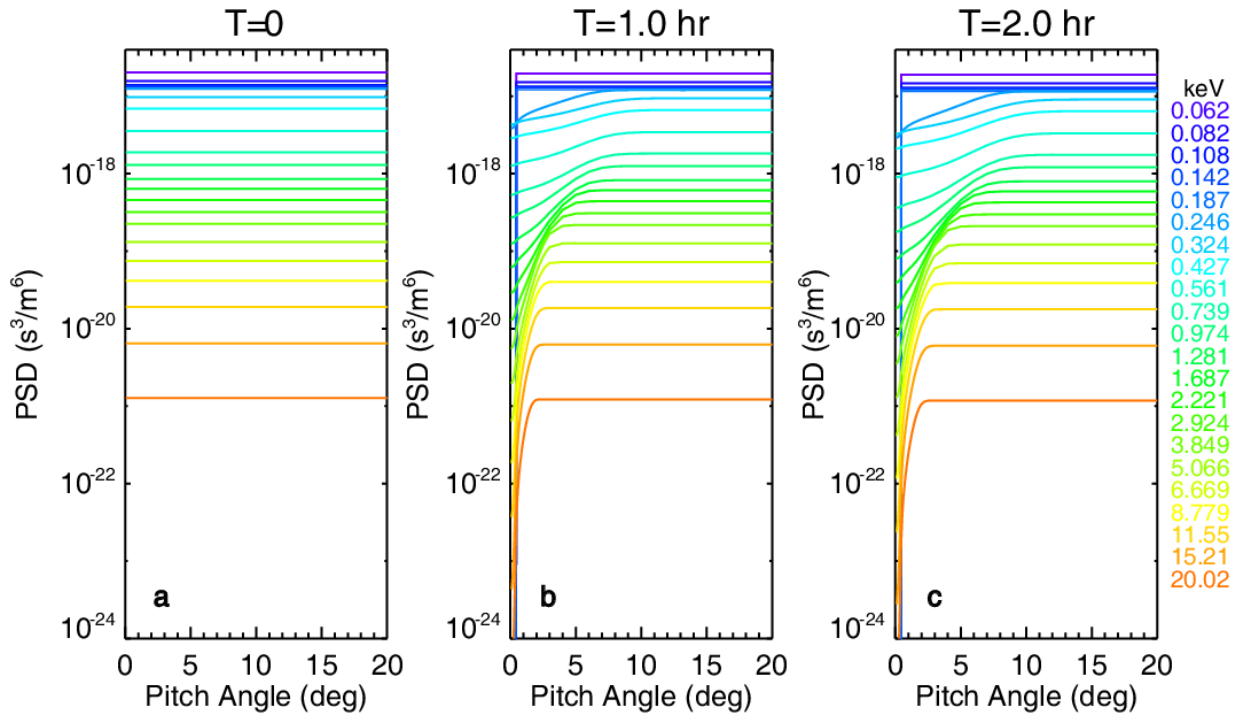


**Figure 2.3:** Initial electron distribution (isotropic) for modeling the diffusion process and the evolution of electron distribution after interaction with ECH waves for 1h and 2h ( $L=16$ ,  $E_w=0.1$  mV/m).

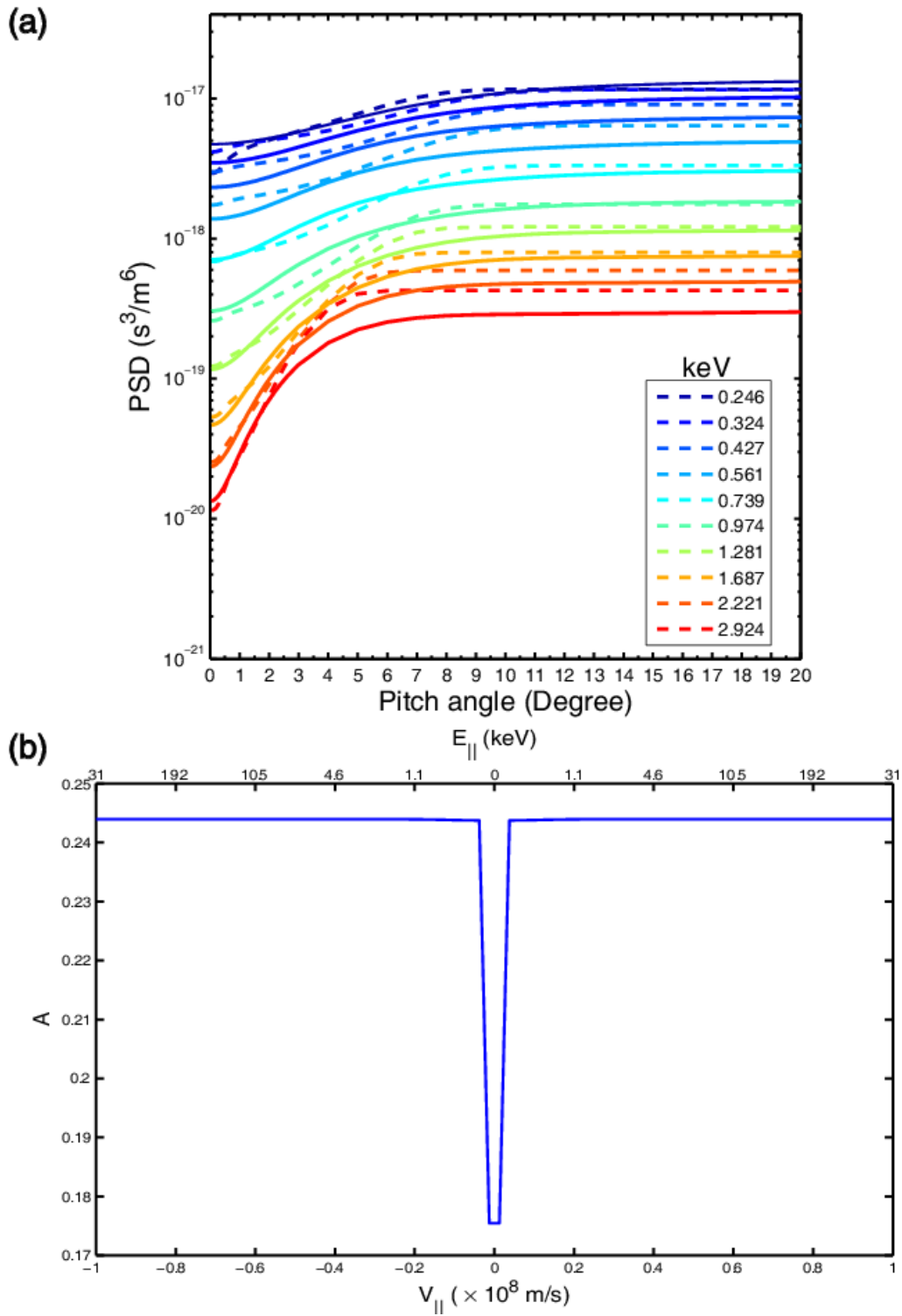


**Figure 2.4:** (a) Electron phase space density (PSD) after diffusion as a function of pitch angle for energy levels resonant with ECH waves. The dashed lines display the diffused electron

distribution, and solid lines represent electron PSD fitted to multi-component subtracted bi-Maxwellians. (b) The electron anisotropy as a function of parallel electron velocity/energy.

**Table 2.1:** Parameters of electron components used to model the diffused suprathermal electron phase space density for the case in Figure 2.3.

Component	$N_e(m^{-3})$	$T_{\perp}(eV)$	$T_{\parallel}(eV)$	$\Delta$	$\beta$
1	$3.78 \times 10^4$	1.35	1.35	1.0	0.5
2	$1.70 \times 10^5$	307.4	249.2	0.413	0.014
3	$1.70 \times 10^5$	1705.2	1382.1	0.047	0.009

The fitting parameters obtained by a constrained nonlinear optimization fit to the diffusion code results are listed in Table 2.1; these parameters were used as input to the HOTRAY code to trace ECH waves and obtain the path-integrated wave gain. As mentioned above, for each assumed wave amplitude at a specified location, we launched nineteen rays from the magnetic equator with the same wave frequency ( $1.2f_{ce}$ ) and wave normal angle ( $89.8^\circ$ ), but with various initial azimuthal angles from  $0^\circ$  to  $180^\circ$ . Then the median value of the nineteen maximum gains was recorded to represent the wave amplification corresponding to the prescribed wave amplitude. By varying the diffusion coefficients and magnetic field-related parameters in the first step (Section 2.2.1), we estimated the wave amplification corresponding to each assumed wave electric field amplitude at each L-shell. Figure 2.5 illustrates the variation of ECH wave

amplification with wave electric field amplitude at three L-shells. Error bars show the upper and lower quartiles of the maximum gain at each amplitude value over different azimuthal angles.

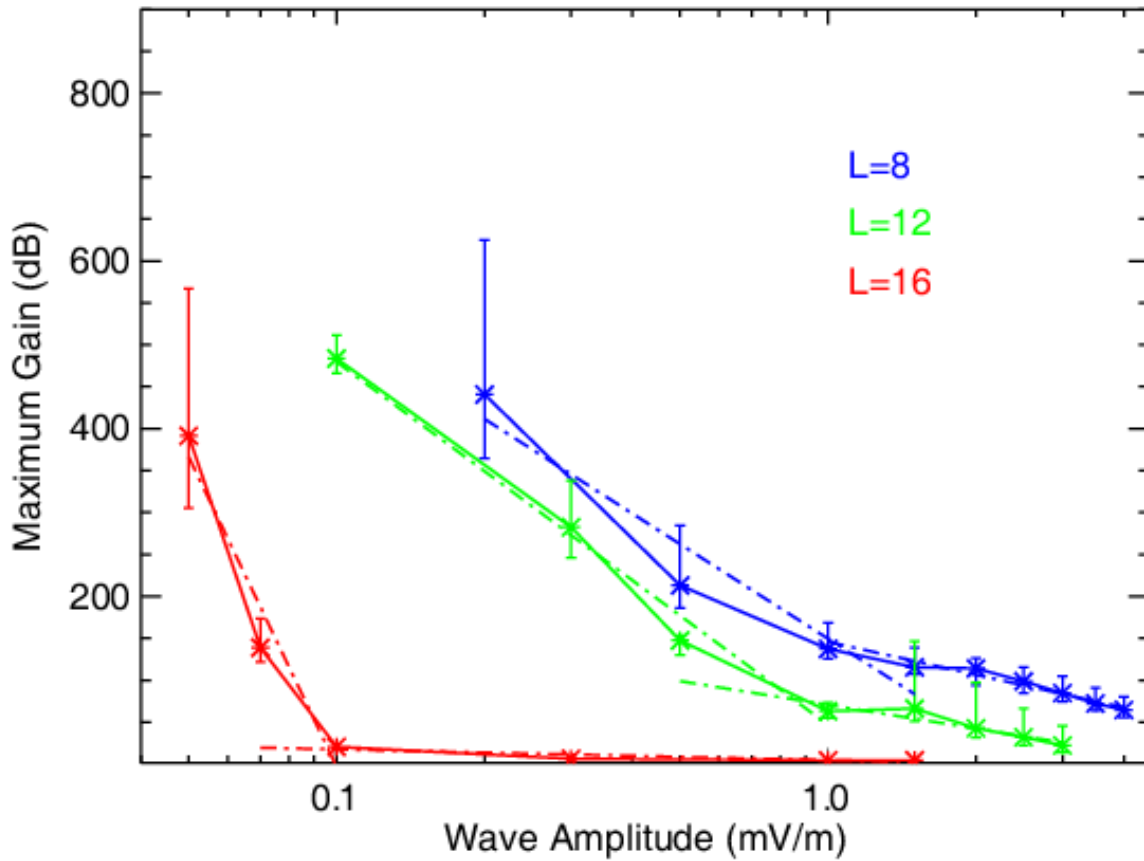


**Figure 2.5:** ECH wave amplification corresponding to different wave electric field amplitudes at  $L=8$ ,  $L=12$ , and  $L=16$ . Dashed lines were fitted to determine the inflection point corresponding to the quasi-steady state.

To quantitatively evaluate the inflection point in a gain-log(amplitude) curve, we linearly fitted the curve before and after the transition point with two distinct slopes (dashed lines in Figure 2.5) and defined the wave amplitude at the intersection of two fitted lines as the ECH wave amplitude at the quasi-steady state. From Figure 2.5, we can see that the ECH wave

amplitude consistent with quasi-steady state is  $\sim 1$  mV/m at  $L=8$ , but decreases with increasing  $L$ -shell. It drops to  $\sim 0.8$  mV/m at  $L=12$  and descends to  $\sim 0.1$  mV/m in the outer magnetotail ( $L=16$ ).

## 2.4 Summary and Discussion

We numerically modeled the interaction between electrons and ECH waves to estimate the amplitude of these waves during the quasi-steady state. Quasi-linear theory modeling was used to investigate the evolution of electron pitch-angle distributions due to interaction with ECH waves, from which we obtained the marginally unstable state electron distribution. The quasi-linearly evolved electron distribution (Figure 2.3) shows that ECH waves only affect the PSD of electrons over a limited energy range with pitch angles  $< 20^\circ$ , as consistent with previous numerical results [Thorne *et al.*, 2010; Tao *et al.*, 2011].

After obtaining the diffused electron distribution, we used the HOTRAY ray-tracing code to examine the path-integrated growth of ECH waves. By iteratively varying the wave electric field amplitude and evaluating the corresponding amplification, we determined the quasi-steady state as the transition point in the gain-amplitude curve. In this quasi-steady state, ECH waves diffuse electrons to form a partly-filled loss cone distribution that amplifies the waves only moderately. We find that the wave amplitude corresponding to the quasi-steady state decreases with increasing  $L$ -shell, from  $\sim 1$  mV/m at  $L=8$  to  $\sim 0.1$  mV/m at  $L=16$ .

To use the HOTRAY code to evaluate ECH emission amplification, we fitted the diffused electron distribution (Figure 2.3) with multi-component subtracted bi-Maxwellians. Discrepancies between the fitted and diffused electron distributions, especially near sharp

gradients at the edge of the loss cone, remain, however, indicating that our modeling cannot be used reliably for very small loss cones ( $\alpha_{lc} < 0.4^\circ$  or  $B_{eq} < 2$  nT). Furthermore, we used the Dungey magnetic field model, which likely overestimates the electron loss-cone size at high L-shells, to simulate the stretched outer magnetotail. Finally, ray tracing as applied here cannot give a good estimate of local wave amplitudes unless the source is well known and the change of wave energy density due to ray divergence is properly evaluated. Nonetheless, our results establish trends that can be extended outside the limits of our modeling.

Specifically, we found that as we move to higher L-shells, the progressively smaller loss cones at those L-shells can be readily filled through quasi-linear diffusion by smaller wave amplitudes, establishing the quasi-steady state. Although the absolute values of the quasi-steady state amplitude versus L-shell may not be accurate for the reasons explained earlier, our study captures the physics of the problem and establishes a realistic trend. We can reasonably extrapolate that the wave amplitude during the quasi-steady state can eventually drop to below electric field instrument (EFI) sensitivity level ( $\sim 0.01$  mV/m for the THEMIS EFI instrument) under a realistic field. In fact, our model's limitations (Dungey field insufficiently stretched, actual equatorial field smaller than modeled for a stretched magnetotail) suggest that quasi-steady state amplitudes may fall below sensitivity level as close as  $L \sim 10$ . At  $L \sim 10$ , the equatorial field is often  $\sim 1-5$  nT,  $\sim 10$  times smaller than a dipole's, and the field line radius of curvature is  $< 1 R_E$ ,  $\sim 3$  times smaller than a dipole's. The ubiquity of the free energy source (incompletely-filled loss-cone distribution) further supports our hypothesis that ECH waves may persist in the outer magnetosphere, but with amplitudes possibly below instrument noise level.

While recent theoretical and modeling studies [Thorne *et al.*, 2010; Ni *et al.*, 2011b, 2011c] have implied that whistler-mode chorus waves play a dominant role in driving diffuse aurora in the inner magnetosphere ( $< \sim 8 R_E$ ), ECH emissions have been identified as the potential driver of diffuse auroral precipitation in the middle to outer magnetosphere [Ni *et al.*, 2011a, 2012a]. The seeming contradiction between the presence of diffuse auroral precipitation at higher latitudes (up to about  $70^\circ$  MLAT) [Newell *et al.*, 2009] and the relative scarcity of ECH waves in high L-shells ( $> \sim 12$ ) was addressed in this chapter. Our results suggest that such ECH emissions at high L-shells ( $L > \sim 12$ ) are likely to be present, and can thus be responsible for the observed precipitation, even though evidence of these waves may be scarce at current datasets due to their small amplitude. For a more quantitative analysis, we can use realistic values of plasma sheet electron fluxes at the peak flux energy (100 eV-10 keV) from THEMIS observations (see, e.g., THEMIS overview plots) and the average loss-cone fill ratio computed from the modeled diffusion process. We thus estimated the precipitated electron energy flux resulting from ECH waves during the quasi-steady state (weak diffusion limit) at  $L=8$ ,  $L=12$ , and  $L=16$ , respectively, for relatively quiet times and active times. Our results are shown in Table 2.2. The strong diffusion case made by assuming distributions isotropic within  $\sim 30^\circ$  in pitch angle away from field aligned, including across the loss cone, was also included in Table 2.2. The variability of this estimated precipitating energy flux is noticeably large (a factor of  $\sim 3.0$ ) because of transient activations (injections associated with bursty bulk flows) that apparently continue even during relatively quiet times [e.g., Angelopoulos *et al.*, 1994]. The trends with L-shell are not necessarily representative, as we have used only a small dataset to determine typical energy flux for this analysis. However, it is instructive that the estimated precipitating energy flux agrees with Newell *et al.*'s [2009] statistical estimates of this flux at ionospheric altitudes, including at

high L-shells. This suggests that our estimates of the quasi-steady state amplitudes are reasonable. Note that in Table 2.2 we assumed the same weak diffusion fill ratios for both quiet and active times, namely, those determined from our quasi-steady state solution. The loss-cone filling and associated precipitation as a function of L and MLT, subject to observational constraints and under a variety of activity levels, will be investigated in a similar self-consistent manner in future studies.

**Table 2.2:** Assumed values of plasma sheet electron (100 eV-10 keV) fluxes from THEMIS observations and estimated precipitated electron energy flux for relatively quiet and active times with different diffusion extents at L=8, L=12, and L =16 respectively.

L	Quiet			Active		
	Assumed Energy Flux (eV/cm <sup>2</sup> /s/str/eV)	Estimated Precipitated Energy Flux (ergs/cm <sup>2</sup> /s)		Assumed Energy Flux (eV/cm <sup>2</sup> /s/str/eV)	Estimated Precipitated Energy Flux (ergs/cm <sup>2</sup> /s)	
		Strong Diffusion	Weak Diffusion		Strong Diffusion	Weak Diffusion
8	1.29×10 <sup>6</sup> -3.69×10 <sup>7</sup>	3.6-4.5	0.06-0.07	1.96×10 <sup>6</sup> -4.60×10 <sup>7</sup>	3.7-6.9	0.06-0.11
12	1.68×10 <sup>6</sup> -4.66×10 <sup>7</sup>	1.8-7.0	0.20-0.77	1.88×10 <sup>6</sup> -6.01×10 <sup>7</sup>	9.6-18.4	1.06-2.02
16	4.11×10 <sup>5</sup> -1.99×10 <sup>7</sup>	3.9-5.9	0.94-1.42	1.68×10 <sup>5</sup> -4.50×10 <sup>7</sup>	5.7-11.8	1.37-2.83

## CHAPTER 3

### **ECH Wave Intensification Correlated with Electron Injections and Dipolarization Fronts**

After investigating the wave amplitude during quiet times theoretically, we also want to know how ECH waves are generated under active conditions. Intense ECH waves are often observed upon arrival of fast earthward flows, which in turn are correlated with particle injections and dipolarization fronts (DFs) in the plasma sheet. Investigating the wave intensification during these plasma sheet dynamics may help to elucidate the excitation mechanism of these waves, a topic that has remained rather stagnant because of observational constraints under nominally quiet conditions. Using THEMIS observations, we establish a temporal correlation between ECH wave intensification and electron injections and DFs. We also discuss possible mechanisms leading to the intensification of ECH waves under different dynamic conditions.

Our working hypothesis is that intensified ECH waves have the same excitation mechanism with the emissions approaching quasi-steady state, but with different characteristics (e.g., amplitudes, duration, propagation and distribution features). Investigating the wave intensification during different magnetotail dynamics will shed light on the wave excitation mechanism under various conditions, especially considering our evidence that the quasi-steady state waves in outer magnetosphere may not be present at current datasets due to their small amplitude.

Section 3.1 briefly presents previous work on the generation of ECH waves and observations of wave intensifications during active times. In Section 3.2, we introduce the database and data format of the THEMIS instruments. Selection criteria for ECH waves, injections, and DFs and our methodology to characterize their temporal relationship statistically are described in Section 3.3. In Section 3.4, we present the statistical results to establish the correlation between ECH waves and injections/DFs. We summarize this study and discuss possible mechanisms leading to such a correlation in Section 3.5.

### **3.1 Introduction**

As discussed in Section 1.5.2, ECH waves are thought to be driven by loss-cone instability of the ambient, hot plasma sheet electron distribution in the presence of a low-density cold component [Ashour-Abdalla and Kennel, 1978; Horne, 1989; Horne *et al.*, 2003]. Adopting a mixed cold and hot electron (with a loss cone property) distributions, Ashour-Abdalla *et al.* [1979] performed a parametric study of convective loss cone instabilities. Their results further demonstrated that the cold electron density determines the harmonic bands that can be non-convectively unstable (both parallel and perpendicular group velocities simultaneously approach zero); this non-convective instability, corresponding to fast spatial growth, is only possible when the density and temperature ratio between cold and hot electron component are sufficiently small. Because of the difficulty in observing either the small loss-cone ( $<1^\circ$  in the outer magnetosphere) or the cold electron population, however, these ECH wave excitation mechanisms have not been verified.

During earthward convection, plasma sheet electrons (with only partially filled loss-cone) from the geomagnetic tail are expected to generate ECH waves. In turn, the waves can scatter the

resonant electrons into loss cone. There should be a quasi-steady state, where electron diffusion and wave growth achieve balance before subsequent convection or losses alter the hot plasma sheet population. In Chapter 2, we numerically modeled the interaction between electrons and ECH waves to estimate the amplitude of these waves during the quasi-steady state and concluded that the progressively smaller loss cones at higher L-shells can be filled through quasi-linear diffusion by smaller wave amplitudes, establishing quasi-steady state. Therefore, ECH wave amplitude in the outer magnetotail may drop below current instrument detection level during quiet conditions.

According to *Liang et al.* [2011], ECH emissions may intensify upon the arrival of fast earthward flows in the plasma sheet. Electron injections, rapid increases in energetic particle fluxes at energies from tens to hundreds of keV, are important contributors to particle acceleration and transport in Earth's magnetotail and are observed over a long portion of the magnetotail in association with flow bursts [*Sergeev et al.*, 2009; *Runov et al.*, 2011a]. They have been reported at various regions in the magnetotail, from geosynchronous orbit [e.g., *Mauk and Meng*, 1983; *Birn*, 1997a, 1997b, 1998], to mid-tail regions [*Runov et al.*, 2009, 2011a; *Gabrielse et al.*, 2012], to 60R<sub>E</sub> downtail [*Konradi*, 1966; *Sarris et al.*, 1976 and references therein]. Injections can be dispersionless or dispersed. If an injection is dispersionless (flux increases simultaneously over a broad energy range), the observations are interpreted to have been made near the injection source. Dispersed injections (flux increases first at higher energies) are attributed to energy-dependent particle drifts. Injections are typically associated with substorms and are correlated with dipolarization fronts [*Moore et al.*, 1981] in the near-Earth plasma sheet. Dipolarization fronts are characterized by a sharp, large-amplitude increase in the northward magnetic field component ( $B_z$ ), often preceded by a smaller amplitude negative

variation in  $B_z$  and coinciding with a rapid decrease in plasma density [Nakamura *et al.*, 2002; Ohtani *et al.*, 2004; Runov *et al.*, 2009, 2011a, 2011b]. Statistical studies have shown that DFs occur in the plasma sheet at a wide range of geocentric distances, from 5  $R_E$  to 30  $R_E$  downtail [Ohtani *et al.*, 2004]. Because they are often embedded within bursty bulk flows (BBFs) [Angelopoulos *et al.*, 1992], DFs are associated with significant magnetic flux transport.

A number of possible mechanisms may lead to ECH wave intensification during injections and DFs. A more dipolarized field configuration after DF passage [Liu *et al.*, 2013] implies a smaller field curvature (larger radius of curvature) than in a nominally stretched magnetotail. This decreased field curvature may affect wave propagation and results in latitudinal broadening of the high-amplitude ECH wave region around the neutral sheet. Furthermore, the electron fluxes near the resonant energy (hundreds to several thousand eV) that may also be enhanced during injections can both increase the resonant electron density and lead to sharper velocity-space gradients in electron distributions near the edge of the loss cone; both factors may contribute to ECH emission growth. In this study, therefore, we use injections as a proxy of increases in resonant electron energy fluxes. Decreased density and temperature ratios between cold and hot electrons resulting from injections may further expand the unstable range of non-convective region for ECH waves in parameter space, promoting fast amplification of these waves. It is even possible that drifting electrons injected by a non-local source may contribute to the excitation of ECH emissions all along their paths, by modifying the loss cone properties and the local plasma conditions.

The correlation between ECH wave intensification and magnetotail dynamics has not been investigated statistically, however. Higher-amplitude ECH waves can scatter plasma sheet

electrons into the loss cone and precipitate them at a higher rate (occasionally even approaching the strong diffusion limit), which can affect the diffuse auroral energy flux. A statistical study of the relationship between ECH waves and magnetotail activities can further improve our understanding of ECH wave generation and related particle scattering under diverse plasma sheet conditions, such as during BBFs, DFs, and energetic particle injections. With its prolonged residence in the center of the plasma sheet and its comprehensive observational database of waves and particles in the magnetotail, the THEMIS mission enables such a statistical survey, in order to quantify the degree of correlation between DFs, injections and ECH waves and contribute to further understanding of ECH wave excitation, propagation and effects on particle scattering.

### **3.2 THEMIS Database and Instrumentation**

THEMIS consists of five identical spacecraft (probes P1, P2, P3, P4, and P5) equipped with comprehensive particle and field instruments [Angelopoulos, 2008]. The probes' near-equatorial orbits with apogees above  $10 R_E$  and perigees below  $2 R_E$  are ideal for capturing ECH emissions in the equatorial magnetosphere. Only observations from the three inner THEMIS probes (P3, P4, and P5) were used, because ECH emissions are rarely found beyond  $12 R_E$  in the database [Ni *et al.*, 2011a]. Our statistical database comes from five THEMIS tail science phases (excluding intervals when the Electric Field Instrument was in the probe's shadow), covering intervals from 15 December 2007 to 15 April 2008, 15 December 2008 to 15 April 2009, 2 March 2010 to 31 May 2010, 16 March 2011 to 22 June 2011, and 13 April 2012 to 14 October 2012.

The Electric Field Instrument (EFI) [Bonnell *et al.*, 2008] and Search Coil Magnetometer (SCM) [LeContel *et al.*, 2008; Roux *et al.*, 2008] measure wave electric and magnetic fields in

three orthogonal directions. Observations from EFI and SCM are passed to the Digital Fields Board (DFB) [Cully *et al.*, 2008] to calculate the mean amplitude of the electric and magnetic fields in 6 logarithmically-spaced frequency bands from 0.1 Hz to 6 kHz, producing Filter Bank (FBK) data with a cadence of 4 seconds. In this study, FBK data are used to select ECH events. Since 1 May 2010, new wave power spectra data (FFF data, with a cadence of 8 seconds) became available during the fast survey mode, providing high frequency resolution data with 32 or 64 frequency bands logarithmically spaced from 4 Hz to 4 kHz [Cully *et al.*, 2008]. These new, high resolution routinely available spectral data products were used in this chapter to confirm ECH event signatures in case studies and while developing automatic selection criteria using FBK data. The Fluxgate Magnetometer (FGM) [Auster *et al.*, 2008] measures background magnetic fields. Three-second-resolution fluxgate spin-fit (FGS) magnetic field data are used to evaluate local electron cyclotron frequency, select DF events, and perform further statistical studies. The electrostatic analyzers (ESA) [McFadden *et al.*, 2008] measure plasma from a few eV up to 30 keV for electrons and up to 25 keV for ions, with a time cadence of 3 seconds. We use ESA data to exclude possible solar wind intervals from the database. The Solid State Telescope (SST) [Angelopoulos, 2008] measures distribution functions of superthermal particles in the 25 keV to 6 MeV energy range with three-second time resolution during fast survey. Combined ESA and SST partial moments are used to select injections and perform statistical studies.

### **3.3 Event Selection**

We first restrict THEMIS measurements spatially to only include measurements in the magnetotail:

(1) We exclude near-perigee data, when the radial distance of the probes is less than  $3 R_E$ .

Then we search for events for each orbital period (separated by perigee crossings), rather than each calendar day, to better categorize each ECH event. All data points in the magnetotail with  $X < -6 R_E$  (GSM coordinate system is used in this chapter, unless otherwise specified) are selected for further investigation.

(2) We exclude data points possibly outside the magnetosphere, when the radial distance of the probes is  $\geq 8 R_E$ , while the electron density is  $\geq 5 \text{ cm}^{-3}$ , the ion temperature  $\geq 1 \text{ keV}$ , and the X-component of the ion velocity is  $\leq -100 \text{ km/s}$ . In addition, we exclude observations made when probes were in Earth's shadow.

An example of enhanced ECH wave emissions captured by THEMIS probe P4 is shown in Figure 3.1. Spectrograms of wave electric field and magnetic field spectra intensity from FFF data are plotted (Figures 3.1d and 3.1e). The bottom magenta line shows the electron gyrofrequency,  $f_{ce}$ , determined from the measured ambient magnetic field; and the black lines above  $f_{ce}$  represent  $2f_{ce}$ ,  $3f_{ce}$ , and  $4f_{ce}$ . ECH wave emissions are seen in the first harmonic band around 17:03UT, as the probe approaches the magnetic equator, inferred from the small  $|B_x|$  values ( $\sim 5 \text{ nT}$ ),  $\sim 0.2 \text{ cm}^{-3}$  electron density, and the electron energy spectra being dominated by plasma sheet electrons in the energy range of 1 keV to 10s of keV. These emissions persist for about 15min before vanishing at  $\sim 17:19\text{UT}$ . We can see the ECH wave's most prominent feature is the wave electric field power between harmonics of electron gyrofrequency (Figure 3.1d), along with weak magnetic field fluctuations (Figure 3.1e), as consistently shown in previous observations [*Kennel et al.*, 1970; *Roeder and Koons*, 1989; *Meredith et al.*, 2009]. These ECH

wave signatures are also captured in the spectrograms of wave electric and magnetic field from FBK data (Figures 3.1f and 3.1g), with lower frequency resolution.

The first cyclotron harmonic band, between the cyclotron frequency and twice that frequency, usually contains the major power intensity of an ECH event [e.g., *Meredith et al.*, 2009], which is also shown in Figure 3.1d. Therefore in this study, we examine wave power in that band as representative of each event occurrence and intensity. From Figures 3.1d and 3.1e, we can see both FFF and FBK data successfully captured the first harmonic band of ECH emissions in this case, which has also been verified in tens of other selected events. But FFF data are only available since 1 May 2010 during the fast survey mode, ~12 hours per day, whereas FBK data are always available during these five tail seasons. We thus use FBK data in this study to select ECH events.

As shown in Figures 3.1f and 3.1h, observed ECH emissions can be intermittent in wave amplitudes. But these scattered emissions may belong to a same event in nature, with amplitudes modified by local plasma and magnetic field conditions. In order to investigate the correlation rate of ECH waves with injections or DFs, we need to categorize these scattered ECH emission points as events. After surveying several ECH events, we were able to find reasonable operational criteria to select ECH events in the spatially restricted database as follows:

- (1) Because ECH waves are confined near the equator, we focus on datasets in the central plasma sheet with plasma beta  $>0.5$ .
- (2) We search the database for power within an observationally defined frequency range, herein referred to as  $[f_{\min}, f_{\max}]$ , wide enough to encompass the first cyclotron harmonic

band but excludes geophysical noise from low frequencies.  $f_{\min}$ , intended to be below the local electron cyclotron frequency at the time of wave generation, is the largest of two gyrofrequencies: one calculated from the local northward magnetic field component ( $f_{ce_{B_z}}$ ) that approximates the equatorial magnetic field and a fraction (35%) of the gyrofrequency from the local total magnetic field ( $0.35f_{ce_{B_t}}$ ); when the northward magnetic field is close to zero, near the equator,  $0.35f_{ce_{B_t}}$  is the larger of the two frequencies capping the ECH wave search from below to reasonable, non-zero values. This is particularly important given the large dynamic range of the magnetic field over the radial distance considered.  $f_{\max}$  is twice  $f_{ce_{B_t}}$ . All FBK bands within  $[f_{\min}, f_{\max}]$  are considered as probable ECH emissions. To further exclude EFI instrument noise in the FBK data, we select only data points with a peak wave electric field amplitude  $>0.1$  mV/m. Considering the electrostatic nature of ECH waves, we exclude electromagnetic emissions with significant magnetic component by further requiring that the peak magnetic field fluctuation be smaller than  $B_{\text{threshold}}$ .  $B_{\text{threshold}}$  is probe- and time-dependent, which varies between 4 pT and 5 pT.

- (3) We bundle the valid ECH emissions as selected above into ECH “events” by requiring that data samples separated by fewer than 5 minutes belong to the same ECH event. Then for each event, we search for the nearest point ahead of and after the bundle when the wave electric field amplitude drops below 0.03 mV/m and mark those as the start and end times of each event.

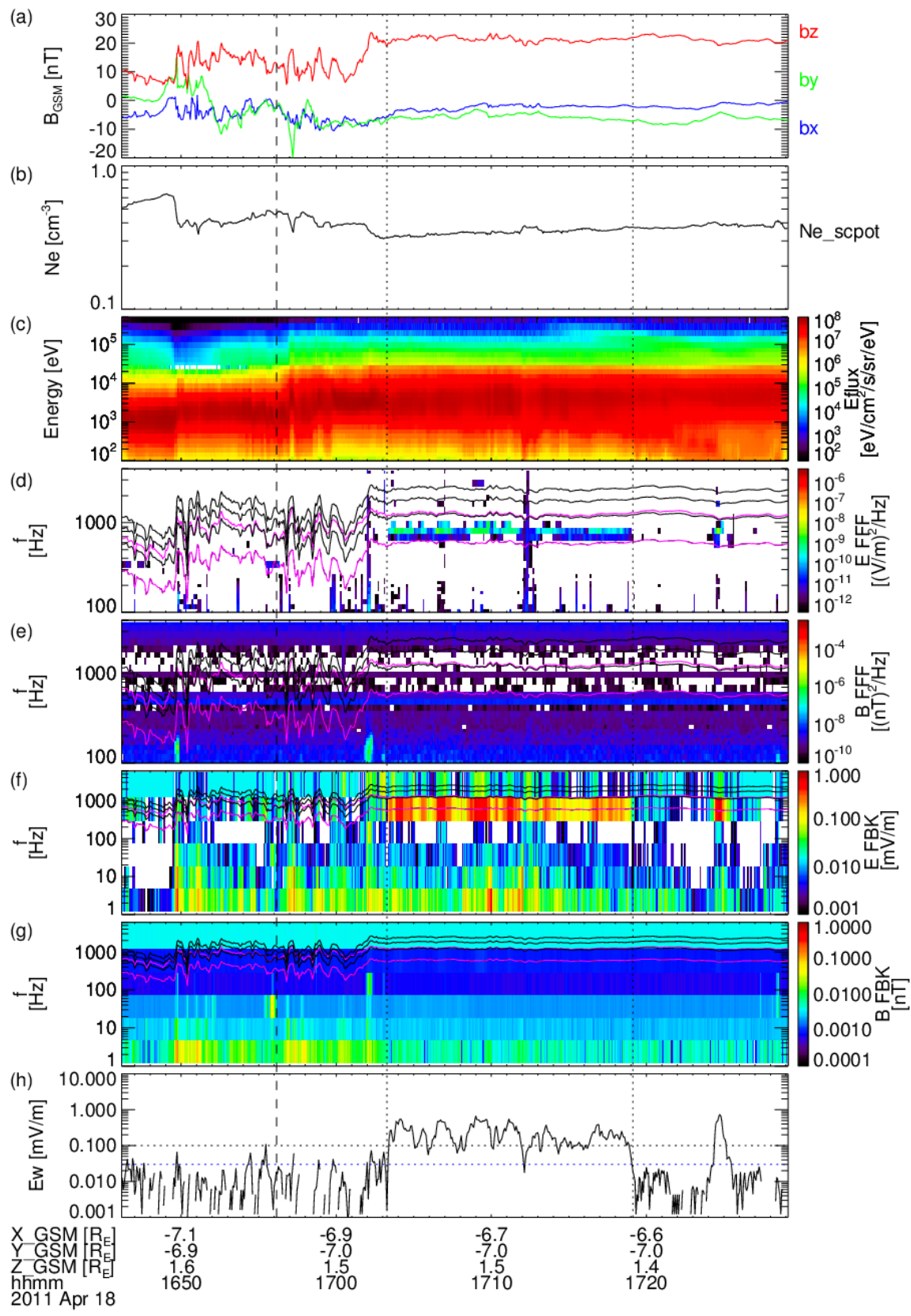


**Figure 3.1:** An example ECH wave event correlated with electron injections captured by THEMIS probe P4. The vertical dashed line denotes the start of the injection; the two vertical dotted lines denote the start and end of the ECH event. (a) The magnetic field in the geocentric solar magnetospheric (GSM) coordinate system, (b) the electron density inferred from the spacecraft potential, (c) the electron energy flux observed by the ESA and SST instruments, spectrograms of (d) wave electric field and (e) magnetic field power spectral density from the FFF data, spectrograms of (f) wave electric field and (g) magnetic field from the FBK data, (h) peak wave electric field amplitude within selected frequency bands (between two horizontal magenta lines). In panels (d) to (g), the overlaid black horizontal lines indicate  $4f_{ce}$ ,  $3f_{ce}$ ,  $2f_{ce}$  from top to bottom, whereas the magenta lines denote  $f_{min}$  and  $f_{max}$  adopted in selecting the first harmonic band of ECH emissions. In panel (h), the black (top) dotted horizontal line indicates the threshold of 0.1 mV/m used to selected scattered ECH emissions; the blue (bottom) dotted horizontal line indicates the threshold of 0.03 mV/m used to determine edges of each ECH event.

In Figure 3.1, we also show an example of automatically selected ECH event interval using the above criteria. The start and end time are marked by two vertical dotted lines. During this selected interval, ECH waves exhibit varied electric field amplitudes, from  $\sim 0.03$  mV/m at the edges to  $\sim 1$  mV/m at the peak, whereas the magnetic field fluctuations remain below 4 pT. Our criteria were able to automatically categorize ECH emissions under similar plasma and magnetic field conditions as a continuous event.

For each ECH wave event we search the spatially restricted database for possible electron injections 1 hour before to 1 hour after the start time of a wave event. Our selection criteria for injections are as follows:

- (1) To exclude electron flux increases caused by non-local activations, those common near the plasma sheet boundary, we restrict our database to the central plasma sheet (plasma beta >0.5).
- (2) Electron energy flux (after a 2-min running average) at three consecutive energy channels (within the 8-200 keV energy range) must be observed to increase >0.5 within 1 minute. We use the time stamp in the middle of this increase as the injection start time  $T_{0\text{ Injection}}$ .
- (3) To include dispersed injections into our database, we allow for a 5-min time difference for different energy channels observing the energy flux increase.
- (4) To exclude transient fluctuations in the energy fluxes, we require the flux at  $T_{0\text{ Injection}}+2\text{min}$  to be greater than that at  $T_{0\text{ Injection}}-2\text{min}$ .
- (5) The next injection must occur at least 10 min after the selected injection.

A similar procedure was used to build the dataset of DFs that occurred 1 hour before to 1 hour after the start time of a wave event. To do that we used criteria developed by *Liu et al.* [2013]:

- (1) Z-component of magnetic field ( $B_z$ ), after three-point running average, must be observed to increase >0.5nT within 1 second, i.e.,  $dB_z/dt > 0.5\text{nT/s}$ . The first point that satisfies this  $B_z$  jump criterion was chosen as the DF start time,  $T_{0\text{ DF}}$ .
- (2) The maximum  $B_z$  in the  $T_{0\text{ DF}}$  to  $T_{0\text{ DF}}+30\text{s}$  time range must be at least 5 nT greater than that in the  $T_{0\text{ DF}}-30\text{s}$  to  $T_{0\text{ DF}}$  time range.
- (3) The maximum  $B_z$  in the  $T_{0\text{ DF}}$  to  $T_{0\text{ DF}}+30\text{s}$  time range must be greater than 5 nT.
- (4) The next DF must occur at least 3 min after the selected DF.

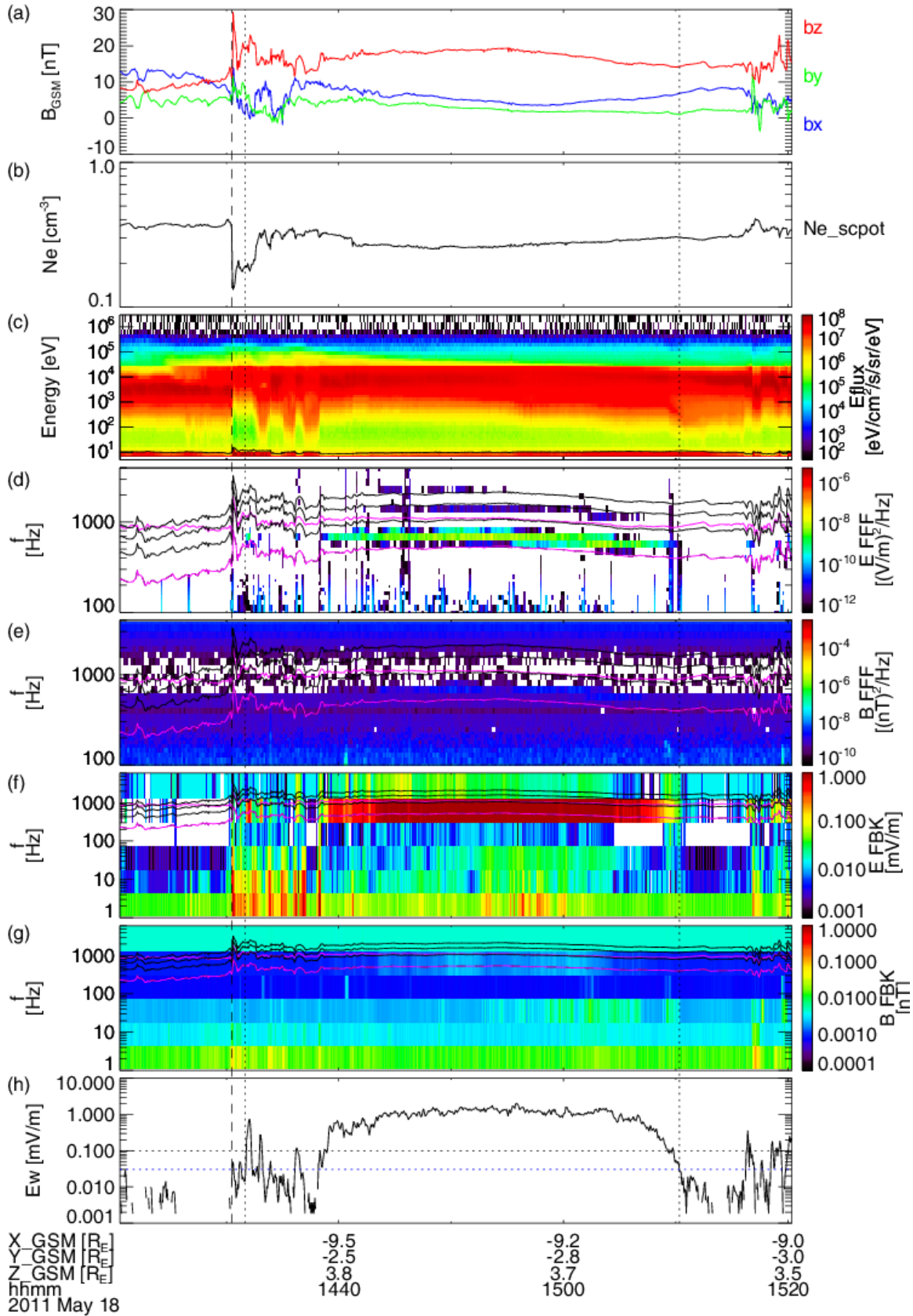


**Figure 3.2:** An example of ECH wave event correlated with DFs captured by THEMIS probe P3. The vertical dashed line denotes the start of the DF; the two vertical dotted lines denote the start and end of the ECH event. Panels are arranged in the same format as in Figure 3.1.

Dipolarization fronts are often observed in series [e.g., *Zhang et al.*, 2011]. *Liu et al.* [2013] restricted their database to exclude trailing DFs in a series, and focus on the leading DF in order to understand DF structure avoiding strong interactions with other DFs or the dipolarized magnetic field. However, because ECH waves may correlate better with subsequent DFs than with the leading DF, in this chapter we do not restrict the DFs to be isolated or leading DFs. We thus relax the *Liu et al.* [2013] restriction of an unperturbed magnetic field ahead of each DF, so as to include subsequent DFs in our database, not just the first in a series.

When multiple injections or DFs are related to one ECH wave event, we select the injection/DF closest to the start time of that event for the subsequent statistics. Figure 3.1 and Figure 3.2 show two examples of ECH wave events that are correlated with electron injections and DFs, respectively. The vertical dashed line ahead of ECH start time ( $T_{0\ ECH}$ ) denotes the onset of injection ( $T_{0\ Injection}$ ) in Figure 3.1, and the onset of DF ( $T_{0\ DF}$ ) in Figure 3.2. From these figures, we can see that the wave response time relative to these two activities is different: time delay of ECH relative to injections ( $T_{0\ ECH} - T_{0\ Injection}$ ) is  $\sim 5$ min, while the time delay relative to DFs ( $T_{0\ ECH} - T_{0\ DF}$ ) is shorter, within 1min.

The above criteria select 9221 ECH events in total. When the criteria of injections/DFs are applied to measurements from the same probe that observes the ECH event (referred to as single-probe database in the following correlation study), 5188 (56%) ECH events are correlated with

injections, while 4007 (43%) events are correlated with DFs. In addition, 2910 (32%) events are correlated with both injections and DFs, as tabulated in Table 3.1. Figure 3.3 shows the distribution of event durations for five different categories. The duration varies from ~8 sec to ~4 hr. The median event duration is 164 sec for injection-related events, 160 sec for DF-related events, and 188 sec for events related to both injections and DFs.

**Table 3.1:** Number of ECH events and percentage in four categories. Note that both-related is the category of ECH waves correlated with both injections and DFs; non-related is the category of ECH waves correlated with neither injections nor DFs.

Category	Number of Events	Percentage
Injection-related	5188	56%
DF-related	4007	43%
Both-related	2910	32%
Non-related	2936	32%

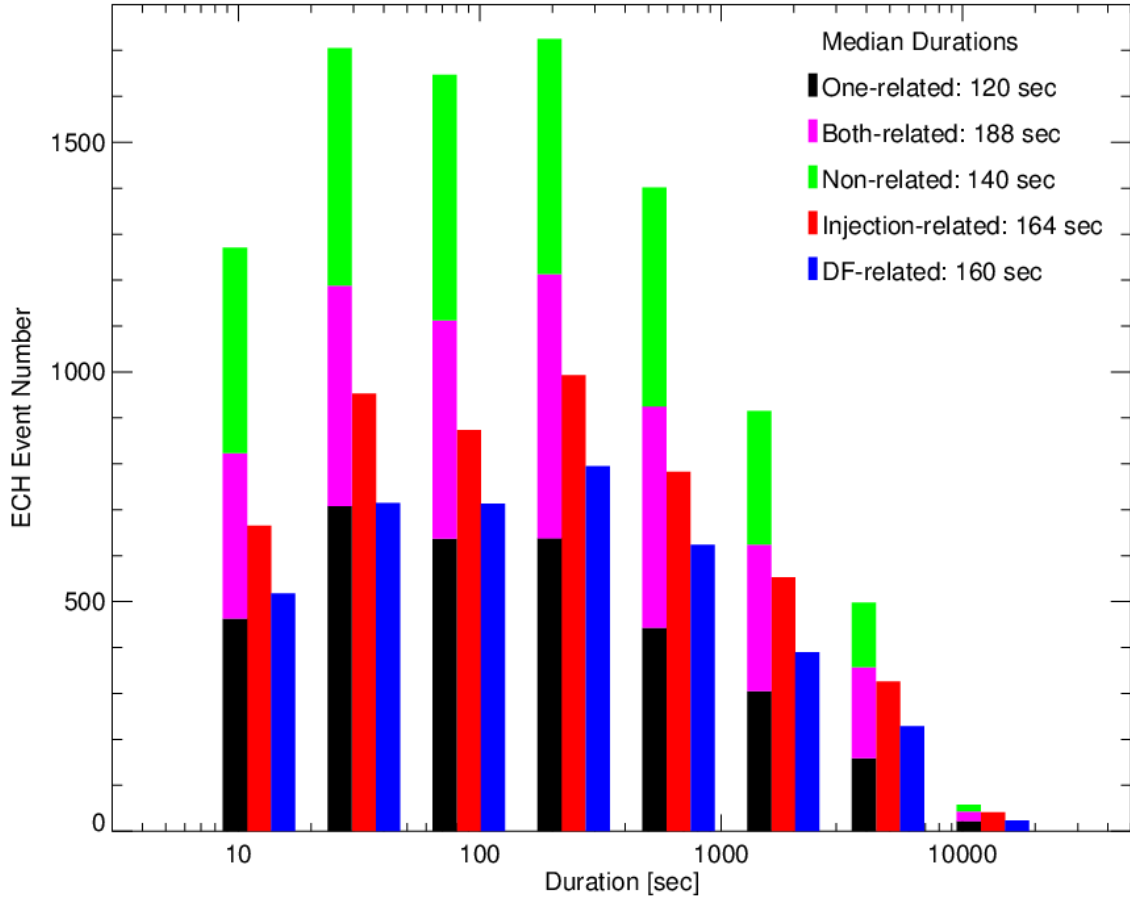
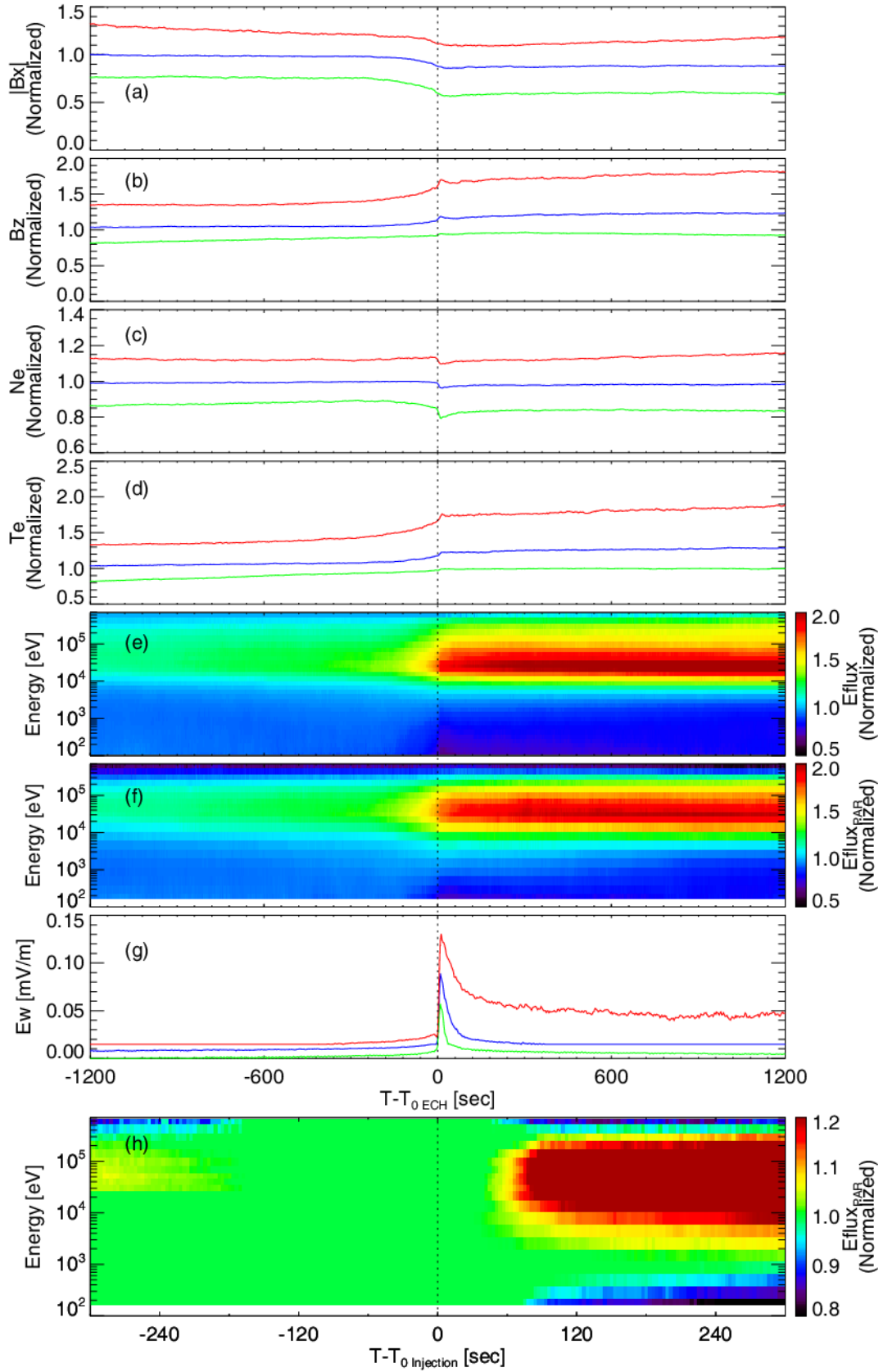


**Figure 3.3:** Distribution of ECH event duration in five categories. Note that one-related is the category of ECH waves observed in conjunction with a DF or an injection but not both; both-related is the category of ECH waves correlated with both injections and DFs.

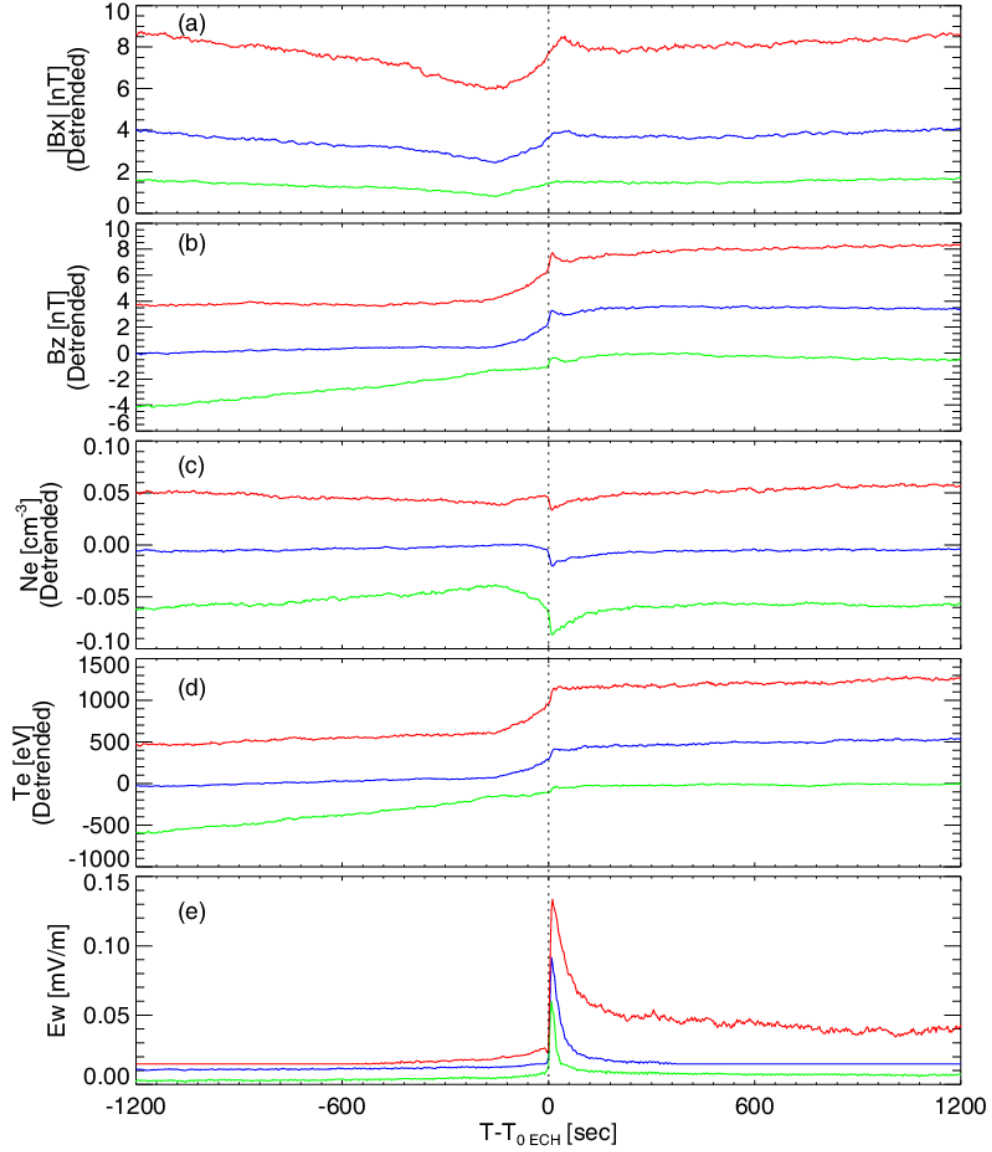
### 3.4 Statistical Results

In Figures 3.4 and 3.5, we show results from the superposed epoch analysis of critical quantities related to ECH events (from  $T_{0\ ECH}-20\text{min}$  to  $T_{0\ ECH}+20\text{min}$ ) that are correlated with injections (5188 out of 9221 events) and DFs (4007 out of 9221 events), respectively. Wave intensification (Figure 3.4g) occurs several minutes after increases in both omnidirectional and magnetic field

aligned (pitch-angle range  $0^\circ$ - $22.5^\circ$ ) energetic electron flux, accompanied by dipolarized magnetic field topology (simultaneous decrease in  $|B_x|$  and increase in  $B_z$  (Figures 3.4a and 3.4b)), decrease in electron density (Figure 3.4c), and increase in electron temperature (Figure 3.4d). In order to examine the variation of electron energy flux at different energy levels during injections, we also show in Figure 3.4h the superposed median change in magnetic field aligned (pitch-angle range  $0^\circ$ - $22.5^\circ$ ) electron energy flux with respect to the start time of an injection (from  $T_{0\text{Injection}}-5\text{min}$  to  $T_{0\text{Injection}}+5\text{min}$ ). The  $\sim 1\text{min}$  time lag between actual energy flux increases and  $T_{0\text{Injection}}$  is because we use the 2-min smoothed data in selecting injections (to avoid scatter). From this plot, we can see that during injections, field-aligned energy fluxes are enhanced over a wide range of energies (from  $\sim 1\text{ keV}$  to  $\sim 300\text{ keV}$ ). This supports our hypothesis that along with injected energetic electrons, lower energy electron (resonant with ECH waves) fluxes also intensify, which may contribute to the wave growth after electron injections. For ECH events correlated with DFs, as illustrated in Figure 3.5, wave intensification (Figure 3.5e) occurs about two minutes after the appearance of DF signatures: density decrease (Figure 3.5c), temperature increase (Figure 3.5d), and asymmetric bipolar variations in  $|B_x|$  (Figure 3.5a) and  $B_z$  (Figure 3.5b).



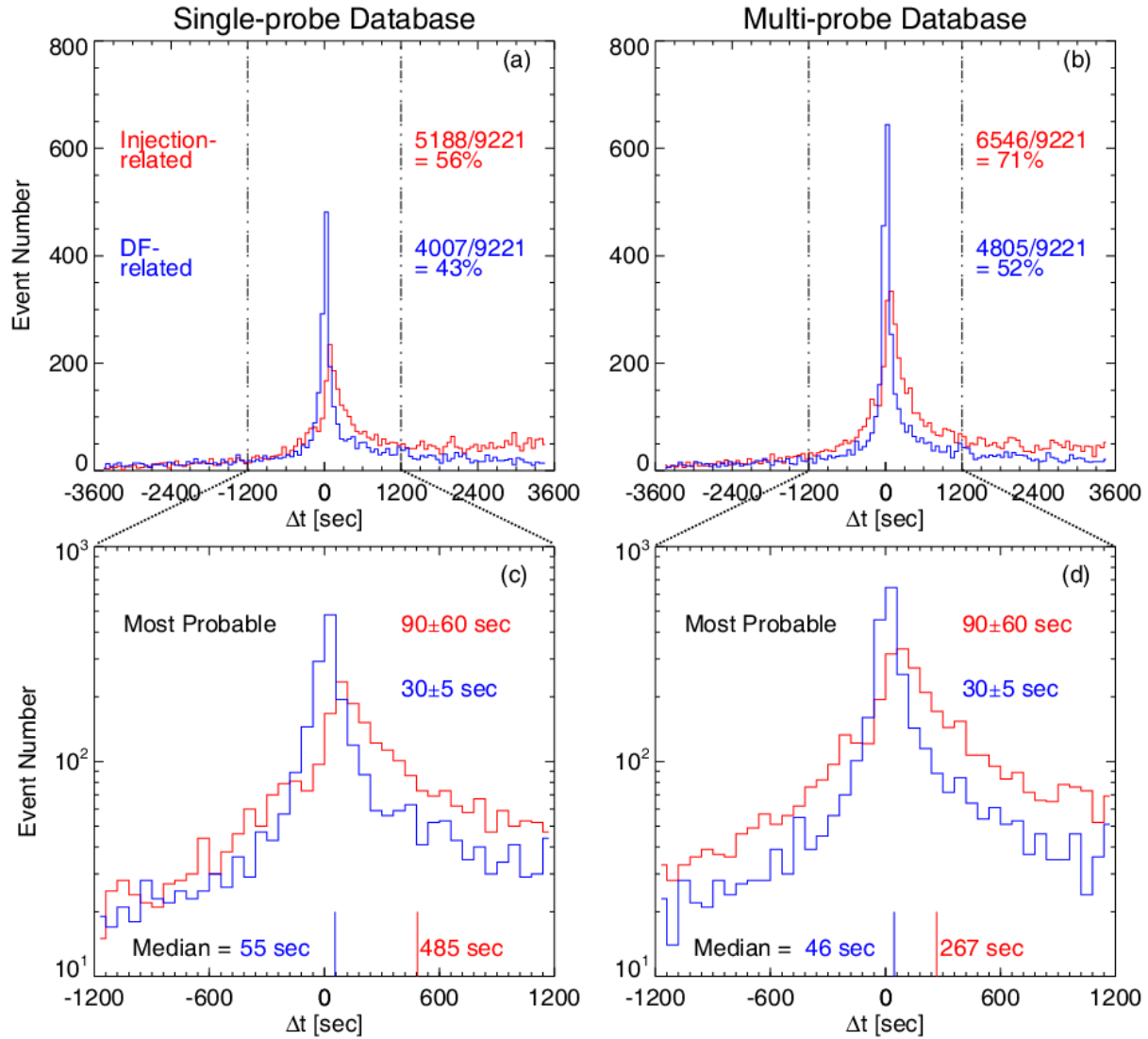
**Figure 3.4:** Superposed epoch analysis of (a) the magnetic field X component's absolute value, (b) the magnetic field Z component, (c) the electron density, (d) the electron temperature, (e) the electron omni-directional energy flux, (f) the magnetic field-aligned (pitch-angle range  $0^\circ$ - $22.5^\circ$ ) electron energy flux, (g) the amplitude of the wave electric field (peak value if multiple frequency channels involved) from FBK data, and (h) the median magnetic field-aligned (pitch-angle range  $0^\circ$ - $22.5^\circ$ ) electron energy flux. The dotted vertical line in panels (a)-(g) indicates the start of an ECH event, whereas the dotted vertical line in panel (h) indicates the start of an injection. Three curves in panels (a)-(d) and (g) represent the upper quartile (red), median (blue), and lower quartile (green) of the superposed data. Panels (e) and (f) show the median of the electron energy flux after a three-point-average in energy. The color scale in panel (h) is intentionally left saturated to better display different behaviors of the energy flux at different energy levels. This figure only includes ECH wave events correlated with injections (5188 events). Quantities in (a)-(f) and (h) are normalized to their median values in the time range  $T_{0\text{ Injection}}-2\text{min}$  to  $T_{0\text{ Injection}}-1\text{min}$ .



**Figure 3.5:** Superposed epoch analysis of (a) the magnetic field x component’s absolute value, (b) the magnetic field z component, (c) the electron density, (d) the electron temperature, and (e) the amplitude of the wave electric field (peak value if multiple frequency channels involved) from FBK data. The dotted vertical line indicates the start of an ECH event. Three curves in each panel represent the upper quartile (red), median (blue), and lower quartile (green) of the superposed data. This figure only includes ECH wave events correlated with DFs (4007 events). Quantities are detrended with their average values of the time range  $T_{0,DF}-3\text{min}$  to  $T_{0,DF}-2\text{min}$ .

As discussed in the introduction section of this chapter, it is possible that drifting electrons injected by a non-local source can contribute to the wave growth along their paths. To avoid biases from using single-point detections of injections/DFs, we also searched data from the other two probes (as opposed to the probe that observes ECH wave events) for injections and DFs in the same timeframe, when the inter-probe separation in both X and Y directions was within  $2 R_E$  (consistent with spatial scales of injection-correlated flow bursts and dipolarized flux bundles [Angelopoulos *et al.*, 1997; Nakamura *et al.*, 2004]). We refer this database as multi-probe database, which is only used to confirm the correlation rate in a comprehensive way.

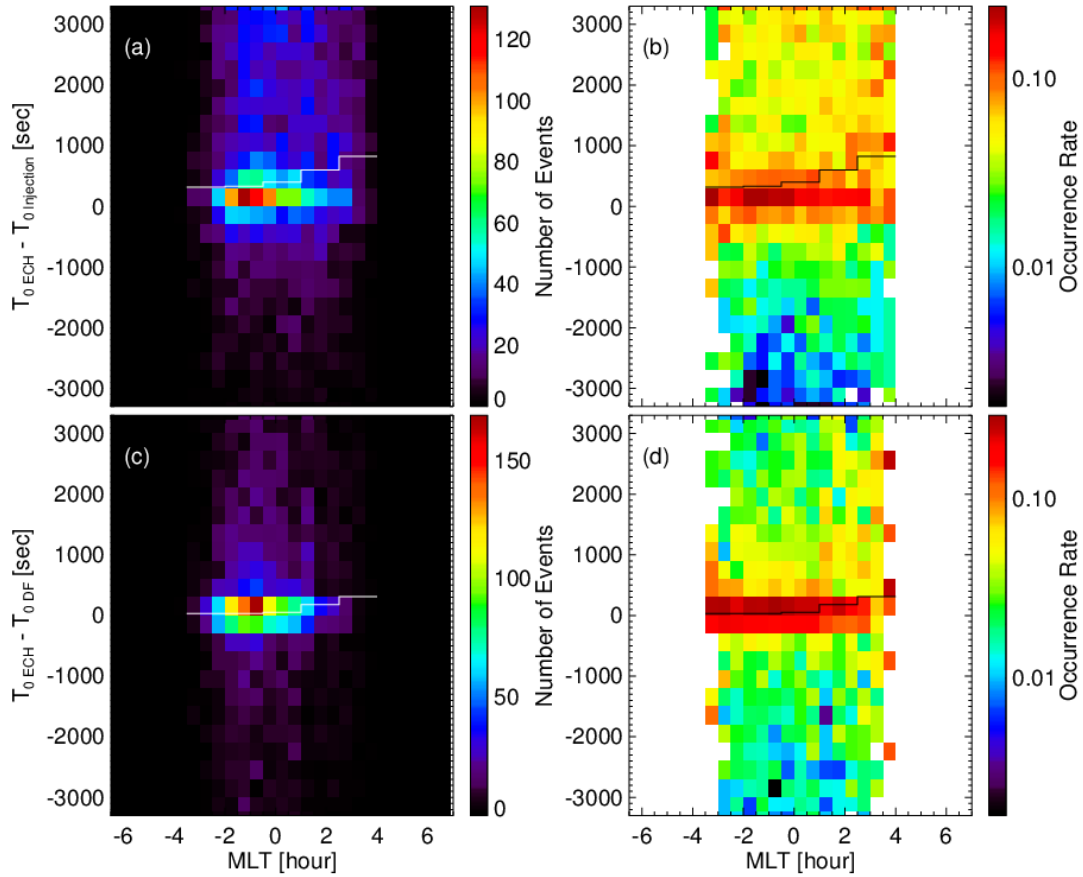
To quantitatively investigate the temporal correlation between ECH waves, injections, and DFs, we examined the time shift between the onsets of ECH waves, injections, and DFs, observed on the same probe or multiple probes. Results are shown in Figure 3.6. From Figure 3.6a, we can see that 56% of ECH events are correlated with injections and 43% are correlated with DFs for the single-probe database; these correlation rates increase to 71% for injection-related events and 52% for DF-related events in the multi-probe database. The number of events maximizes at around  $\Delta t=0$  (shown in both Figures 3.6a and 3.6b), implying a close relationship between injections/DFs and ECH events. Figures 6c and 6d show histograms of ECH events within a  $\pm 20$  min time lag for single-probe and multi-probe databases, respectively. As shown in both Figures 3.6c and 3.6d, the time lag of ECH events relative to injections is longer than that relative to DFs. It is generally longer in the single-probe database than in the multi-probe database, probably due to the finite spatial scale of DFs and the drift of injected electrons. For the single-probe database, the median time lag for ECH events relative to injections is 485 sec; the median time lag for DF-related ECH events is 55 sec. For both databases, the most probable time lag of ECH events is 90 sec relative to injections and 30 sec relative to DFs.



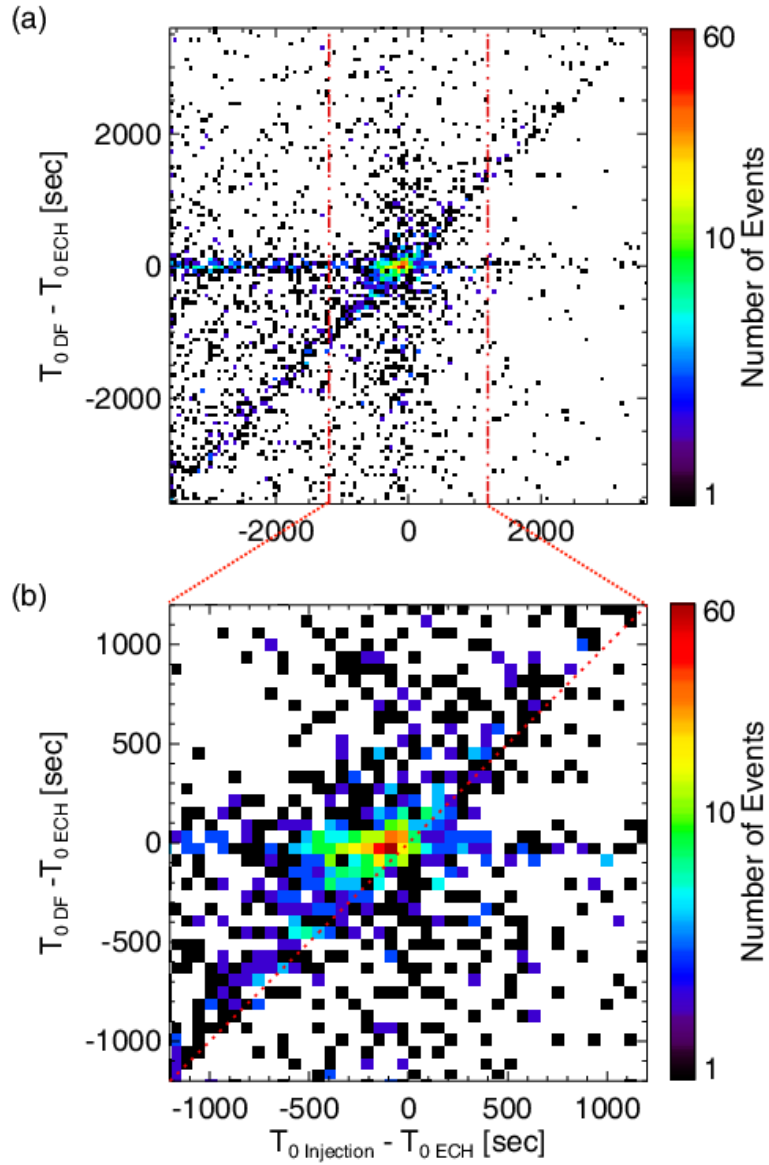
**Figure 3.6:** Histograms of time shift for ECH wave events correlated with injections (red) and DFs (blue) for the single-probe database (a and c) and the multi-probe (b and d) database. Figures c and d are enlarged versions of  $\pm 20$  min from Figures a and b respectively, with vertical bars displaying median time lag of ECH events relative to injections and DFs.

Figure 3.7 shows MLT distributions (single-probe database used hereafter, unless otherwise specified) of the temporal correlations between ECH waves, injections, and DFs. From Figure 3.7a and 3.7c, we can see that injection/DF-correlated ECH events occur preferentially in the pre-midnight sector, from ~22MLT to midnight, which is consistent with the distribution of injections and DFs from previous statistical studies [*Birn et al.*, 1997a; *Gabrielse et al.*, 2014; *Liu et al.*, 2013]. Figure 3.7a and Figure 3.7b also show that the time lag of ECH waves relative to injections increases from ~300 sec (21-23MLT) to ~800 sec (2-4MLT); Figure 3.7c and Figure 3.7d show that ECH response time relative to DFs varies from ~20 sec at pre-midnight (21-23MLT) to ~300 sec at post-midnight (2-4MLT).

For ECH waves correlated with both DFs and injections, we also examined the preferred sequence of observing these activities. As shown in Figure 3.8a, the nominal ECH wave time lag relative to injections and DFs is <20 min. Figure 3.8b demonstrates that injections tend to occur first, 90 sec (most probable time shift) ahead of ECH waves; DFs happen 60 sec later, followed by ECH waves 30 sec later.



**Figure 3.7:** Distribution of ECH event response time lags for different magnetic local times (MLT, in units of hour, categorized by the median MLT value of each event), shown for injection-related (upper) and DF-related (lower) ECH events. Color bar denotes number of events for Figures a and c, occurrence rate (normalized to total number of events within each MLT bin) for Figures b and d. The overlaid black/white lines indicate median time shift of ECH events relative to injections and DFs for each MLT bin, wherever total number of events is statistically abundant (greater than 10% of peak event number within a certain MLT bin).



**Figure 3.8:** Time delays of ECH wave onset relative to injections and DFs. Figure b is an enlarged version of  $\pm 20$ min from Figure a. The overlaid red dotted line indicates identical time shift for ECH waves relative to injections and DFs.

### 3.5 Summary and Discussion

Using three comprehensive databases of ECH wave events, injections, and DFs, we statistically investigated the temporal correlation between these three activities in the magnetotail. We built a database of ECH wave events based on the local gyrofrequency paying special attention to exclude low-amplitude noise and categorized ECH emissions as events rather than as scattered points in order to correlate wave emission instances with other dynamic conditions. Multi-point observations from THEMIS facilitate comprehensive databases for injections and DFs to investigate correlations. With these databases, we statistically established a temporal correlation between ECH waves, injections, and DFs: 71% of ECH events are correlated with injections and 52% are correlated with DFs (Figure 3.6). The median time lag for ECH events relative to injections is  $\sim 500$  sec; the median time lag for DF-related ECH events is  $\sim 60$  sec.

In addition, we examined the variation of ECH response time with MLT. The time lag of ECH events relative to injections increases from  $\sim 300$  sec at the pre-midnight region to  $\sim 800$  sec at the post-midnight region (Figure 3.7a and 3.7b), which is in agreement with the working hypothesis of a causal relationship between ECH wave intensification and downward drifting electrons from injections.

As shown in the superposed epoch analysis (Figure 3.4h), along with injected energetic electrons (in the tens to hundreds of keV energy range), field-aligned energy fluxes in lower energy electrons (down to  $\sim 1$  keV) are also enhanced. The accompanying lower energy electrons are at the resonant energy levels (hundreds to several thousand eV) with ECH waves. Being primarily in the field-aligned direction, this enhancement would both increase the resonant electron density and lead to sharper velocity-space gradients in electron distributions near the

edge of the loss cone, contributing to local wave growth. On the other hand, injected electrons are capable of changing local plasma conditions (Figures 3.4c and 3.4d), which may modify the local plasma dispersion relation, wave propagation and amplification. According to the parametric study by *Ashour-Abdalla et al.* [1979], it is possible that decreased density and temperature ratios between cold and hot electrons resulting from injections may further expand the unstable range of non-convective region for ECH waves in parameter space, promoting fast amplification of these waves. The more dipolarized field topology after the passage of DFs (Figures 3.5a and 3.5b), as expected from previous statistical studies of DFs [*Liu et al.*, 2013], is in qualitative agreement with our premise that DFs can result in suppressing latitudinal confinement of the waves. These mechanisms will be further investigated using modeling in a follow-up study.

For ECH waves that are correlated with both DFs and injections (32% of ECH events), we investigated the relative sequence in which each activity was observed. As shown in Figure 3.8b, injections are observed first, followed by DFs after 60 sec, which lead to wave intensification 30 sec later. This sequence implies that ECH wave intensification requires the presence of both a dipolarized flux tube and an enhancement in resonant electron flux near loss cone. The 22% of ECH events in the multi-probe database that are correlated with neither injections nor DFs, might be related to wave propagation away from their intensification region. The increasing wave response time from pre-midnight to post-midnight region (Figure 3.7) may indicate it is possible that as injected electrons drift downward (energetic electrons accompanied with resonant energy electrons), away from their source, they can still increase resonant electron fluxes at the loss cone edge, thereby contributing to the ECH wave intensification along their drift paths. But due to extended dispersions of flux increases at different energy levels or the crude angular resolution

of particle instruments, drifting electrons may not exhibit distinguishably sharp injection signatures as in near the injection source. This will be further investigated in future multi-spacecraft studies.

Recent statistical and theoretical modeling studies [*Ni et al.*, 2011a, 2012a; *Zhang et al.*, 2013] on ECH waves have reinforced the potential importance of these waves in driving diffuse aurora, especially in the middle to outer magnetosphere (beyond  $\sim 8 R_E$ ). By numerically modeling the interaction between electrons and ECH waves, *Zhang et al.* [2013] evaluated the expected wave amplitude during quasi-steady state (nominally quiet conditions). Their results suggested that ECH waves may exist below the sensitivity of present day instrumentation and may be responsible for a low-intensity drizzle, which explains the contradiction between the presence of diffuse auroral precipitation at higher latitudes (up to about  $70^\circ$  MLAT) [*Newell et al.*, 2009, 2010] and the relative scarcity of ECH waves in high L-shells ( $> \sim 12$ ) [*Ni et al.*, 2011a]. On the other hand, our results indicate that during active geomagnetic conditions, intensified ECH waves are observed in association with injections and DFs. This is also consistent with higher wave amplitude and occurrence rate in the pre-midnight region during active conditions reported in previous statistical results [*Ni et al.*, 2011a]. In addition, *Newell et al.* [2010] showed that the diffuse aurora energy flux increases significantly during high solar wind driving conditions and expands to a broader latitudinal and longitudinal range. The enhanced diffuse aurora precipitation in the higher latitudes and pre-midnight region agrees with intensified ECH waves reported in this study, correlated with injections and DFs. Specific contributions of ECH waves to diffuse aurora precipitation will be further studied in future quantitative modeling using statistical characteristics of plasma and magnetic field environments.

However, it may be counter-intuitive to associate DFs and related injections, which known to drive field aligned currents [e.g., *Liu et al.*, 2013] and discrete aurora [e.g., *Nakamura et al.*, 2001; *Nishimura et al.*, 2010], with diffuse auroras that are featureless. Diffuse aurora exists during various geomagnetic conditions, but it intensifies significantly during active times [*Petrinec et al.*, 1999]. Part of these active diffuse auroras, especially at high MLATs may occur in the aftermath of injections and DFs. Even in the absence of field aligned currents, DFs and related injections can also create plasma sheet conditions favorable for wave growth in their aftermath, including the reduced field line curvature and increased energy flux in a larger volume. Due to the distortion of magnetic field topology at higher L-shells ( $>\sim 8 R_E$ ), it is possible that DFs and related injections lead to the substorm wedgelets in the dusk while contributing to the featureless diffuse aurora precipitations in the dawn side of the wedgelets.

These intensified ECH emissions during dynamic plasma sheet conditions grow due to the same velocity space anisotropy as the emissions approaching quasi-steady state, namely, the loss-cone of the hot plasma sheet electrons. Investigating the mechanism leading to the wave intensification in the aftermath of electron injections, affecting local growth rates, and DFs, affecting wave propagation, can therefore help understand the wave generation during quiet times as well. This is especially true considering that quasi-steady state waves in outer magnetosphere may not be detectable due to their small amplitude.

## CHAPTER 4

### Extent of ECH Wave Emissions

The exact role of ECH waves in driving diffuse aurora has been controversial for many years. Using THEMIS observations from five magnetotail seasons, we investigate the occurrence rate distribution of ECH waves and the extent of individual wave intensifications under various plasma sheet conditions. Both are critical for modeling these waves' contributions to electron scattering and to diffuse auroral emissions. As shown in Chapter 3, we are able to categorize ECH emissions into quiet and active time events. By examining the occurrence rate distribution and extent of ECH waves for active and quiet plasma sheet separately, we expect to improve our understanding of wave excitation under diverse magnetotail conditions. We also investigate the mechanism leading to the different Z-extents under various plasma sheet conditions by modeling the wave power distribution as a function of distance from the neutral sheet. Our results suggest that ECH intensification following dipolarizing flux bundles is in part due to increased  $R_c$ , which enables intensification to higher amplitudes over a larger volume, explaining the increased occurrence rate and extent of active-time wave events.

Section 4.1 briefly introduces the motivation for a finer spatial distribution of ECH waves in the context of studying these waves' contributions to diffuse aurora. We describe the database and how we evaluate the extent of selected ECH waves in Section 4.2. Our observational results are shown in Section 4.3. In Section 4.4, we model the extent of these waves under different magnetic field configurations using the HOTRAY ray-tracing code to examine the relationship

between the waves' extent and field topology. We summarize and discuss the results in Sections 4.5 and 4.6.

## 4.1 Introduction

As discussed in Section 1.5.3, the exact role of ECH waves in diffuse auroral precipitation has been a debate for a long time [e.g., *Kennel et al.*, 1970; *Lyons*, 1974; *Belmont et al.*, 1983; *Roeder and Koons*, 1989; *Horne and Thorne*, 2000; *Horne et al.*, 2003; *Meredith et al.*, 2009]. Recent studies have shown that ECH waves could be the dominant driver of diffuse auroral precipitation in the middle to outer magnetosphere [*Ni et al.*, 2011a, 2012a; *Zhang et al.*, 2013], beyond  $\sim 8 R_E$ , where high-latitude diffuse aurora [*Newell et al.*, 2009, 2010] maps to.

To better examine the importance of ECH waves in driving diffuse aurora, quantitative evaluation of plasma sheet electron interactions with a more realistic wave model is required. The spatial distribution characteristics of ECH emissions have been reported using CRESS and THEMIS data [*Meredith et al.*, 2009; *Ni et al.*, 2011a]. However, these studies only utilized single spacecraft to evaluate the occurrence rates of these waves in space, without distinguishing the source location of each emission. Modeling the scattering effects of ECH waves and evaluating the specific contribution of ECH waves to diffuse aurora requires understanding of the instantaneous wave spatial distribution with finer spatial resolution than can be derived from the single spacecraft occurrence rate studies. Since intense waves appear to be absent most of the time and are likely localized, at least in  $Z$  (relative to the neutral sheet), a relative scale (established by two spacecraft) is far more informative than the occurrence rate spatial distribution established by single spacecraft.

The precipitated electron energy flux within the diffuse aurora is most intense from pre-midnight well into the morning hours [Newell *et al.*, 2009]. But which characterization of ECH waves at the equator— as continuous, ubiquitous, small-amplitude emissions or impulsive, localized, strong ECH waves— contributes to such a precipitation pattern? And what do these characterizations tell us about the generation mechanism of these waves? Investigating directly the extent of ECH waves, therefore, can provide new insights into the origin of diffuse aurora.

Using the CRRES wave data, Meredith *et al.* [2000] demonstrated that ECH waves intensify significantly (with amplitudes at the magnetic equator above 1mV/m) following substorm injections in the inner magnetosphere. Using THEMIS data in the mid-tail region, Zhang and Angelopoulos [2014] established a temporal correlation between ECH wave events (continuous intervals of wave activity) and local plasma sheet activations, exemplified by electron injections or dipolarization fronts (DFs). This correlation suggests that the aforementioned phenomena can create plasma sheet conditions favorable for ECH wave growth in their aftermath, possibly due to reduced field line curvature and increased energy flux within a larger volume. Wave events not correlated with local injections and DFs at the spacecraft within an hour of wave observation, may be related to dawnward-drifting electrons from a nearby injection. We hypothesize that along with these injected energetic electrons, resonant electron fluxes are also enhanced at the edge of the loss cone, contributing to ECH wave intensification along their drift paths. Dipolarization fronts and related injections are known to drive field-aligned currents [e.g., Liu *et al.*, 2013] and discrete aurora [e.g., Nakamura *et al.*, 2001; Nishimura *et al.*, 2010]. In order to associate them with featureless diffuse auroras, we speculate that auroral precipitation can be diffuse at one MLT-MLAT spot, while field-aligned currents may cause discrete aurora elsewhere (probably westward of the diffuse auroral precipitation). In fact, we note that the

Newell et al. study did not bin the precipitation data by activity index, but strictly by the type of spectrum observed, indicating that diffuse precipitation in that study could take place both during high AE index and concurrently with discrete precipitation (elsewhere in the auroral oval). Similarly, the plasma sheet can be locally “quiet” in that intense field-aligned currents associated with DFs are absent at the observing spacecraft. Even though nearby bursty bulk flows encompassing one or more dipolarization fronts can be occurring, locally the quiet plasma sheet may still be the driver of diffuse aurora. We therefore segregate locally active plasma sheet intervals (times of injections and DFs) from quiet plasma sheet intervals (no injections or DFs) and assume the latter represent quiet ionospheric conditions at the footprint. By examining the occurrence rate distribution and extent of ECH waves for active and quiet plasma sheet separately, we expect to improve our understanding of wave excitation under diverse magnetotail conditions.

With its prolonged residence in the plasma sheet, the THEMIS mission offers a unique dataset for investigating ECH wave extent in more detail. By looking at the correlation of wave intensity between multiple spacecraft with different configurations and at various distances relative to each other or to the neutral sheet, we estimate the extent of these waves (if present) in different dimensions. By modeling the wave extent under different magnetic field topologies, we obtain further clues to the mechanism leading to wave intensification during/after injections/DFs.

## **4.2 Database and Methodology**

In this chapter, we use the same ECH wave database as developed in Chapter 3, where we organized ECH wave observations into contiguous sample intervals, termed “events”, in order to investigate their correlation with injections and DFs. Our database includes 8753 ECH events in

the plasma sheet (refer to the near-neutral sheet region of the plasma sheet with plasma beta  $>0.5$ ) with durations varying from 8 sec to 3.9 hr, as shown in Figure 3.3. Because of the potentially significant variation in spacecraft separation during an ECH event, we use all individual data samples (at 4 sec resolution) within each wave event to investigate the spatial distribution and extent of ECH waves in this chapter. We use measurements from all five probes to show the spatial distribution of ECH waves from  $X=-6 R_E$  to  $X=-30 R_E$ . Because of the large separations between the inner (P3, P4, and P5) and the outer (P1 and P2) probes, which result in low correlation of wave intensities between inner and outer probes, we only use observations from the three inner probes to estimate the wave spatial scales.

We use observations from pairs formed by the three inner spacecraft. We select one spacecraft that observes ECH waves as the reference spacecraft. Then we separate the dual spacecraft observations according to whether the second spacecraft, assuming it has valid measurements, observes the waves at the same time. Within a certain spacecraft separation range, the ratio of samples of dual-spacecraft ECH observations to samples of single-spacecraft ECH observations (with the other spacecraft making valid plasma sheet measurements, and thus having the potential to capture the waves if they are present) gives us the occurrence rate of ECH waves captured by two spacecraft. We refer to these two databases of single- and dual-spacecraft ECH wave emission samples as the “initial database” and the “conjoint database”. The dual-spacecraft occurrence rate of ECH waves as a function of spacecraft separation in the X, and Y directions provides the ECH wave extent in each dimension. With regard to estimating the wave occurrence rate as a function of distance from the neutral sheet (DNS), we note that the plasma sheet flaps and twists, and its hinge point varies with activity. Therefore, no magnetospheric model can provide a good estimate of neutral sheet location. We thus fit the in-situ magnetic

field data to a Harris sheet model [Harris, 1962] and use the model DNS to estimate spacecraft location and hence spacecraft separation in the  $Z$  direction. In addition, we compute the plasma beta ( $\beta$ ), the thermal to magnetic pressure ratio, and treat the normalized beta difference ( $\Delta\beta/\beta$ ) between the spacecraft as a proxy of their separation in the  $Z$  direction.

### 4.3 Observation Results on ECH Wave Extent

We first examine the spatial distribution of the wave occurrence rates at each spacecraft. As evident from Figure 4.1c, the occurrence rate of ECH emissions in the XY plane (in aberrated GSM coordinates with a  $4^\circ$  aberration angle) has a slight dawnward preference within  $10 R_E$ , whereas ECH emissions are seen predominantly in the pre-midnight sector beyond  $10 R_E$ . This pre-midnight preference beyond  $10 R_E$  is correlated with higher geomagnetic activity (higher AE index, not shown here) in that region of the magnetotail. The occurrence rate of ECH emissions decreases with increasing distance from Earth, dropping to below 10% beyond  $15 R_E$ . We also show the occurrence rate of ECH emissions that are not correlated with injections or DFs in Figure 4.1d (detailed definitions of this correlation can be found in Chapter 3). Compared to Figure 4.1c, these non-related ECH emissions have a clear preference for the dawn sector within  $10 R_E$ .

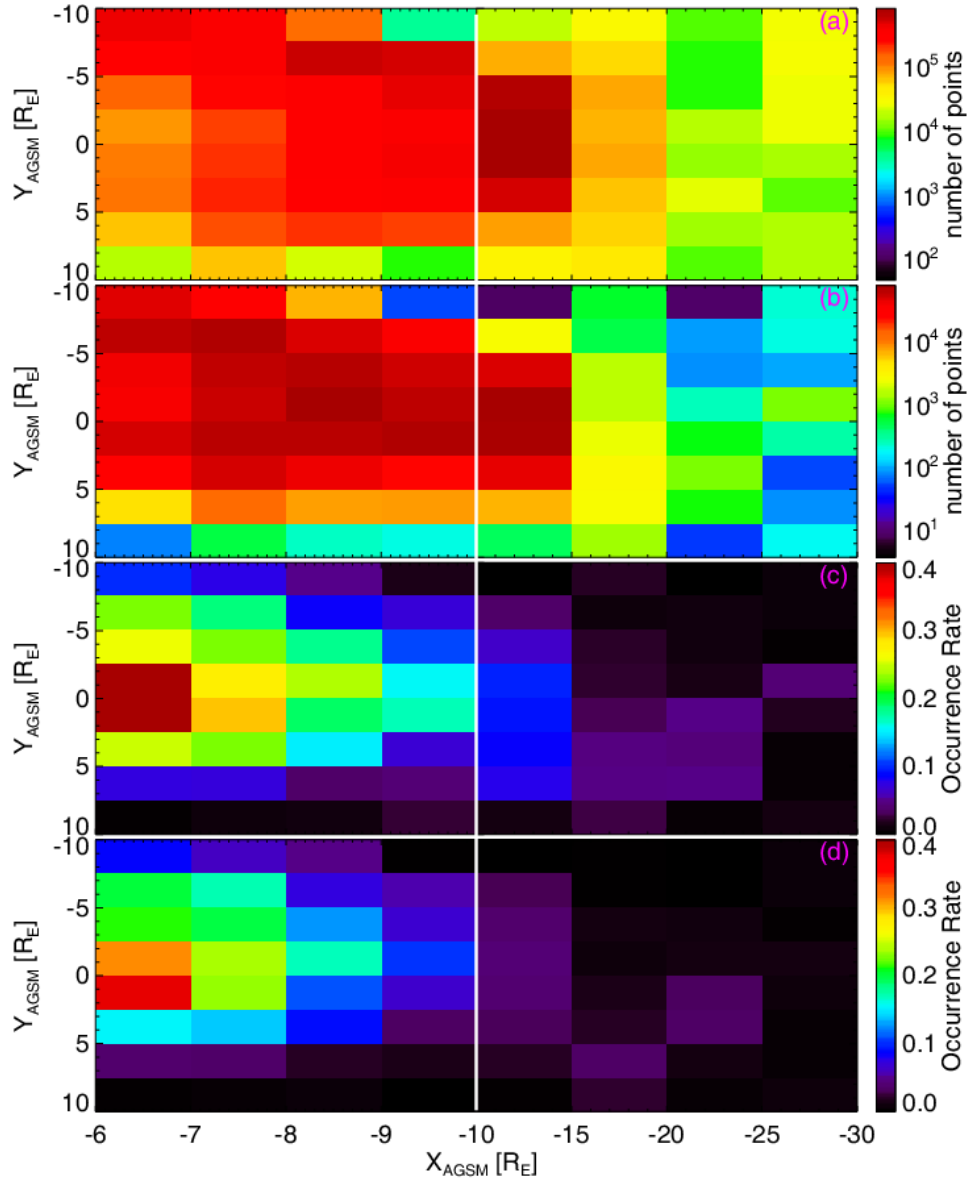


**Figure 4.1:** Distribution of (a) valid measurements (orbital distribution with valid EFI data within the central plasma sheet) and (b) ECH observations from single spacecraft in the XY plane (in aberrated GSM coordinates). (c) Occurrence rate of ECH emissions computed as the ratio of (b) to (a). (d) Occurrence rate of ECH emissions that are not correlated with injections or DFs. Note that the spatial resolution changes from 1  $R_E$  per tick on the left of the vertical white line to 5  $R_E$  per tick on its right.

We next examine the extent of ECH waves in the Z direction by recording the occurrence rate of dual-spacecraft observations for a certain Z-separation ( $\Delta Z$ ) between the two spacecraft. In order to reduce the variation of wave occurrence due to the finite Y-extent of the wave emission region, we restrict the spacecraft separation to be Z-dominated ( $|\Delta Z_{\text{GSM}}| > |\Delta Y_{\text{GSM}}|$ ) when examining the Z-extent. Figures 4.2a and 4.2b show the spatial distribution of samples in the initial database (when the reference spacecraft sees the ECH waves and the other spacecraft is able to but does not necessarily observe the waves) and in the conjoint database, in the X- $\Delta Z$  plane. Here  $\Delta Z$  was approximated by the difference of normalized distance to the neutral sheet (DNS) in a Harris sheet model fitted to the data. The normalization of DNS is with the current sheet thickness L. The ratio of the number of samples in the two databases is the occurrence rate of ECH emissions observed simultaneously at two locations separated by  $\Delta Z$ , at a given distance from Earth, X. That ratio is shown in Figure 4.2c (for normalized  $\Delta Z$  distances) and also in 4.2d (for absolute  $\Delta Z$  distances, without normalizing to the current sheet thickness). We can see that the occurrence rate of ECH emissions is higher when the second spacecraft is closer to neutral sheet (negative  $\Delta Z$ ) than the reference spacecraft. Conversely, the occurrence rate is lower when the second spacecraft is farther away from the neutral sheet (positive  $\Delta Z$ ). Figure 4.2c shows that the maximum extent of ECH emissions in terms of normalized DNS is  $\sim 0.5$ . In absolute distances the maximum scale is  $\sim 0.5 R_E$ .

In addition, we verify the Z-extent of ECH waves by using the relative change in plasma beta as a proxy of spacecraft separation in the Z direction. Figures 4.3a and 4.3b show the spatial distribution of samples in the initial database and conjoint database in the X- $\Delta\beta/\beta$  plane, where  $\Delta\beta/\beta$ , the normalized beta difference between two spacecraft, represents proximity to the neutral sheet. Consistent with Figures 4.2d and 4.2c, we can see the occurrence rate of ECH emission

capture (Figure 4.3c) is higher for the spacecraft closer to neutral sheet (positive  $\Delta\beta/\beta$  indicates negative  $\Delta Z$ ) than for the spacecraft farther away from the neutral sheet (negative  $\Delta\beta/\beta$  indicates positive  $\Delta Z$ ).

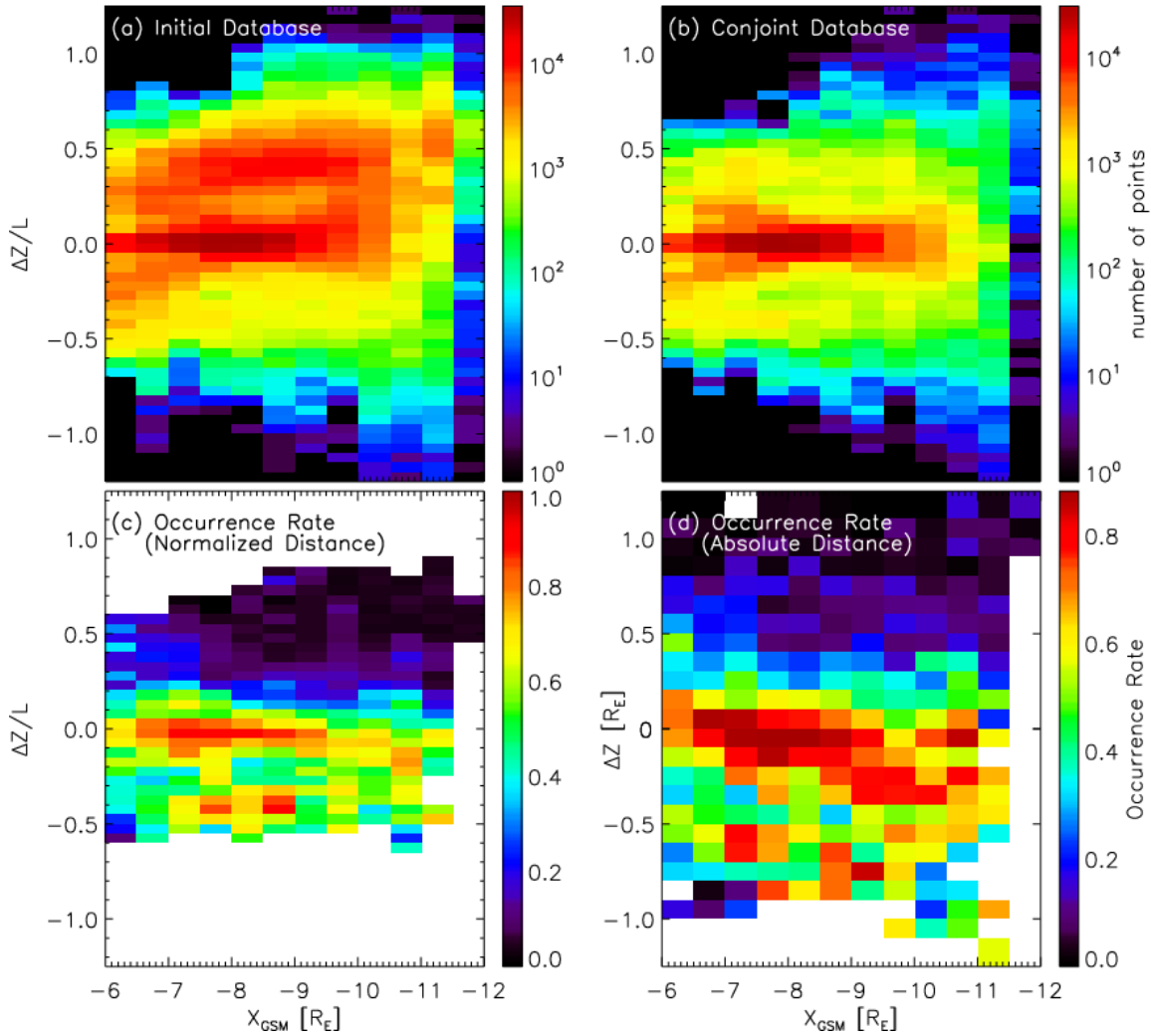


**Figure 4.2:** (a) Two-dimensional spatial distribution of dual-spacecraft measurements in the initial database, where one (the reference) spacecraft observes ECH waves and another (the second) spacecraft has valid measurements but may or may not observe the waves. The abscissa

shows the  $X_{\text{GSM}}$  location (in  $R_E$ ) of the reference spacecraft. The ordinate represents the spacecraft separation, as the difference in normalized distance to the neutral sheet estimated by fitting the magnetic field data at the two spacecraft to a Harris sheet model. Normalization of distance to the neutral sheet is with respect to the current sheet thickness  $L$ . A positive value indicates that the second (other) spacecraft is in the direction away from the neutral sheet, and a negative value indicates that it is closer to the neutral sheet than the reference spacecraft; (b) Spatial distribution of the dual-spacecraft measurements in the conjoint database, where both the reference spacecraft and the other (second) spacecraft capture ECH waves at the same time; (c) Distribution of occurrence rates of ECH waves determined by the ratio of data in (b) over (a); (d) Same as (c) except we used an absolute spacecraft distance in the  $Z$ -direction after determining the thickness of the neutral sheet by fitting the data to a Harris sheet model (also see text). Note that when the number of observations in the initial database was fewer than 300, the ratios are not shown, to increase the statistical significance of the results and avoid noise.

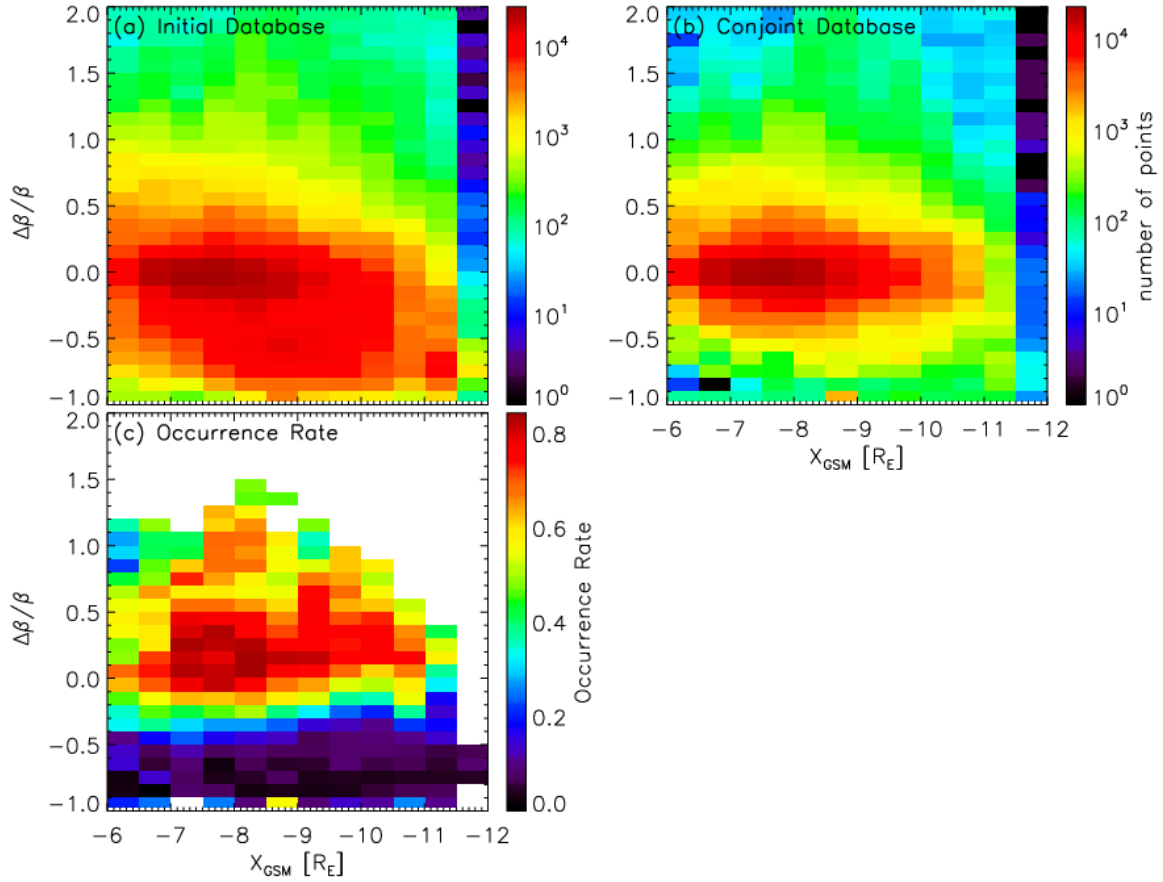


**Figure 4.3:** (a) Two-dimensional spatial distribution of dual-spacecraft measurements in the initial database, where one (the reference) spacecraft observes ECH waves and another (the second) spacecraft has valid measurements but may or may not observe the waves. The abscissa shows the  $X_{\text{GSM}}$  location (in  $R_E$ ) of the reference spacecraft. The ordinate represents the spacecraft separation, as the normalized beta difference ( $\Delta\beta$ ) between the two spacecraft. A negative value indicates that the second (other) spacecraft is in the direction away from the neutral sheet, and a positive value indicates that it is closer to the neutral sheet than the reference spacecraft; (b) Spatial distribution of the dual-spacecraft measurements in the conjoint database, where both the reference spacecraft and the other (second) spacecraft capture ECH waves at the same time; (c) Distribution of occurrence rates of ECH waves, determined by the ratio of data in

(b) over (a). Note that when the number of observations in the initial database was fewer than 300, the ratios are not shown, to increase the statistical significance of the results and avoid noise.

For better visualization and to compare different local plasma sheet activity conditions, we also show the occurrence rate of dual-spacecraft observations as a function of  $|\Delta Z|/L$  in line plots (Figure 4.4). From Figure 4.4a, we can see that the occurrence rate of observing simultaneous ECH emissions at two spacecraft drops to below 50% for spacecraft separations  $|\Delta Z|/L > 0.18$ ; DF-related waves exhibit a similar trend, with slightly higher occurrence rates at larger  $|\Delta Z|/L$ ; after excluding active plasma sheet conditions, i.e., ECH waves correlated with DFs (and injections), the occurrence rate decreases to below 50% when  $|\Delta Z|/L > 0.13$  ( $|\Delta Z|/L > 0.08$ ). This tendency for further equatorial localization of the waves with reduced local plasma sheet activity becomes clearer after normalizing the occurrence rates to the totals and peaks within each category. In Figures 4.4b and 4.4c, the DF-related, the non-DF, and non-related (both non-DF and non-injection) categories are increasingly peaked at the narrowest equatorial bin,  $|\Delta Z|/L < 0.05$ , with steeper falloffs.

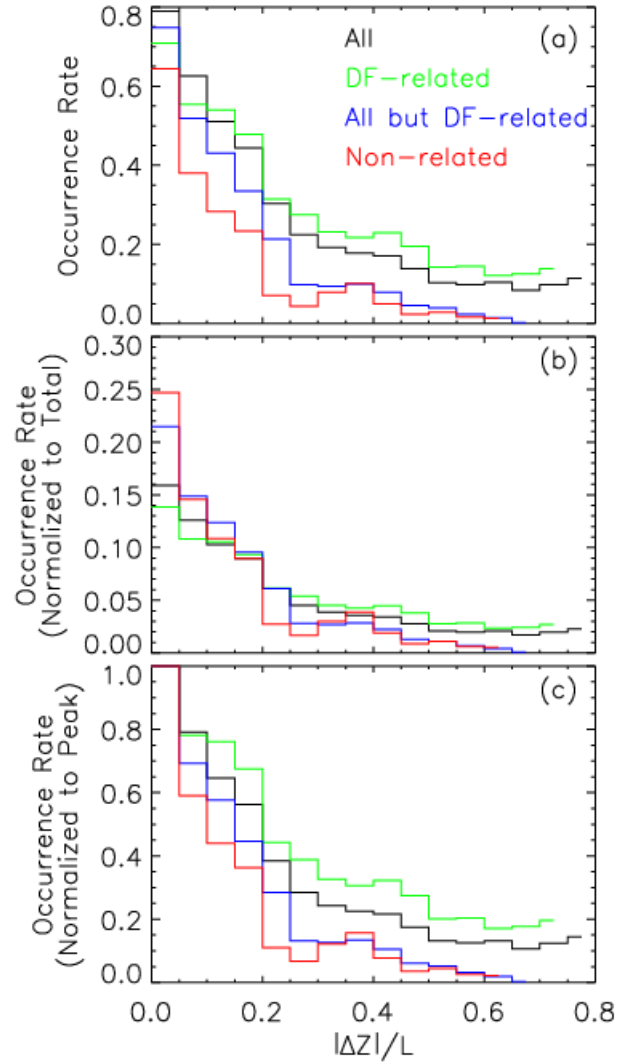


**Figure 4.4:** (a) Occurrence rate of dual-spacecraft observations of ECH waves as a function of  $|\Delta Z|/L$ ; normalized occurrence rate with (b) the total and (c) the peak value within each category. These two normalizations allow us to see the relative distribution of wave occurrence within each category. The four traces in each plot represent the result for the entire wave database (black), the DF-related waves (green), the waves not correlated with DFs (blue), and the waves not correlated with DFs or injections (red). Note that when the number of observations in the initial database within each category was fewer than 4000, the occurrence rates are not shown, to increase the statistical significance of the results and avoid noise.

Finally, we examine the extent of ECH waves in the X and Y directions for different subsets. To eliminate aliasing due to the finite Z-extent, we only use the portion of the data for which the spacecraft separation  $\Delta Z$  is negative, such that the other spacecraft is closer to the neutral sheet than the reference spacecraft. Figures 4.5a and 4.5b are histograms of the data in the initial and conjoint databases as a function of spacecraft separation in Y ( $\Delta Y_{\text{GSM}}$ ). As shown in Figure 4.5c, which is derived from the ratio of the data in Figures 4.5b and 4.5a, the occurrence rate of dual ECH observations decreases significantly for  $|\Delta Y_{\text{GSM}}| > 2R_E$  (for all four subsets), indicating that the Y-scale of these waves is  $\sim 2 R_E$ . The normalized occurrence rates (Figures 4.5d and 4.5e) decrease more rapidly with  $|\Delta Y_{\text{GSM}}|$  for non-related ECH waves than for the entire ECH database. In order to eliminate the variation of wave occurrence with Y-separation, we further restricted the database with  $|\Delta Y_{\text{GSM}}| \leq 2R_E$  when examining the X-extent. Figures 4.5f and 4.5g are histograms of the data in the initial and conjoint databases as a function of spacecraft separation in X ( $\Delta X_{\text{GSM}}$ ). As shown in Figure 4.5h, the occurrence rate of dual ECH observations and simultaneous DF-related wave observations does not change much for  $|\Delta X_{\text{GSM}}| \leq 4R_E$ . However, after excluding ECH waves correlated with DFs (and injections), we see a sharp decrease in the occurrence rate for  $|\Delta X_{\text{GSM}}| > 1R_E$ , in Figures 4.5h, 4.5i, and 4.5j.

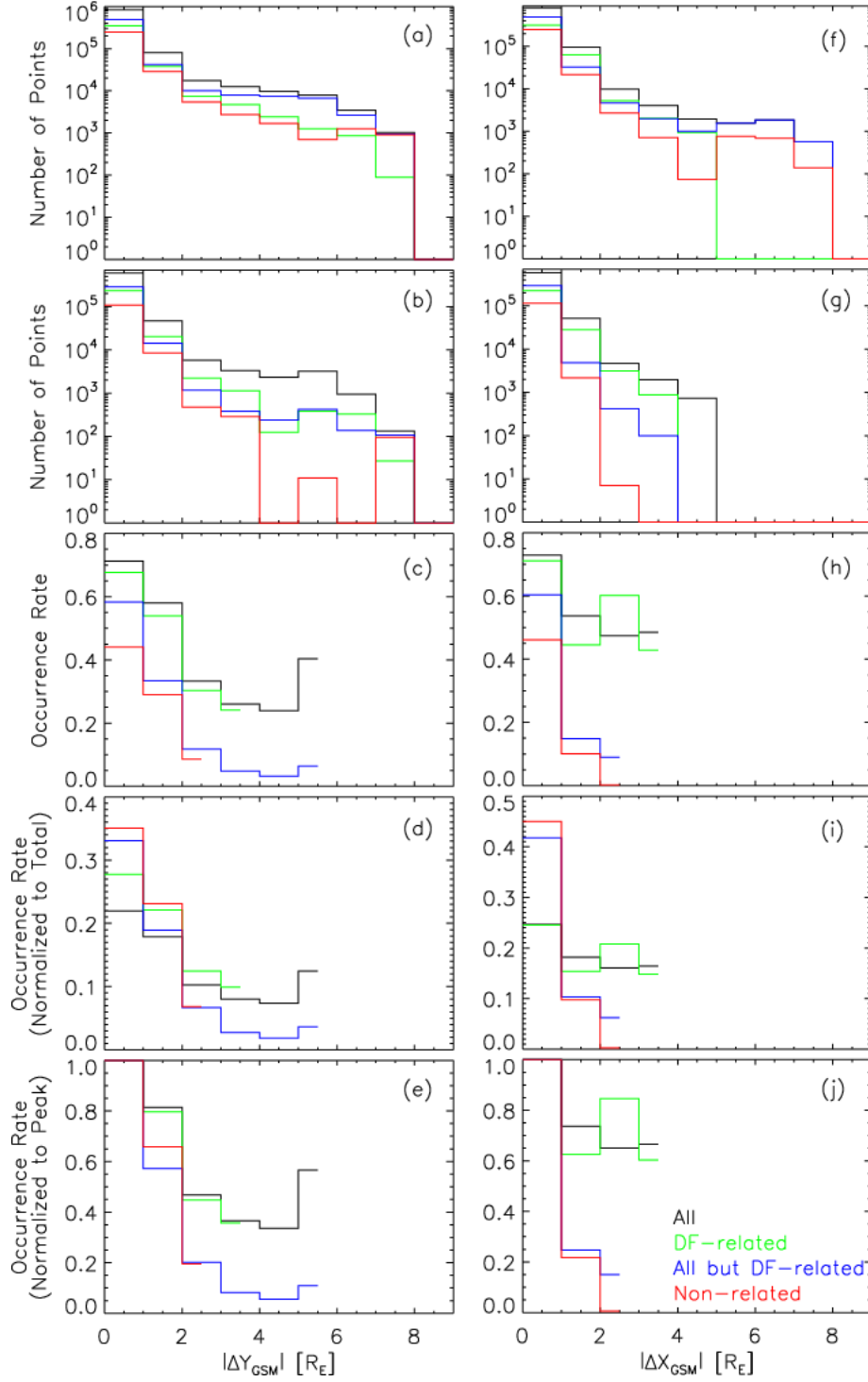


**Figure 4.5:** (a) and (f) show histograms of spacecraft separations in the Y- and X- directions ( $\Delta Y_{\text{GSM}} = Y_{\text{GSM,ref}} - Y_{\text{GSM,other}}$  and  $\Delta X_{\text{GSM}} = X_{\text{GSM,ref}} - X_{\text{GSM,other}}$ , respectively) between the

spacecraft that observes ECH waves (the reference spacecraft) and the other spacecraft, which has valid measurements, but may or may not observe the waves. (b) and (g) show histograms of  $\Delta Y$  and  $\Delta X$  separations only for cases when the other spacecraft also captures the waves at the same time as the reference spacecraft. (c) and (h) show the occurrence rates of ECH waves as function of  $\Delta Y$  and  $\Delta X$  separations (the ratios of the values in (b) and (g) over those in (a) and (f)). (d) and (i) show the distribution of normalized occurrence rates, the same occurrence rates as in (c) and (h), except normalized such that the integral under each curve is unity. (e) and (j) show the distribution of normalized occurrence rates to the peak values within each category. These two normalizations allow us to see the relative distribution of wave occurrence within each category. The four traces in each plot represent the result for the entire wave database (black), the DF-related waves (green), waves not correlated with DFs (blue), and waves not correlated with DFs or injections (red). Note that when the number of observations in the initial database within each category was fewer than 4000, the occurrence rates are not shown, to increase the statistical significance of the results and avoid noise.

#### **4.4 Modeling ECH Wave Extent under Different Magnetic Field Topologies**

To better understand the results obtained above, we model the equatorial confinement of ECH waves under different magnetic field topologies. We use the HOTRAY ray-tracing code [Horne, 1989] to follow a group of rays launched with certain properties and estimate the  $Z$ -spread of each ray under a certain magnetic field topology.

We adopt a “modified” Harris sheet magnetic field topology by adding a uniform  $B_z$  component ( $B_{z0}$ ) to the classic Harris sheet model:

$$\begin{aligned}
B_x &= B_{xlobe} \cdot \tanh\left(\frac{Z}{L}\right) \\
B_z &= B_{z0}
\end{aligned}
\tag{4.1}$$

where  $B_{xlobe}$  is the  $B_x$  component in the lobe;  $L$  is the half thickness of the current sheet; and  $Z$  is the distance to the neutral sheet. By varying  $B_{xlobe}$  and  $L$ , which control the magnetic field curvature, we can model the wave propagation under different magnetic field topologies. We keep the magnetic field magnitude the same by normalizing electron gyrofrequency to a constant value of 365 Hz (consistent with that estimated from the data at mid-tail).

We employ an electron distribution with a partially filled loss cone that is consistent with the marginal instability state [Zhang *et al.*, 2013], represented by the sum of subtracted bi-Maxwellians [e.g., Ashour-Abdalla and Kennel, 1978; Horne *et al.*, 2003]:

$$f = \sum_i f_i,$$

where each component is expressed by:

$$\begin{aligned}
f_i(v_{\parallel}, v_{\perp}) &= \frac{n_i}{\pi^{2/3} \alpha_{\perp i}^2 \alpha_{\parallel i}} \exp\left(-\frac{v_{\parallel}^2}{\alpha_{\parallel i}^2}\right) \\
&\cdot \left[ \Delta_i \exp\left(-\frac{v_{\perp}^2}{\alpha_{\perp i}^2}\right) + \frac{(1-\Delta_i)}{(1-\beta_i)} \cdot \left( \exp\left(-\frac{v_{\perp}^2}{\alpha_{\perp i}^2}\right) - \exp\left(-\frac{v_{\perp}^2}{\beta_i \alpha_{\perp i}^2}\right) \right) \right].
\end{aligned}
\tag{4.2}$$

Here  $n_i$  is the electron density,  $\alpha_{\perp i}$  and  $\alpha_{\parallel i}$  are the thermal velocities perpendicular and parallel to the ambient magnetic field, and  $\beta_i$  and  $\Delta_i$  essentially determine the depth and width of the loss cone, respectively. All the parameters are listed in Table 4.1, where the values of  $\beta_i$  and  $\Delta_i$

provide a loss cone of  $\sim 1^\circ$ , consistent with that calculated from the magnetic field data at mid-tail. In tracing rays under different magnetic field topologies, we use the same electron distribution and assume it to be constant with latitude and unchanging through the entire propagation region ( $< 1R_E$ ).

**Table 4.1:** Parameters of electron components used in the HOTRAY ray-tracing code.

Component	$N_e(m^{-3})$	$T_\perp(eV)$	$T_\parallel(eV)$	$\Delta$	$\beta$
1	$6.04 \times 10^4$	3.10	3.10	1.0	0.5
2	$3.02 \times 10^5$	338.6	214.5	0.255	0.163
3	$2.42 \times 10^5$	1836.2	1163.4	0.027	0.047

We first launch single ECH rays with the same wave frequency ( $1.2f_{ce}$ ), but with a range of initial wave normal angles (in the growth regime, from  $88.9^\circ$  to  $91.1^\circ$ ) and azimuthal angles (from  $0^\circ$  to  $350^\circ$ ) at the equator. We then record the maximum Z-extent of these rays for a given magnetic field topology as represented by the radius of curvature and evaluate how representative that may be of the actual extent of the waves in the data. When they have propagated a short distance away from the neutral sheet, ECH waves typically refract because field line bending modifies the wave normal angle and thus the group velocity. Under different magnetic field configurations, these waves will refract at different latitudes, as indicated by the

stars (linearly fitted by the green line) in Figure 4.8. The Z-extent of the rays is linearly correlated with the field line radius of curvature ( $R_c$ ), and the  $R_c$  to Z-extent ratio is 16:1.

A radius of curvature of  $\sim 0.8 R_E$ , consistent with that expected from the data at mid-tail after the passage of a DF [S.-S. Li *et al.*, 2011], suggests that the waves should be confined within  $\sim 0.05 R_E$  of the neutral sheet, which implies that simultaneous observations of ECH waves between two spacecraft would have been scarce, given the large typical spacecraft separation along Z in our database (median separation is  $0.3 R_E$ ; only  $<7\%$  of the data would have resulted in dual observations; yet our measured occurrence rate is 44%). This discrepancy is likely due to our oversimplified modeling of the ECH wave extent using single rays. In reality, the waves at a given location are the result of noise amplification emitted from a large range of source locations.

To study wave amplification quantitatively in a more realistic scenario, we also model the distribution of ECH wave intensity as a function of distance to the neutral sheet by integrating at each observation point the wave power contribution from rays emanating from many different sources distributed uniformly in space. We adopt a similar methodology to previous work of modeling plasmaspheric hiss distribution from a given chorus source [Bortnik *et al.*, 2011a, 2011b; Chen *et al.*, 2012]. Specifically, we assume the sources are distributed everywhere in the magnetotail, spaced at intervals of  $0.1 R_E$  in X,  $0.1 R_E$  in Y, and  $0.1 R_E$  in Z. At each location, we launch rays with a fixed wave frequency ( $1.2f_{ce}$ ), but with a  $0^\circ$  to  $180^\circ$  range of wave normal angles evenly distributed on the surface of the sphere. At each location and for each wave normal angle, we launch a set of azimuthal angles, from  $0^\circ$  to  $350^\circ$ , spaced at intervals of  $10^\circ$ . We launch  $N=1562 \times 36$  rays with various wave normal angles and azimuthal angles. As illustrated by five example sources labeled S0, S1, S2, S3, and S4 in Figure 4.6a, we propagate the rays away from

the source. We then compute the power along the rays. Collecting the power from all rays passing through a certain observation volume, with a half width of  $0.05 R_E$  in X,  $0.05 R_E$  in Y, and  $0.01 R_E$  in Z, we assign the total power at the observation point to the center of that volume. For each ray at a given observation volume, the local intensity of the ray (normalized to its source intensity) is given by  $\frac{P_i}{P_0} = \frac{10^{G/10}}{N}$ , where  $G$  is the path-integrated gain from the launch location to the observation spot,  $N$  is the total number of rays launched at each origin,  $P_i$  and  $P_0$  are the wave intensities at the observing and source locations. By repeating this for different observation locations systematically, we can build up the distribution of wave power everywhere in our one-dimensional model magnetotail.

Since free energy sources are assumed ubiquitous in our system and since we adopt a field configuration that is uniform in the X and Y directions, wave growth continues indefinitely as the ray propagates away from its origin. Figure 4.7 shows the distribution of the power ratio at different distances away from an equatorial source. We restrict the range of wave propagation to  $\pm 1.0 R_E$  away from its source in both X and Y. We expect that magnetic field fluctuations violate the uniformity assumption and restrict further wave propagation beyond that distance by wave refraction and damping. Thus rays from sources more than  $\pm 1.0 R_E$  away from an observation site are not allowed to contribute to wave power at that site.

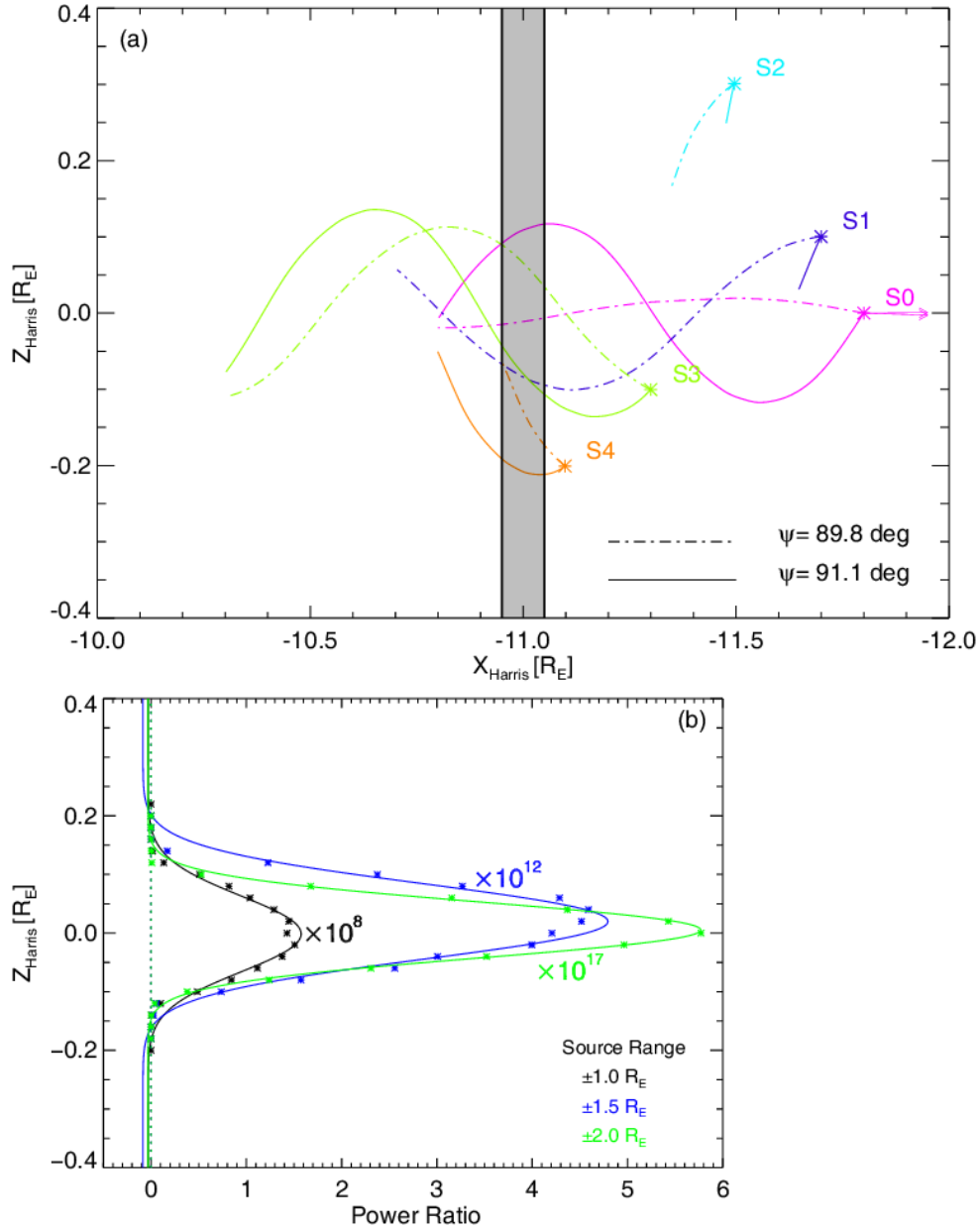


**Figure 4.6:** Schematic depicting our distributed, multi-source modeling approach for ECH wave intensity reconstruction using ray-tracing with the HOTRAY code. (a) XZ projection of rays in our model. Sources are spaced at intervals of  $0.1 R_E$  in X, Y, and Z. Only five sources are shown to exemplify the distributed sources. At each source, we launch multiple rays with a range of wave normal angles (rays that are able to propagate away from the origin have a limited range of

wave normal angles from  $88.9^\circ$  to  $91.1^\circ$ ) and different azimuthal angles (that affect the propagation direction in Y, but is not shown here). Two magenta arrows at source  $S_0$  denote wave vector directions of the two exemplified rays. Wave growth due to loss-cone instability and wave damping due to refraction of wave normal angles into a damped range controls the ray intensity as a function of the original intensity (which is assumed to start at noise level). The rays are collected and summed at each observer point (exemplified by the shaded region). The summed wave power (relative to the source power) as a function of observer position is shown in panel (b) for positions that vary in Z. The relative wave power is illustrated by the stars and exponentially fitted by the line. The colored curves represent results (each divided by the order of magnitude at the curve's peak) from different source range assumptions. Rays do not propagate farther than  $0.2 R_E$  due to curvature. The vertical dotted line represents our selection of a threshold for the wave power ratio ( $10^{-4}$  of the peak wave power) on which to base our estimate of the Z-extent of the wave.

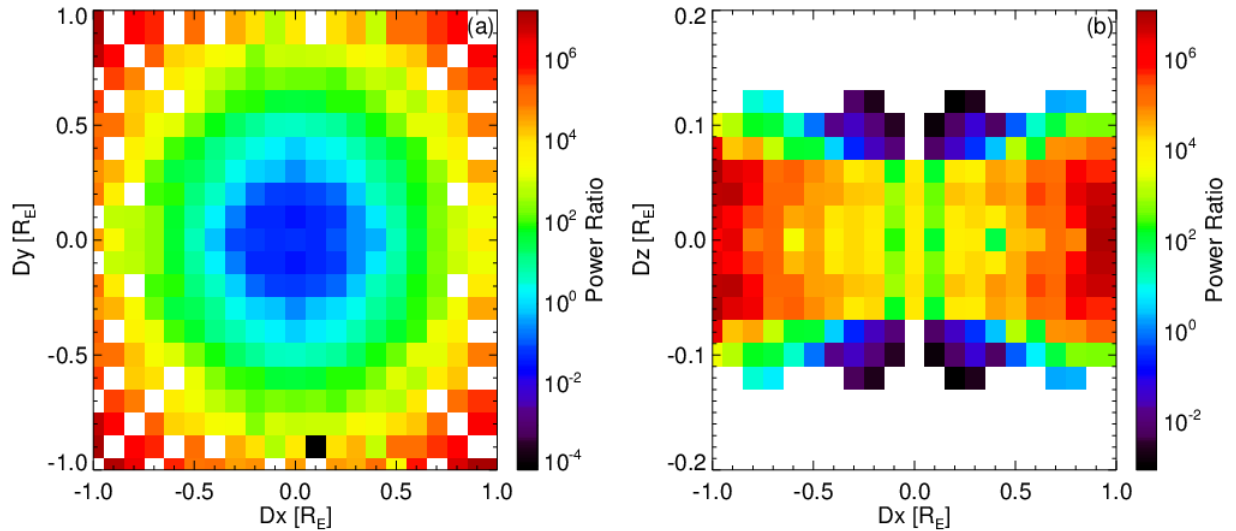


**Figure 4.7:** Distribution of wave power ratio in our model as a function of distance from the source (this one launched at  $Z=0$ ) location. The model is a Harris sheet magnetic field, modified

by the addition of a finite  $B_z$  ( $B_{z0}$ ) that establishes a field line curvature measured at the equator (for the case shown,  $B_{z0}=13$  nT,  $L=1.5 R_E$ ,  $B_{xlobe}=30$  nT, which results in  $R_c=0.8 R_E$ ).

Under our X/Y-uniform field topology assumption, all sources radiate identically regardless of their X/Y location, so we need only examine the wave power ratio distribution from sources located at different distances from the equator. So we construct forward-tracing source models for rays launched at different distances from the equator and this suffices for determining source behavior everywhere in the volume of interest. By back-tracing ECH waves to different sources and summing up power ratios at each observation site, we obtain the wave power at observation sites with different  $Z$  but the same  $X$  and  $Y$  locations. The wave power profile is illustrated by the stars (exponentially fitted by the line) in Figure 4.6b for a certain field topology ( $R_c=0.8 R_E$ ). By looking at the  $Z$ -distance at which the power ratio decreases to  $10^{-4}$  of its equatorial maximum, we estimate the extent of the waves in this multi-source model to be  $0.18 R_E$ . We also estimate the  $Z$ -extent by restricting the range of wave propagation to  $\pm 1.5 R_E$  and  $\pm 2.0 R_E$  away from its source in both  $X$  and  $Y$ , as shown in Figure 4.6b. The resulting  $Z$ -extents are  $0.16 R_E$  and  $0.15 R_E$ , respectively. The  $Z$ -extent of the emission is roughly the same, regardless of the allowable range of the sources. Although the absolute amplification of the waves depends on the amplitude and wavelength of low-frequency plasma sheet fluctuations that may limit the region of ray propagation, the  $Z$ -extent is expected to be independent of our source range assumptions because it is defined relative to peak amplification at the equator.

In the interest of saving running time, we only estimate the  $Z$ -extent of ECH waves under three different  $R_c$ s ( $0.8$ ,  $1.5$  and  $3.7 R_E$ ); results are shown in Figure 4.8. The linear correlation between field line curvature and  $Z$ -extent, already established in the single ray-tracing result, is

also evident in the multi-source model results. The linear fit to the multi-source model (red line) corresponds to a larger wave extent for a given magnetic field curvature radius, compared to single ray runs. The  $R_c$ -to-wave- $Z$ -extent ratio is now 8:1. The reason for this is the presence of sources at non-equatorial locations which attain sufficient amplification; this is a more realistic scenario than single-ray estimates of the wave  $Z$ -extent. The observed  $Z$ -extent of  $\sim 0.2 R_E$  (for both the entire database and DF-related subset) corresponds to an  $R_c$  of  $\sim 0.9 R_E$ , which is a reasonable field line curvature for a wide range of plasma sheet conditions and distances from Earth. For quiet-time events, a smaller  $Z$ -extent ( $\sim 0.1 R_E$ ) corresponds to an  $R_c$  of  $\sim 0.1 R_E$ .

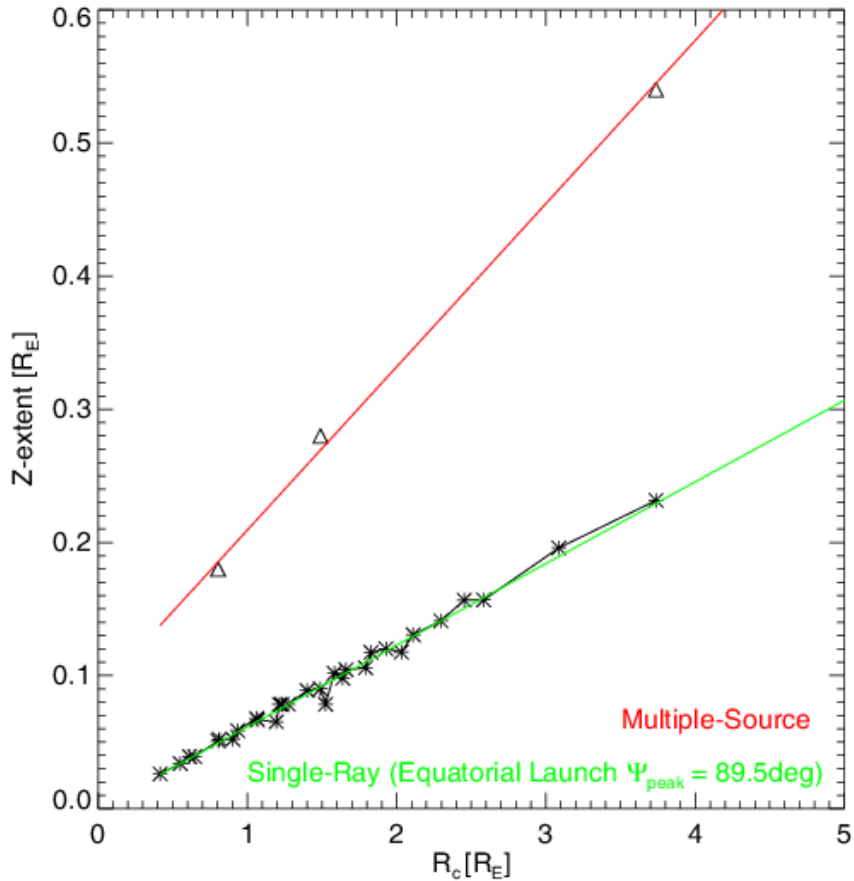


**Figure 4.8:** Maximum  $Z$ -extent of ECH waves from single-ray tracing (stars, linearly fitted by the green line) and multiple-source modeling (triangles, linearly fitted by the red line).

## 4.5 Summary

We used five tail seasons of THEMIS observations to survey the spatial distribution of ECH emissions. As shown in Figure 4.1c, within  $10 R_E$  this distribution is almost symmetric across the midnight meridian; beyond  $10 R_E$ , ECH emissions occur preferentially in the pre-midnight region, which is correlated with higher geomagnetic activities. Within  $10 R_E$ , the non-related (both non-DF and non-injection) ECH emissions show a clear preference for the dawn sector.

By correlating wave intensity between different THEMIS spacecraft, we estimated the extent of ECH waves in three directions. As consistently shown in Figures 4.2 and 4.3, the spacecraft closer to the neutral sheet tends to observe ECH waves more often than one located farther away from the neutral sheet ( $\Delta\beta/\beta$  and  $\Delta Z/L$  are used as proxies of the spacecraft separation relative to the neutral sheet). As shown in Figures 4.2c and 4.2d, the maximum scale of ECH waves in  $Z$  is  $\sim 0.5$  in terms of normalized DNS and  $\sim 0.5 R_E$  in absolute distance. We also compared the occurrence rate of dual-spacecraft observations as a function of  $|\Delta Z|/L$  during different local plasma sheet activity conditions. With reduced local plasma sheet activity, ECH waves tend to be more confined to the equator (Figures 4.4b and 4.4c).

Similarly, we examined the extent of ECH waves in the  $X$  and  $Y$  directions for different subsets. As shown in Figure 4.5c, the  $Y$ -scale of these waves is  $\sim 2 R_E$ . The normalized occurrence rate (Figures 4.5d and 4.5e) of non-DF and non-related ECH waves decreases more rapidly with  $|\Delta Y_{GSM}|$  than the occurrence rate in the entire database and in the DF-related subset. As shown in Figure 4.5h, the  $X$ -scale of the entire wave database and the DF-related subset is at least  $4 R_E$ , whereas it decreases to  $\sim 1 R_E$  for the non-DF and non-related categories (Figures 4.5h, 4.5i, and 4.5j).

By tracing single ECH rays in the HOTRAY code, we found that the  $Z$ -extent of these rays is linearly correlated with the field line radius of curvature ( $R_c$ ). We also modeled the distribution of ECH wave power as a function of distance to the neutral sheet by back-tracing the waves to distributed sources in space, confirming the linear correlation between field line curvature and  $Z$ -extent and providing a realistic estimate of the wave extent for a given  $R_c$ . The observed  $Z$ -extent of  $\sim 0.2 R_E$  corresponds to an  $R_c$  of  $\sim 0.9 R_E$ , which is a reasonable value.

## 4.6 Discussion and Conclusion

The nearly symmetric occurrence of ECH waves across the midnight meridian within  $10 R_E$  and the preference for the pre-midnight region beyond  $10 R_E$  are consistent with previous statistical results from *Ni et al.* [2011a] in the overlap region of 6 to  $15 R_E$ . After excluding ECH waves correlated with injections and DFs, which have been shown to peak in occurrence rate at pre-midnight [*Birn et al.*, 1997a; *Gabrielse et al.*, 2014; *Liu et al.*, 2013], we find that the non-related ECH emissions show a clear preference for the dawn sector (within  $10 R_E$ ). This may indicate that these waves are related to injected electrons that drift away from their original flow channels at pre-midnight.

Using simultaneous multi-probe observations, we established ECH waves' extent with finer scales than in single spacecraft occurrence rate studies. In examining the  $Z$ -extent of these waves, we found a higher probability of observing ECH waves closer to the neutral sheet, which is expected from their equatorial confinement. Our results on the extent of the waves are expected to be used in future modeling of ECH wave interactions with plasma sheet electrons, which will enable better modeling of the precipitated electron energy flux for comparison with ground-

based or ionospheric precipitation measurements. This, in turn, is expected to enable better evaluation of the contribution of ECH to diffuse aurora relative to other wave modes.

Our finding that the  $Z$ -extent of ECH waves is proportional to the magnetic field curvature radius ( $R_c$ ) agrees with the hypothesis on the mechanism underlying the correlation between ECH waves and DFs reported in Chapter 3: when the magnetic field configuration becomes more dipolarized upon arrival of dipolarizing flux bundles (the strong magnetic field region preceded by dipolarization fronts) [Liu *et al.*, 2013], high-amplitude ECH waves will propagate to a greater latitudinal range around the neutral sheet, as indicated by Figure 4.8. The  $Z$ -extent of ECH waves from dual-spacecraft observations,  $\sim 0.2 R_E$ , corresponds to  $R_c \sim 0.9 R_E$  from our modeling, indicating that the observed extent of these waves is consistent with a dipolarized field topology [S.-S. Li *et al.*, 2011]. In addition, the strict confinement of ECH waves in  $Y$  ( $\leq 2 R_E$ ) and their loose confinement in  $X$  ( $\geq 4 R_E$ ) are consistent with the volume of a dipolarized flux tube after DFs pile up and dipolarization extends downtail [Angelopoulos *et al.*, 1996]. This type of dipolarized flux region after DFs, may be required to excite these waves to higher amplitudes over a sufficiently large extent in  $Z$  for them to be more easily observable in the aftermath of dipolarization fronts and injections, i.e., at active times.

By excluding ECH emissions correlated with injections and DFs, we also examined the extent of these waves during quiet plasma sheet conditions. Waves not related to injections and DFs (more stretched magnetic field topology) demonstrate a smaller  $Z$ -extent ( $|\Delta Z|/L \sim 0.1$ ) than those in the entire wave database, as shown in Figure 4.4. This agrees with our expectation that the curvature radius in a plasma sheet devoid of local dipolarizations would be smaller, leading to a smaller  $Z$ -extent of the waves. As shown in Figure 4.5, non-related ECH waves have a

similar Y-extent ( $\sim 2 R_E$ ), but a smaller X-extent ( $\sim 1 R_E$ ) than those in the entire database (behavior dominated by DF-related waves). This further indicates that in addition to modifying the Z-extent of ECH waves by increasing the magnetic field curvature radius, dipolarizing flux bundles and related injections may also increase the wave X-extent by modifying the local magnetic topology and plasma environment; these modifications and their effects on wave generation are left for future investigation.

In modeling the wave power distribution, we restrict the range of wave propagation to  $\pm 1.0 R_E$  away from its source in both X and Y. Although this is an arbitrary cut, the Z-extent from modeling remains roughly the same when we vary this source range assumption. In addition, our model depicts a qualitative picture of why field-line curvature ( $R_c$ ) is critical to controlling amplifications (and thus observations) of ECH waves. Verifications of our result will be pursued in a future study using a realistically-varying magnetotail field topology.

Excited by the loss-cone instability of the hot plasma sheet electrons, ECH waves can, in turn, scatter resonant electrons into the loss cone. There should be a quasi-steady state in which electron diffusion balances wave growth. Because of the smaller loss cones at higher L-shells, ECH wave amplitude during such a quasi-steady state in the outer magnetotail may drop below current instrument detection level during quiet conditions [Zhang *et al.*, 2013]. Although possibly not detectable, these low-amplitude ECH waves could still contribute to drizzle precipitation of diffuse aurora during quiet times. On the other hand, ECH waves can be intensified by local plasma sheet activations, such as electron injections and DFBs, which create plasma sheet conditions favorable for wave growth in their aftermath [Meredith *et al.*, 2000; Zhang and Angelopoulos, 2014]. This study shows that the Z-extent of ECH waves is dictated by

the magnetic field line curvature, indicating that a dipolarized flux region (following DFs or at the adjacent, thin quiet plasma sheet) may be required to excite these waves to such a larger amplitude wave with observable extent in Z. Electron injections, often associated with DFBs, are also capable of promoting wave growth, not only locally within their injection channels, but also along the dawnward-drifting paths of injected electrons (localized to within  $4 R_E$  in Y). Intensified wave emissions following plasma sheet activity may dominate the wave observations in the middle to outer magnetotail ( $X < -10 R_E$ ), contributing to enhanced diffuse auroral precipitation in higher magnetic latitudes during such active times.

## CHAPTER 5

### **Evaluation of ECH Wave Contribution to Diffuse Aurora**

Based on our ECH wave database and the improved understanding of the wave excitation, in this chapter, we aim to quantitatively evaluate the ECH wave-induced plasma sheet electron precipitation systematically throughout the entire magnetotail out to  $35 R_E$  (the THEMIS apogee), and compare it directly with the equatorially mapped energy flux distribution of diffuse aurora from ionospheric observations. Our study is expected to definitively resolve the long-standing question regarding the role of ECH waves in driving the diffuse aurora. Although the wave amplitudes are expected to drop with distance from the Earth, due to the small loss cone size and stretched magnetic field topology, ECH waves are still capable of causing efficient scattering of plasma sheet electrons to account for the observed diffuse aurora dissipation. Our results clearly demonstrate that ECH waves are the dominant driver of diffuse aurora in the middle to outer magnetotail.

An introduction of previous studies on evaluating ECH waves' role to diffuse aurora is presented in Section 5.1. We model the diffuse aurora precipitation and map it to the equator in Section 5.2. Section 5.3 presents modeling of the diffusion of plasma sheet electrons due to interactions with ECH waves. Estimates of the resultant precipitation energy flux throughout the magnetotail are shown in Section 5.4. We summarize and discuss the results in Section 5.5.

## 5.1 Introduction

Diffuse electron precipitations constitute the majority of particle energy deposition into high latitude ionosphere, alters the profiles of ionospheric conductivity, and in turn influences the global pattern of magnetospheric convection, which are all affiliated with ionosphere-magnetosphere coupling processes [Khazanov *et al.*, 2014]. It is generally accepted that the source population for the diffuse aurora (refers to diffuse electron precipitation hereafter in this study) originates from plasma sheet electrons in the hundreds to several thousand eV energy range, whose precipitation is attributed to resonant wave-particle interactions [Fontaine and Blanc, 1983]. As discussed in Section 1.5.3, the mechanism of the diffuse auroral precipitation at higher L-shells still remains unclear. Recent theoretical modeling studies have suggested that ECH emissions may be the potential driver of diffuse aurora outside the inner magnetosphere [Ni *et al.*, 2012a; Zhang *et al.*, 2013].

The impact of ECH waves on the plasma sheet electron dynamics and the diffuse auroral precipitation has not been investigated systematically and globally, however. This requires quantification of quasi-linear bounce-averaged scattering rates and loss timescales of electrons based on a realistic magnetic field topology, wave characteristics, and simultaneous electron distributions. The extensive THEMIS wave and particle databases enable us to develop an improved global model of ECH waves, loss cone size, and the accompanying electron distributions. By modeling the electron diffusion due to interactions with ECH waves, we can estimate the loss cone fill ratio of the local electron distribution and the resultant precipitating energy flux at different regions of the magnetotail. The contribution of ECH waves to the diffuse

auroral precipitation can then be directly investigated by comparing to the overall diffuse auroral precipitation in each location.

## 5.2 Modeling Diffuse Aurora Precipitation

We first model the global pattern of diffuse aurora precipitation in the ionosphere using the OVATION Prime model. This model is based on 22 years (1984-2005) of energetic particle measurements from the Defense Meteorological Satellite Program (DMSP) from which an empirical relationship between the solar wind conditions and the aurora location and intensity was developed [Newell *et al.*, 2010]. Using this model, Newell *et al.* [2009, 2010] have shown that the pattern of diffuse aurora precipitation varies with solar wind driving conditions and that the hemispheric power (globally integrated total particle energy deposition) undergoes small seasonal variations.

As shown in Figure 5.1, the hemispheric power of diffuse aurora increases from 5.5 GW to 15.5 GW from low to high solar wind driving conditions. The definition of low and high solar wind driving conditions is the same as used by Newell *et al.* [2009, 2010]. We then map the diffuse aurora precipitation to the magnetic equator, using both T89 ( $K_p = 2$ ) and T96 (solar wind dynamic pressure  $P_{\text{dyn}} = 1.5$  nPa;  $Dst = -5$  nT;  $B_y = 0.5$  nT;  $B_z = -1.0$  nT) magnetic field models [Tsyganenko, 1989; Tsyganenko and Stern, 1996]. Note that the winter/summer ratio of diffuse aurora energy fluxes is close to 1.0; it can be at most  $\sim 1.3$ , during high solar wind driving conditions [Newell *et al.*, 2010], so we use the energy flux precipitation during local summer conditions to represent the global pattern of diffuse aurora in these plots, as representative.

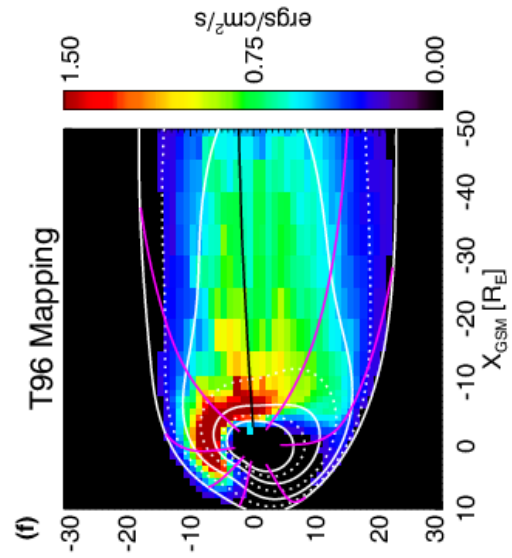
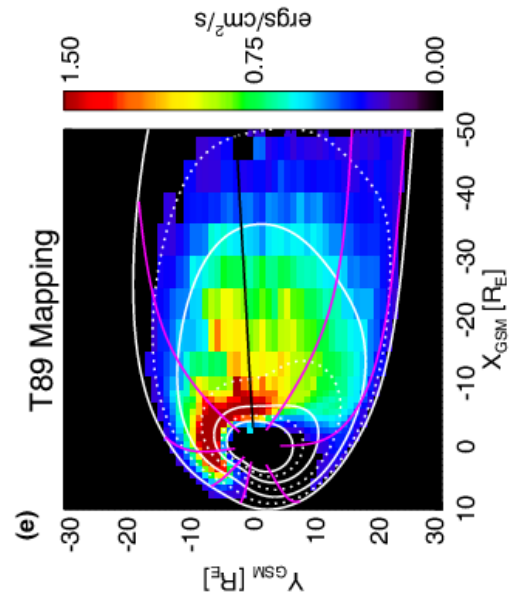
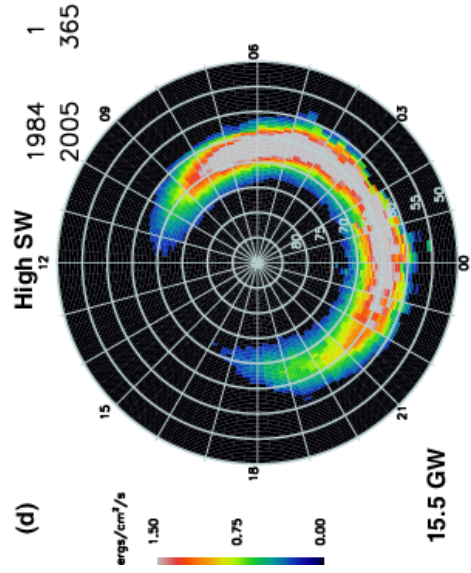
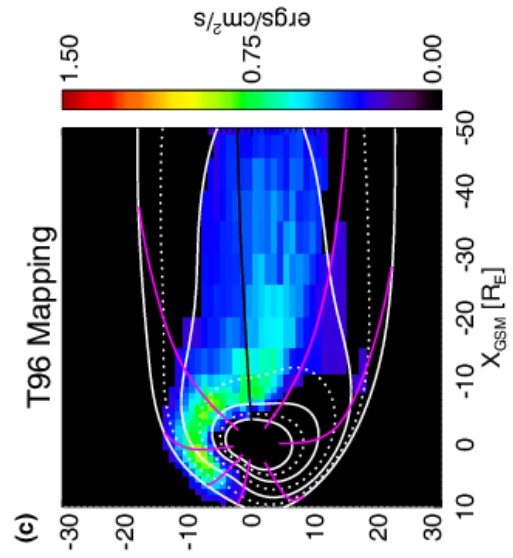
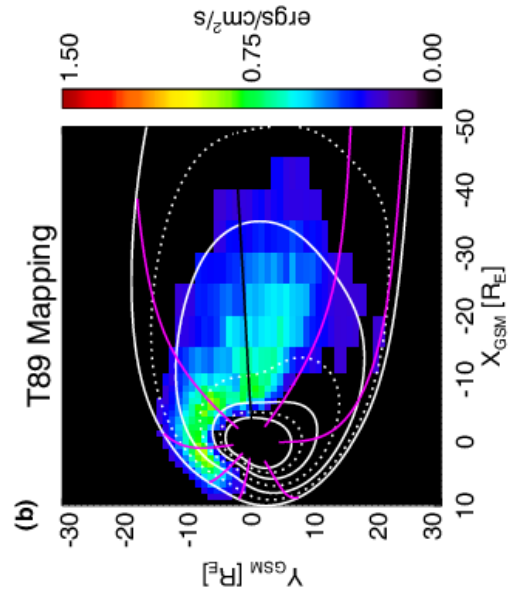
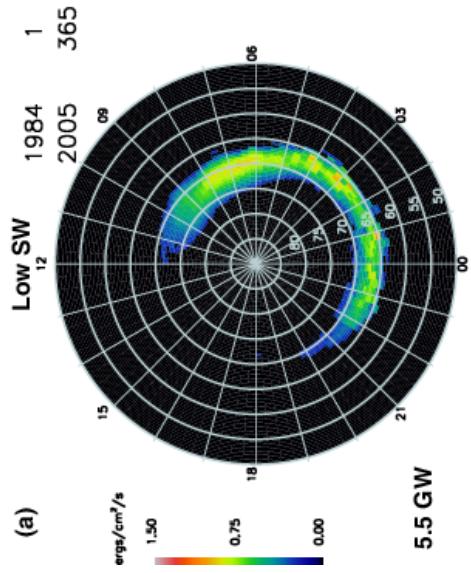


**Figure 5.1:** Electron diffuse aurora energy flux for (a) low and (b) high solar wind driving as a function of magnetic latitude (MLAT) and magnetic local time (MLT), obtained from OVATION Prime model. Only bins with energy fluxes greater than  $0.25 \text{ ergs/cm}^2/\text{s}$  are shown here and included in the subsequent analysis in order to eliminate low amplitude noises. (b) and (c) show the distributions of energy flux during low solar wind driving mapped to the equatorial plane using T89 and T96 magnetic model, respectively. (e) and (f) show the distributions of energy flux during high solar wind driving mapped to the equatorial plane using T89 and T96 magnetic model, respectively. In Panels (b), (c), (e), and (f), magenta lines represent the MLT contours in the ionosphere every 3 hours, with midnight marked by the overlaid black line; white solid circles denote the MLAT contours in the ionosphere at  $60^\circ$ ,  $65^\circ$ ,  $70^\circ$ , and  $75^\circ$ , while white dotted circles represent the MLAT contours in the ionosphere at  $62.5^\circ$ ,  $67.5^\circ$ , and  $72.5^\circ$ .

It is clear that the diffuse aurora precipitation is most intense at pre-midnight to dawn MLT sectors, following the drift path of plasma sheet electrons. Under low solar wind driving conditions, the total power due to electron precipitation on the ionosphere from the middle to outer magnetotail (defined as anti-sunward of the terminator and having equatorial radial distance greater than  $8 R_E$ ) is 1.36 GW for T89 (1.40 GW for T96). This corresponds to 64% of the total nightside precipitation (nightside was defined as negative X locations in the equator) in T89 (66% for T96). Although precipitation in the magnetotail increases during high solar wind driving conditions, the ratio decreases to 37% for T89 mapping results and 38% for T96 results.

### **5.3 Modeling ECH Wave Scattering of Plasma Sheet Electrons**

In order to model diffusion due to wave particle interactions between ECH waves and plasma sheet electrons throughout the magnetotail, we need to first determine the distribution of wave power, magnetic field magnitude and curvature (relevant for loss cone size and ray propagation) and plasma parameters (density, temperature, anisotropy relevant to local wave growth), which will be necessary for quantifying the scattering rates. Using the estimated diffusion coefficients of ECH waves at various equatorial locations, we then model the diffusion using quasi-linear theory, from which we infer the loss cone fill ratio of electron distributions at the steady-state. We shall use those to estimate the contribution of ECH waves to precipitation loss as a function of location as well as globally and compare the results with OVATION estimates of that quantity in Sections 5.4 and 5.5.

#### **5.3.1 Spatial Distribution of ECH Waves**

We use the same ECH wave database as we developed in Section 4.2, which includes ECH emissions (represented by individual data samples within ECH events with peak wave amplitudes  $> 0.1\text{mV/m}$ ) in the plasma sheet (with plasma beta  $> 0.5$ ) captured by five THEMIS spacecraft during five tail science phases (in 2008-2012). As shown in Figure 4.1, the spatial distribution of the ECH occurrence rate in the XY plane (in aberrated GSM coordinates with a  $4^\circ$  aberration angle) has a slight downward preference within  $10 R_E$ ; outside of that distance, it is preferentially seen in the pre-midnight sector. This resembles the pattern of diffuse aurora shown in Figure 5.1. The low occurrence rates beyond  $15 R_E$  ( $< 10\%$ ) result from a combination of low sample rate due to THEMIS orbits (there have only been 2 years of traversals of that region by

two THEMIS probes) and the small wave amplitudes expected at these distances, as demonstrated in Chapter 2.

Plasma and magnetic field characteristics related to ECH waves are important for modeling the wave excitation, propagation and interaction with electrons. The distribution of wave power, and relevant electron and magnetic field parameters during ECH emission intervals is shown in Figure 5.2. Wave amplitude is the critical parameter in estimating the diffusion coefficients; it is a proxy for wave power and since it is recorded as the mean of the absolute value of the bandpass-filtered signal in the FBK data product, we multiply the raw FBK electric field value by a factor  $\pi/2$  to convert it into the nominal wave amplitude. We determine the peak wave amplitude during each ECH event. We then take the average values of all events within each spatial bin to construct the distribution of wave amplitudes through the equatorial magnetotail. In order to remove the data scattering due to limited data points beyond  $\sim 20 R_E$ , we further smooth the distribution by averaging over 9 adjacent bins (3x3 bins in 2 dimensions, X and Y, weighted by the number of events within each bin) centered at the original bin. The total magnetic field magnitude ( $B_t$ ) quantity is important as it will be used to infer the local electron gyrofrequency and loss cone size. The field-aligned electron energy fluxes ( $J_{\parallel}$ ) are important as they are representative of the electron distribution just outside the loss cone that is relevant for precipitation; they will be used for quantifying the electron precipitation once the loss cone fill ratio has been evaluated. We use the average  $B_t$  and  $J_{\parallel}$  (during ECH emission intervals) within each bin to construct the distribution of these parameters; similarly, we further smooth the distribution to eliminate data scattering due to limited data points, by averaging over 9 adjacent bins.

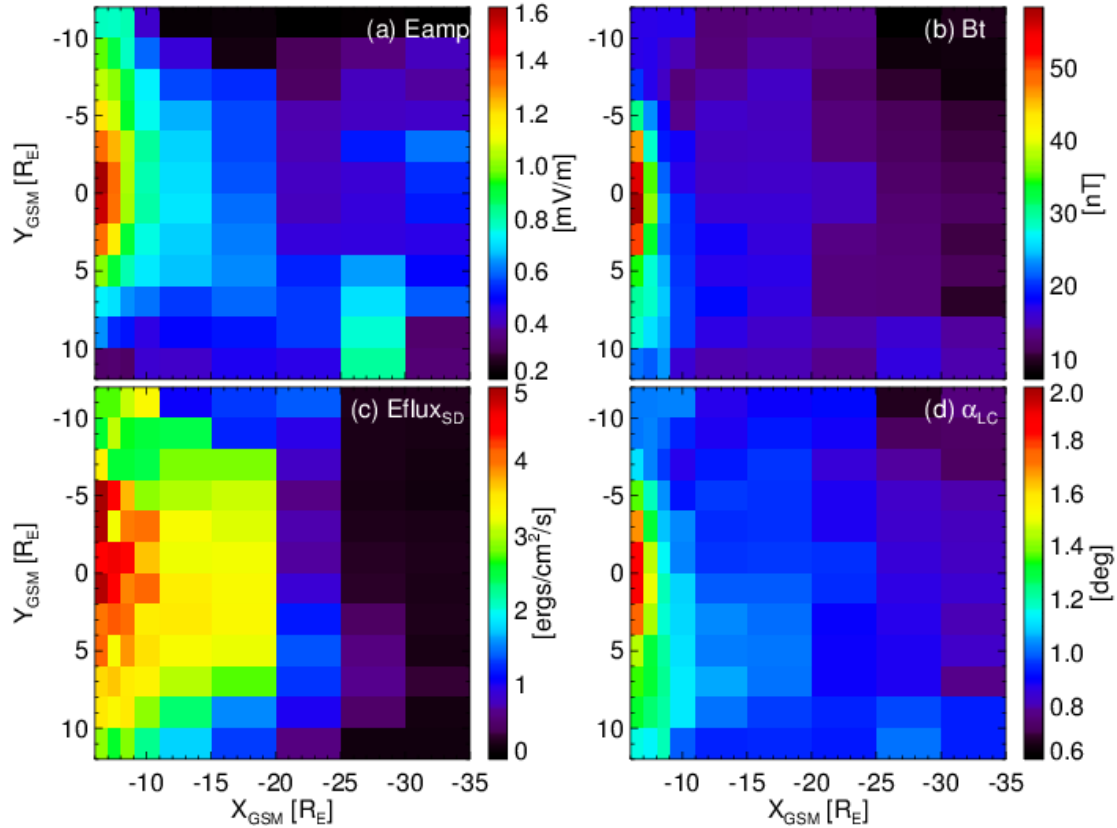


**Figure 5.2:** Distribution (during ECH events) of (a) average ECH wave amplitude, (b) median magnetic field magnitude, (c) energy flux during strong diffusion limit inferred from average magnetic field-aligned (pitch-angle range  $0^\circ$ - $22.5^\circ$ ) electron energy flux,  $J_{//}$ , within the energy range of 50eV to 25keV (energy range of ESA instrument excluding photoelectrons) and (d) loss cone size inferred from the magnetic field magnitude in panel (b).

The average wave amplitude decreases with increasing distance down the tail; it is more intense in the pre-midnight sector beyond  $15 R_E$ , while the amplitude becomes larger in the dawn sector within  $10 R_E$  (Figure 5.2a). The magnetic field magnitude shows a slight asymmetry across the midnight meridian (Figures 5.2b), with larger values at the dusk side, leading to a similar asymmetry for the distribution of loss cone size (Figures 5.2d). This is likely due to the

increased presence of DFBs and injections (known to preferentially occur in the pre-midnight sector) in our database of ECH emissions, since ECH waves are correlated with these active time phenomena. The DFBs, which bring new flux from the tail, are expected to enhance the total field preferentially in the pre-midnight sector. The total energy flux during strong diffusion limit also shows an asymmetry towards the dusk side (Figure 5.2c).

In parallel to our study of the ECH wave distribution, we also investigate the distribution of chorus emissions using the same filter bank (FBK) wave database of the THEMIS spacecraft crossing the plasma sheet. We use the criteria developed by *Li et al.* [2009b] to select chorus emissions between 0.1 and 0.8  $f_{ce}$ . We estimated  $f_{ce}$  from the local northward magnetic field component that approximates the equatorial magnetic field. Same as *Li et al.* [2009b], data with  $f_{ce}$  larger than 10 kHz or smaller than 800 Hz are excluded from the subsequent analysis in order to select measurements covering the entire chorus band. We present in Figure 5.3 the spatial distribution of the chorus wave occurrence rates in the XY plane (in aberrated GSM coordinates with a 4° aberration angle), using the same format as in Figure 4.1. Compared to the distribution of ECH waves in the overlap region, the occurrence rate of moderate (wave amplitudes >10pT) chorus emissions drops significantly (<1%) beyond 9  $R_E$ , indicating that chorus waves are statistically weak (a few pT) in the middle to outer magnetotail.

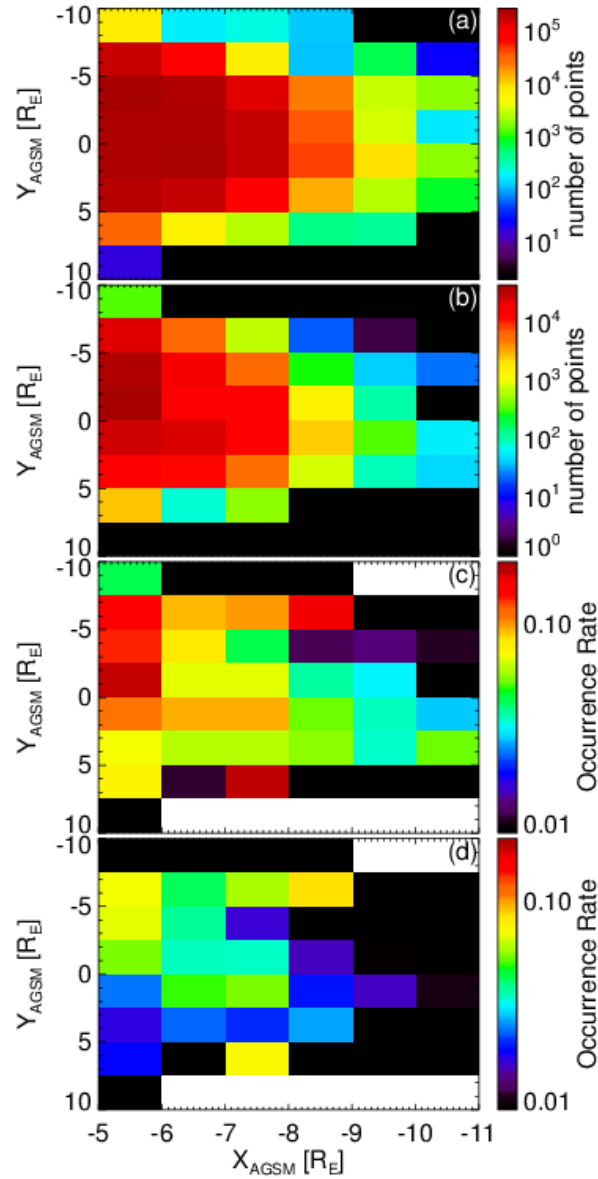


**Figure 5.3:** Distribution of (a) valid measurements (orbital distribution with valid SCM data) and (b) chorus observations from single spacecraft in the XY plane (in aberrated GSM coordinates). (c) Occurrence rate of chorus emissions computed as the ratio of (b) to (a). (d) Occurrence rate of chorus emissions with wave amplitudes  $>10$  pT.

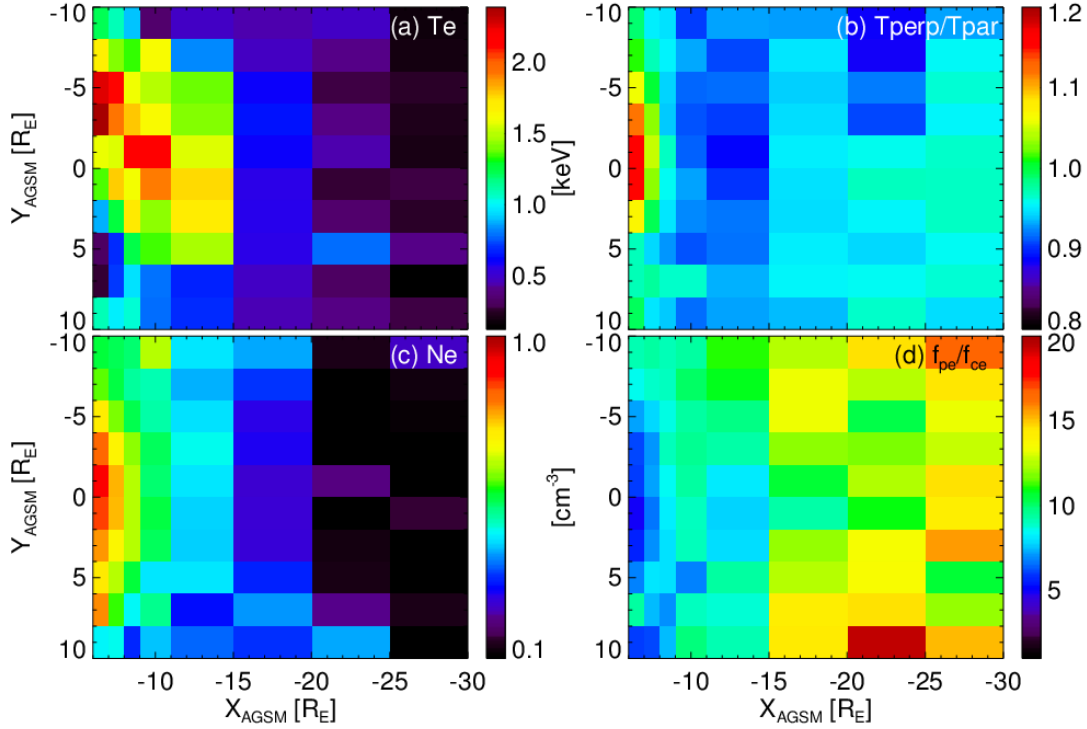


**Figure 5.4:** Distribution of (a) median electron temperature, (b) median temperature anisotropy ( $T_{\perp}/T_{\parallel}$ ), (c) median electron density (after removing points with unrealistically values  $>10\text{cm}^{-3}$ ), and (d) median value of the ratio of plasma frequency ( $f_{pe}$ ) to the local electron cyclotron frequency ( $f_{ce}$ ) in the XY plane (in aberrated GSM coordinates). Data are collected within the central plasma sheet (with plasma beta  $>0.5$ ).

Plasma density and temperature anisotropy are important in controlling chorus wave generation, which affect the resonant electron energy and the magnitude of growth rate. We thus examine the distribution of these two parameters in the central plasma sheet (characterized by plasma beta  $>0.5$ ), where chorus wave are mainly confined to. The total electron density is inferred from the spacecraft potential. Electron cyclotron frequencies ( $f_{ce}$ ) are estimated from in situ magnetic field data measured by the FGM instrument. Electron temperature anisotropy is denoted by the ratio of electron perpendicular and parallel (relative to the magnetic field)

temperature from ESA measurements, i.e.,  $T_{\perp}/T_{\parallel}$ . As shown in Figure 5.4, the plasma frequency to the electron cyclotron frequency ( $f_{pe}/f_{ce}$ ) is higher at larger distances mainly due to the weaker magnetic field magnitude. Within  $X \sim -8 R_E$ , the ratio  $f_{pe}/f_{ce}$  is smaller than  $\sim 5$ , which coincides with the preferred region of intense chorus waves (Figure 5.3d). In addition,  $T_{\perp}/T_{\parallel}$  is greater than 1 within  $X \sim -8 R_E$ , which may provide free energy for the excitation of the strong chorus emissions confined within the same region.

### 5.3.2 Quantifying Diffusion Coefficients

We compute the ECH wave scattering rates under T89 magnetic field topology, same as the model we used for mapping the diffuse aurora to the neutral sheet. Estimation of local diffusion rates requires latitudinal confinement of ECH waves and the latitudinal variations of wave normal angle, wave number and wave power, which are difficult to acquire directly from observations. We thus infer the equatorial wave number from the resonant condition and the local electron gyrofrequency by assuming a minimum resonant energy of 500 eV for a fixed wave frequency (we used a wave frequency  $f=1.5f_{ce}$  and a wave normal angle of  $89.5^{\circ}$  at the equator to represent the first harmonic). Since the observed ECH emissions are confined within a few degrees of the magnetic equator [e.g., Belmont *et al.*, 1983; Roeder and Koons, 1989; Meredith *et al.*, 2009; Ni *et al.*, 2011a], the maximum latitude ( $\lambda_{\max}$ ) over which ECH waves exist is assumed to be varying over the magnetotail as shown in Figure 5.5, from  $5.7^{\circ}$  in the closest ( $X=-6.5 R_E$ ;  $Y=1.0 R_E$ ) bin to  $0.7^{\circ}$  in the farthest ( $X=-32.5 R_E$ ;  $Y=11.0 R_E$ ) bin. Following Ni *et al.* [2011b, 2012a], we then linearly interpolate between the minimum magnetic field magnitude location and  $\lambda_{\max}$  to obtain the latitudinal variations of wave normal angle

(approaching  $90^\circ$  at  $\lambda_{\max}$ ), parallel wave number (assuming perpendicular wave number unchanged with latitudes), and width in parallel wave number.

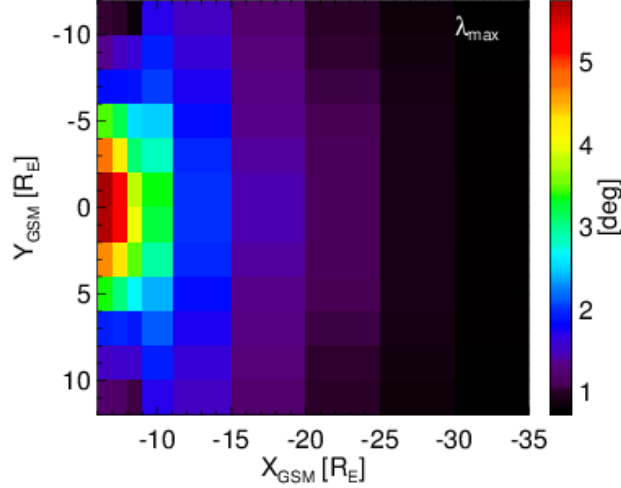


**Figure 5.5:** Distribution of latitudinal confinement of ECH waves in units of degrees.

Using the T89 magnetic field model, we then incorporate the aforementioned distributions of wave parameters and plasma properties into the diffusion rate formulas described in the appendix. We thus estimate the bounce-averaged scattering rates for all equatorial nightside plasma sheet locations. Figure 5.6 shows results for two limit cases near midnight: one closest to Earth ( $X=-6.5 R_E$ ,  $Y=-1.0 R_E$ ) and one furthest from Earth ( $X=-32.5 R_E$ ,  $Y=-1.0 R_E$ ). To investigate the efficacy of ECH waves in scattering plasma sheet electrons, we also compare the pitch angle scattering rates at the edge of the loss cone  $\langle D_{\alpha\alpha} \rangle|_{LC}$  with the strong diffusion rate  $D_{SD}$  defined by *Kennel* [1969] as:

$$D_{SD} = \frac{2(\alpha_{LC})^2}{\tau_B} \quad (5.1)$$

where  $\tau_B$  is the electron bounce period along the entire field line determined as [Ni *et al.*, 2012a, 2012b]:

$$\tau_B = \frac{2}{v} \int_{\lambda_{m,s}}^{\lambda_{m,n}} \sec \alpha \sqrt{r^2 + \left(\frac{\partial r}{\partial \lambda}\right)^2} d\lambda \quad (5.2)$$

with  $v$  denoting the electron thermal speed,  $\alpha$  for local pitch angle,  $r$  for radial distance from the Earth,  $\lambda$  for magnetic latitude, and  $\lambda_{m,s}$  and  $\lambda_{m,n}$  representing the mirror latitudes on the southern and northern hemisphere.

As shown in Figure 5.6, intense ECH wave scattering in the near-Earth plasma sheet occurs only for electrons with pitch angles  $<20^\circ$  and over a limited energy range (0.2-1 keV), consistent with numerical results by *Thorne et al.* [2010] and *Tao et al.* [2011]. Compared to pitch angle diffusion rates, momentum diffusion rates and mixed diffusion rates (not shown here) by ECH waves are small at both near Earth and distant tail plasma sheet, suggesting that ECH emissions play only a minor role in energizing plasma sheet electrons. It is also clear, however, that at larger distances ECH waves tend to efficiently scatter progressively larger pitch angle and lower energy ( $<200\text{eV}$ ) electrons. This is due to increased magnetic field line stretching with distance from Earth. Moreover, as seen in Figures 5.5c and 5.5f, the strong diffusion rate  $D_{SD}$  decreases by at least one order of magnitude from  $X=-6.5 R_E$  to  $X=-32.5 R_E$ , due to smaller loss cone size and the more stretched (and thus longer) field lines at larger distances. Therefore, the strong diffusion due to ECH waves occurs at both progressively lower energies (due to the wave scattering in a progressively stretched field topology) and higher energies (due to the reduction of  $D_{SD}$ ), going from  $\sim 0.2\text{-}1\text{keV}$  at  $X=-6.5 R_E$  to  $\sim 0.1\text{-}3\text{keV}$  at  $X=-32.5 R_E$ . This leads to efficient

pitch angle scattering of both lower and (most importantly for powering the aurora) higher energy electrons in the middle to outer magnetotail.

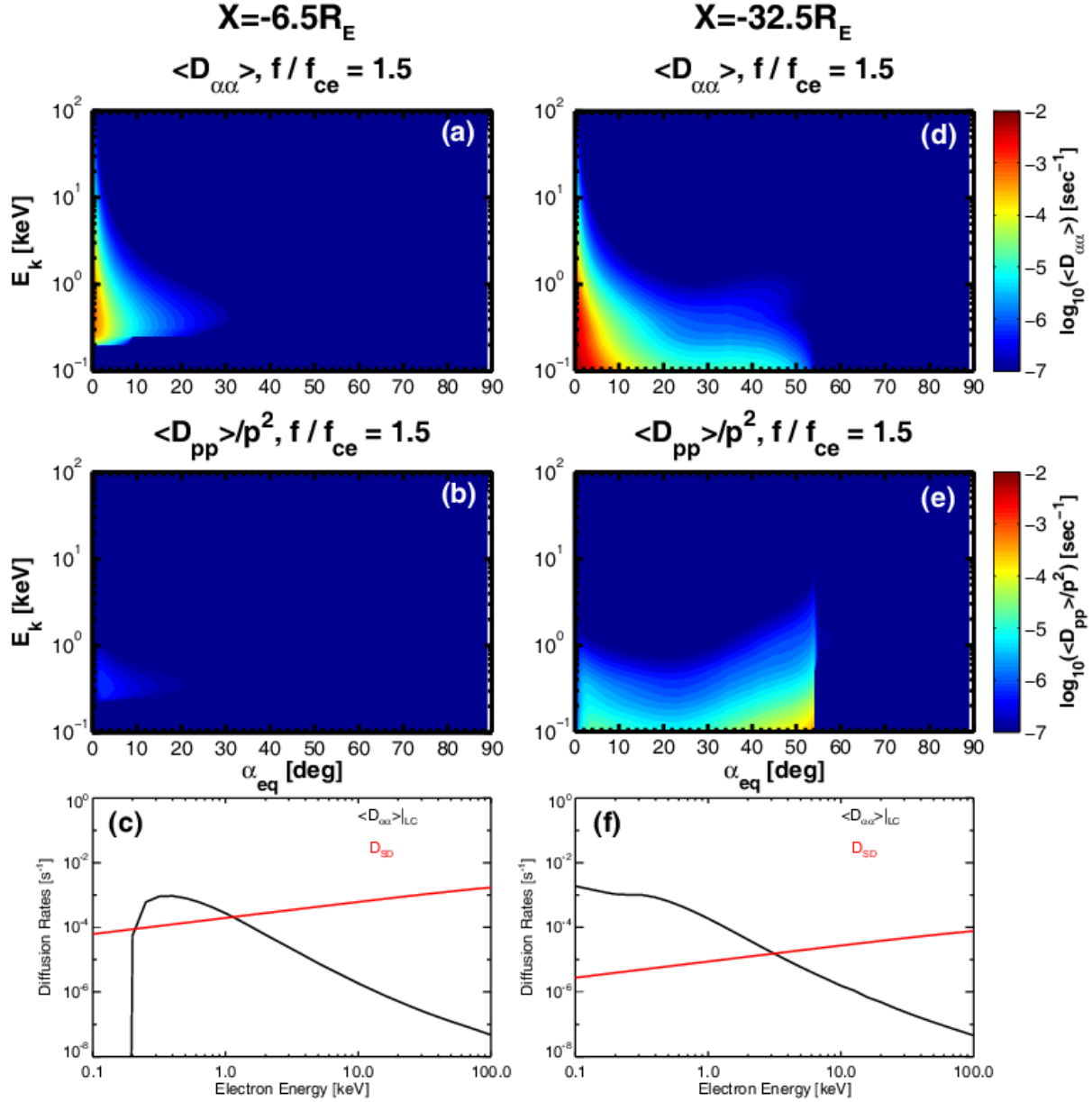


**Figure 5.6:** Bounce-averaged pitch-angle (a and d) and momentum (b and e) diffusion coefficients as a function of equatorial pitch angle and electron kinetic energy due to ECH waves. (e and f) Comparison of pitch-angle diffusion coefficients at the equatorial loss cone edge

$\langle D_{\alpha\alpha} \rangle|_{LC}$  with strong diffusion rate  $D_{SD}$ . The left column (a-c) is the result at  $X=-6.5 R_E$ ,  $Y=-1.0 R_E$ ; the right column (d-f) is the result at  $X=-32.5 R_E$ ,  $Y=-1.0 R_E$ .

### 5.3.3 Modeling Electron Diffusion Using Quasi-linear Theory

Using the resonant scattering rates quantified above, we now model the evolution of the electron pitch-angle distribution by its interaction with ECH waves using the 2-D bounce-averaged Fokker-Planck equation (Equation 5.3), to estimate the loss cone fill ratio at various locations throughout the magnetotail

$$\begin{aligned} \frac{\partial f}{\partial t} = & \frac{1}{S_0 \sin \alpha_{eq} \cos \alpha_{eq}} \frac{\partial}{\partial \alpha_{eq}} (S_0 \sin \alpha_{eq} \cos \alpha_{eq} \langle D_{\alpha\alpha} \rangle \frac{\partial f}{\partial \alpha_{eq}}) \\ & + \frac{1}{p^2} \frac{\partial}{\partial p} (p^2 \langle D_{pp} \rangle \frac{\partial f}{\partial p}) - \frac{f}{\tau}. \end{aligned} \quad (5.3)$$

Here  $p$  is the particle momentum,  $\alpha_{eq}$  is the equatorial pitch angle,  $S_0$  is the bounce period-related term, and  $\langle D_{\alpha\alpha} \rangle$  and  $\langle D_{pp} \rangle$  are the bounce-averaged pitch-angle and momentum diffusion coefficients, respectively. Mixed diffusion terms  $D_{\alpha p}$  were omitted in this equation. The loss time  $\tau$  is set to one quarter of the bounce period ( $\tau_B$ ) if  $\alpha_{eq}$  is less than the local loss-cone angle  $\alpha_{LC}$  and infinity otherwise. Our neglect of mixed diffusion terms simplifies the algorithm and reduces the computation time, while retaining the dominant diffusion process that affects plasma sheet electrons [e.g., *Albert and Young, 2005*].

The magnetic field-related parameters ( $S_0$  and  $\tau$ ) in Equation (5.3) are numerically evaluated for the T89 magnetic field following *Ni et al.* [2012a]. Since we compute the loss cone fill ratio out of the resultant electron distributions, the absolute PSD values do not affect our modeling—we are interested in changes inside the loss cone relative to the PSD value outside. Generic initial conditions are therefore adopted from THEMIS observations, after suppressing anisotropies of the hot component outside the loss cone. Boundary conditions are the same as used in Chapter 2:  $\partial f / \partial \alpha_{eq} = 0$  at  $\alpha_{eq} = 0^\circ$  and at  $\alpha_{eq} = 90^\circ$  for the pitch-angle operator. As shown in Figure 5.6, pitch angle diffusion rates may exceed the strong diffusion limit; we thus use the zero gradient condition at the low pitch angle boundary (applicable to both weak and strong diffusions) in this study. For the energy diffusion operator, the lower boundary was held constant at 55eV because the diffusion timescale of these electrons is much longer than that of typical plasma sheet electrons; the upper boundary was also held fixed at 23keV, well above typical resonant energies of ECH waves with plasma sheet electrons (hundreds of eV to several keV).

Figure 5.7 shows modeled results for the evolution of electron distributions at  $X=-6.5 R_E$ ,  $Y=-1.0 R_E$  and  $X=-32.5 R_E$ ,  $Y=-1.0 R_E$ . We assume that the steady-state has been reached when the electron PSD over potentially resonant energies (100eV to 5keV) changes less than 1% in one time step (2 sec); the electron distributions for that state are shown in Figures 5.6c and 5.6f. The loss cone fill ratio is then estimated using the median value of resultant PSD within the loss cone divided by that at the edge of the loss cone.

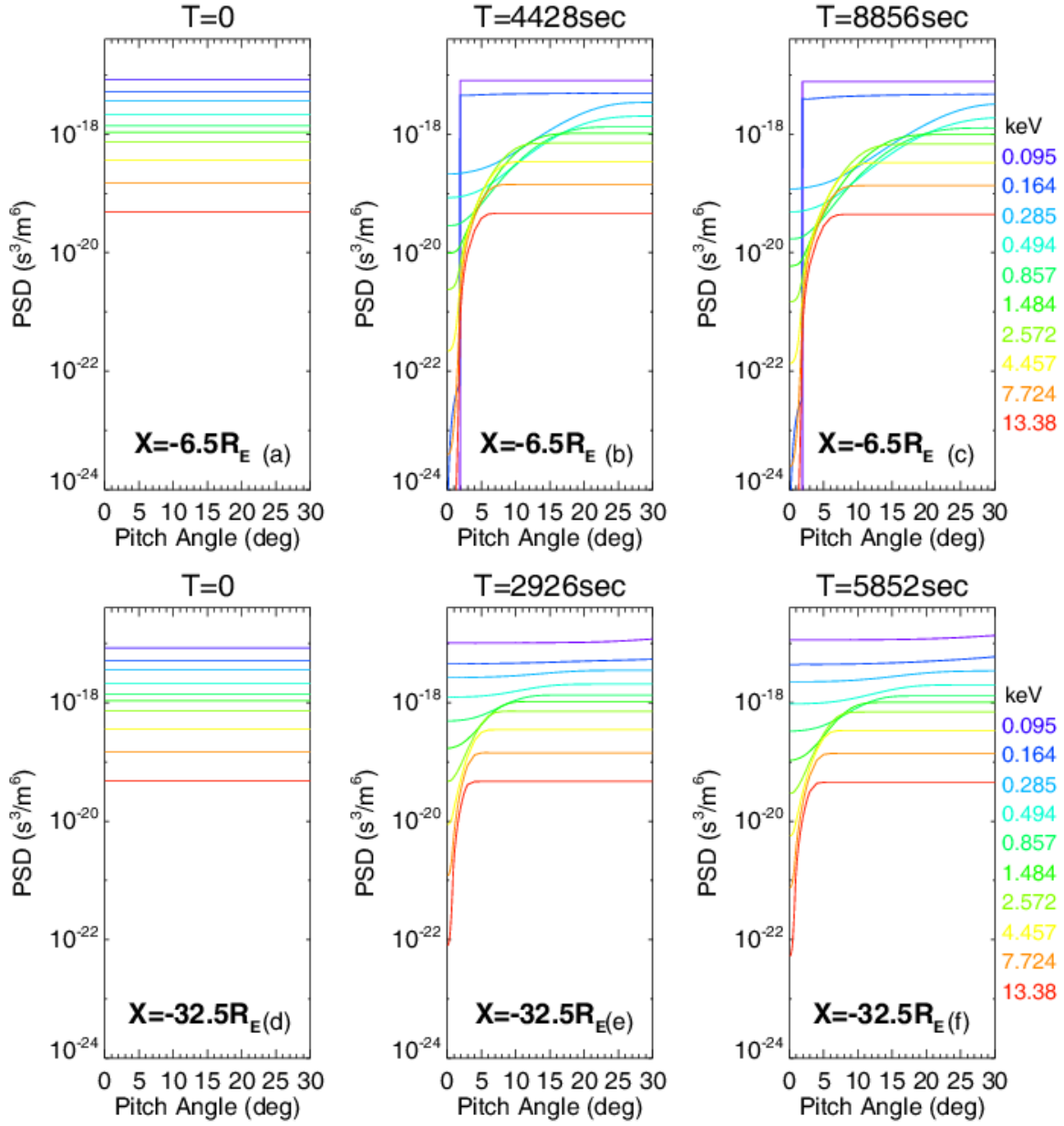


**Figure 5.7:** Initial electron distribution (isotropic) for modeling the diffusion process and the evolution of electron distribution after interaction with ECH waves at two time instants, with the last one (c and f) showing the distribution at the steady-state. The upper panels (a-c) show the results at  $X=-6.5 R_E$ ,  $Y=-1.0 R_E$ ; the bottom panels (d-f) exhibit the results at  $X=-32.5 R_E$ ,  $Y=-1.0 R_E$ .

## 5.4 Estimated Precipitation due to ECH Wave Scattering

Assuming isotropic differential energy flux within a loss cone, the ionospheric precipitation from ECH wave scattering plasma sheet electrons can be estimated by [Ni *et al.*, 2012a]:

$$\Phi = \pi \int_{E_1}^{E_2} \chi_{(E)} J_{(E, \alpha_{LC})} dE \quad (5.4)$$

where  $\Phi$  is the energy flux into the ionosphere,  $\chi_{(E)}$  is the loss cone fill ratio estimated above by modeling the electron distribution at the steady-state,  $J_{(E, \alpha_{LC})}$  is the electron differential energy flux near the equatorial loss cone approximated by the field-aligned energy flux from THEMIS ESA measurements, and  $dE$  is the width of each energy channel.

The electron differential energy fluxes within the equatorial loss cone using the estimated fill ratios are shown in Figure 5.8 for the two cases discussed in Figures 5.6 and 5.7.  $\chi_{(E)}$  is very close to 1 for electrons with pitch angle scattering rate exceeding the strong diffusion rate, but it drops dramatically for other energies with lower diffusion rates than the strong diffusion limit. It is evident by comparing Figures 5.7a and 5.7b that ECH waves can fill in the loss cone more efficiently at  $X=-32.5 R_E$ ,  $Y=-1.0 R_E$ , especially for electrons at higher energies ( $>2\text{keV}$ ).

By summing up the electron energy fluxes inside the loss cone (following Equation 5.4), we estimate electron precipitation caused by ECH wave scattering, shown in Figure 5.9. The ECH wave-induced electron precipitation is predominant in the dusk sector at larger distances (beyond  $20 R_E$ ), and becomes more intense in the dawn sector closer to the Earth (within  $20 R_E$ ), which agrees well with diffuse aurora precipitation (OVATION Prime model result) mapped from the ionosphere during low solar wind driving conditions (Figure 5.9a). ECH wave-induced

precipitation contributes at most 50% of the total energy flux associated with the diffuse aurora in the inner magnetotail ( $X=-6.5R_E$ ,  $|Y|\leq 3R_E$ ). However, the ECH wave-contributed energy flux becomes closer to 100% of the anticipated energy flux in the diffuse aurora in the middle to outer magnetotail (within  $20 R_E$ ). Beyond  $25 R_E$ , although the loss cone fill ratio is high, the estimated precipitation is inadequate to account for the expected diffuse aurora ionospheric power due to the low electron temperature (and field aligned energy flux) in the plasma sheet at those distances.

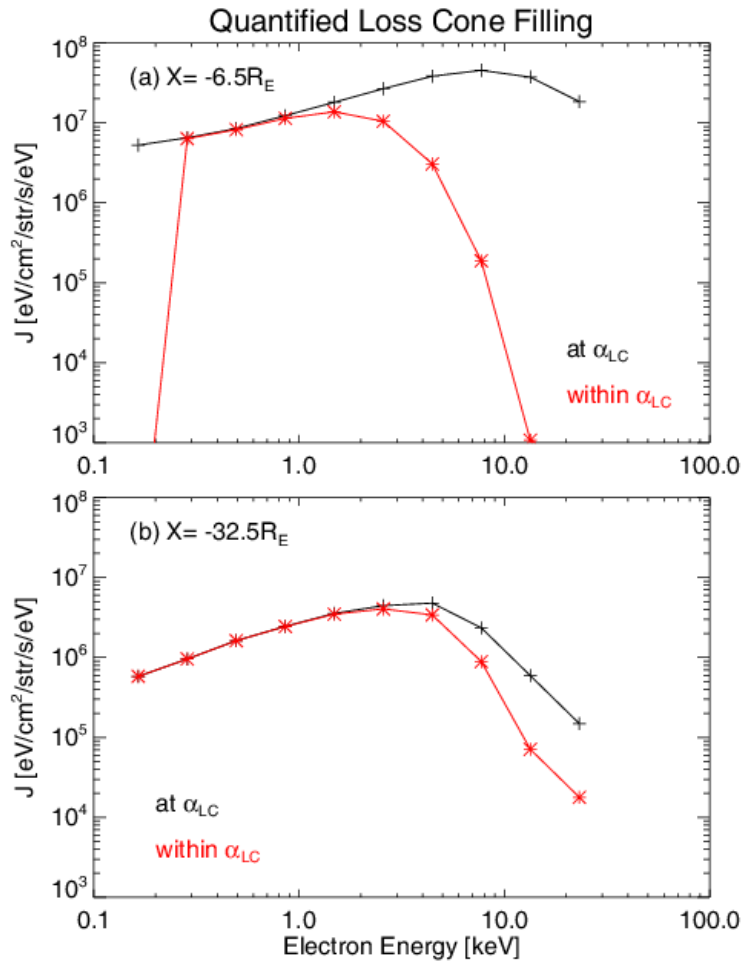


**Figure 5.8:** Electron differential energy flux at the equatorial loss cone (black curve) approximated by the field-aligned energy flux from THEMIS ESA measurements, in comparison

with the differential energy flux within the loss cone (red curve) estimated using the loss cone fill ratio due to ECH wave scattering. The upper panel (a) shows the result at  $X=-6.5 R_E$ ,  $Y=-1.0 R_E$ , while the bottom panel (b) is the result at  $X=-32.5 R_E$ ,  $Y=-1.0 R_E$ .

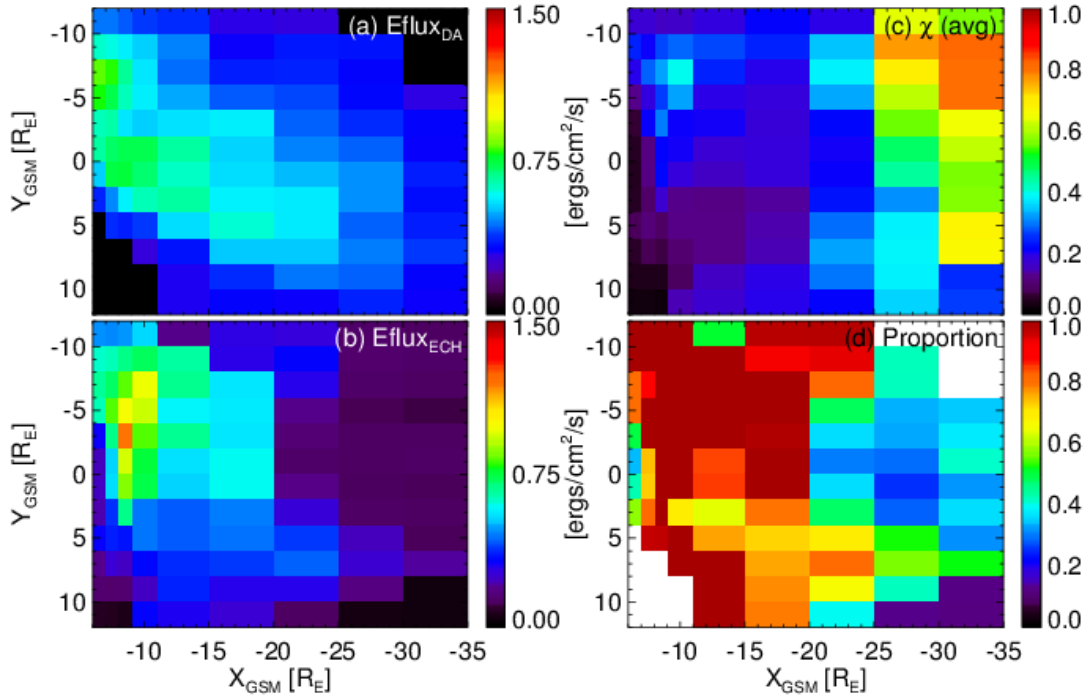


**Figure 5.9:** Distribution of (a) ionospheric diffuse aurora precipitation energy flux mapped to the magnetic equator during low solar wind driving conditions, (b) ECH wave-induced electron precipitation, (c) loss cone fill ratio computed as the ECH wave-induced precipitating energy flux divided by that at the strong diffusion limit, and (d) proportion of diffuse aurora precipitation contributed ECH wave scattering.

## 5.5 Summary and Discussion

We modeled the diffuse auroral precipitation using OVATION Prime model [Newell *et al.*, 2009, 2010] and mapped the energy flux to the magnetic equator using T89 and T96 magnetic field models [Tsyganenko, 1989; Tsyganenko and Stern, 1996]. We used parameters during quiet solar wind conditions for both T89 and T96 models, which may underestimate the equatorial mapping distance of a certain magnetic latitude. Nevertheless, we found that the nightside diffuse auroral precipitation is dominated by dissipations from the middle to outer magnetotail ( $R > 8$ ) during low solar wind driving conditions (Figure 5.1). For high solar wind driving, precipitation from these high L-shells accounts for only ~40% of the entire nightside energy fluxes. This decrease, as also shown in Figure 1.4 during active times, is probably due to the intensified whistler mode chorus emissions during active times in the inner magnetosphere.

In order to determine the origin of these high L-shell precipitations, we investigated the distribution of chorus emissions in comparison with that of ECH waves. We found that chorus emissions are statistically weak (a few pT) (Figure 5.3), consistent with previous studies [Li *et al.*, 2009b]. We further examined the distribution of plasma parameters relevant to the generation of chorus waves. Our results indicate that intense chorus waves are confined to regions where the ratio between the plasma frequency and cyclotron frequency ( $f_{pe}/f_{ce}$ ) is less than 5 (Figure 5.4d), which agrees with previous investigations [Li *et al.*, 2010]. The perpendicular temperature anisotropy (from ESA measurements) only exists at  $X > -8 R_E$  (Figure 5.4b), consistent with the preferred location of intense chorus emissions. This temperature anisotropy can provide free energy for the excitation of upper-band chorus (resonates with electrons at energies between 500 eV and a few keV). As shown in Figure 5.4b, absence of such a free energy source beyond  $\sim 8 R_E$

further indicates chorus waves may not exist outside inner magnetotail, and therefore insufficient to account for the scattering of plasma sheet electrons beyond  $\sim 8 R_E$ , where diffuse aurora is still very intense. However, moderately strong ECH waves (wave amplitude  $>0.1$  mV/m) can still be observed even beyond  $X=-20 R_E$ , indicating that ECH wave can potentially be a driver of high latitude diffuse aurora.

We then numerically modeled the interaction between plasma sheet electrons and ECH waves to estimate the loss cone fill ratio and the corresponding electron precipitation due to ECH wave scattering. To quantify the diffusion coefficients realistically, we first obtained the distribution of wave amplitude and magnetic field magnitude (realistically adjusting the electron cyclotron frequency and the loss cone size in the model) statistically from THEMIS ECH wave database, as presented in Figure 5.2. After block-averaging, we obtained realistic but smoothly varying spatial distributions of wave amplitude, magnetic field magnitude, field line curvature and temperature for use in further modeling of ECH wave growth, propagation and estimation of the diffusion coefficients. In addition, the (hot plasma) dispersion relation requires knowledge of the total-to-cold electron density ratio phase-space gradient near the loss cone and temperature anisotropy of thermal electrons. With regards to the cold electron density, current instruments cannot measure low energy electron densities accurately enough due to the presence of photoelectrons (a few eV range) and back-scattered electrons (occasionally up to tens of eV range) in the measured distributions. Moreover, past and future instruments are not equipped with angular resolution sufficient to measure the distribution function or its gradients within the loss cone. To eliminate fluctuations in the wave number due to uncertainties of these plasma parameters, we fixed the minimum resonant energy (500eV) at each location and used a constant wave normal angle ( $89.5^\circ$ ) at the equator, both of which are typical values for ECH waves. For

the wave latitudinal extent, which cannot be inferred from observations, we assumed reasonable estimates preserving the trend of progressive latitudinal confinement with increasing distance from the Earth, due to increased field line curvature. We intentionally adopted the same latitudinal confinement (at  $X=-12.5 R_E$ ,  $Y=-1 R_E$ ) as used in the case study by *Ni et al.* [2012a] at  $L=11.5$  in order to cross-check and compare our results with theirs. Their (active plasma sheet) pitch angle diffusion coefficients are about four times larger than our (average, and thus preferentially inactive plasma sheet) results at all energies, due to the factor of 2 smaller wave amplitude adopted in our study. This indicates that our single frequency approximation compares well with their multiple frequency (intensity-weighted) diffusion coefficients, and can thus adequately represent the actual wave particle interactions. Our numerically estimated loss cone fill ratio also agrees well with the analytical solution used by *Ni et al.* [2012a] under steady-state condition: both studies obtain a fill ratio close to 1 for electrons with energy  $<1.5$  keV (the transition from strong diffusion rate to moderate diffusion rate). But at higher energies, the smaller scattering rates in our study lead to much lower loss cone fill ratios, as expected.

Due to the decrease in loss cone size and increase in field line stretching, our strong diffusion rate drops with distance from the Earth, leading to more efficient scattering of plasma sheet electrons and high loss cone fill ratios in the middle to outer magnetotail. Using these loss cone fill ratios obtained from modeling electron diffusion, we were able to quantify the precipitation by integrating the field-aligned electron energy fluxes over ESA instrument energies, assuming they represent the fluxes at the edge of the loss cone. The ECH wave-induced precipitation (Figure 5.9b) is predominant at pre-midnight beyond  $20 R_E$  and migrates towards dawn side in the inner magnetosphere, which resembles the modeled pattern of diffuse aurora (Figure 5.9a). As shown in Figure 5.2c, there is almost no dawn-dusk asymmetry in the electron energy flux

distribution within  $\sim 10 R_E$ ; thus, the dawnward preference of wave-induced precipitation at this region mainly results from larger wave amplitude and smaller loss cone size at the dawn sector (Figures 5.2a and 5.2d), corresponding to enhanced scattering from ECH waves. Electron energy fluxes beyond  $25 R_E$  cannot account for the diffuse aurora even at strong diffusion limit, leading to the small contributions of ECH wave-induced precipitations (Figure 5.9d). This discrepancy may be related to insufficient data points beyond  $25 R_E$ ; it may also be related to the fact that at such high latitudes, *Newell et al.* [2009, 2010] may have inadvertently included discrete aurora in their diffuse aurora bins, due to their strict criteria in categorizing discrete aurora.

As far as we know, our study is the first attempt to quantitatively evaluate the contribution of ECH waves to diffuse auroral precipitation throughout the magnetotail. By numerically modeling the ECH wave-induced electron precipitation and evaluating the contribution relative to the diffuse aurora energy flux modeled at the ionosphere, we were able to quantify the role of ECH waves in driving diffuse aurora globally and directly. Adopting quasi-linear theory and a realistic non-dipolar magnetic field topology on the basis of OVATION Prime model, we concluded that ECH waves are the major contribution to diffuse aurora in the middle to outer magnetotail, while the dominant driver of low-latitude diffuse electron precipitations is likely chorus waves, as previously discussed by *Thorne et al.* [2010] and *Ni et al.* [2011c].

# CHAPTER 6

## Summary and Future Work

### 6.1 Summary

This dissertation investigated the excitation of ECH waves under different plasma sheet conditions, and evaluated the role of ECH waves in driving diffuse aurora based on the global statistical features of these waves and a systematical modeling of the wave scattering effects. With general introduction, scientific background, historic review, motivation and objective presented in the first Chapter, we summarize the main results of this dissertation as follows:

In Chapter 2, we evaluated the ECH wave electric field amplitudes during quasi-steady state at different locations of magnetotail using idealized but physically accurate models. Decreasing trends of wave amplitudes with increasing L-shell (due to the progressively smaller loss cone sizes) explains the contradictory results between the presence of diffuse auroral precipitation at higher latitudes (up to about  $70^\circ$  MLAT) [Newell *et al.*, 2009] and relative scarcity of ECH waves in high L-shells ( $L > \sim 12$ ). Our results suggest that such ECH emissions at high L-shells ( $L > \sim 12$ ) may be present, which may then cause the observed precipitation, even though evidence of these waves may be scarce at current datasets due to their small amplitude.

In Chapter 3, we investigated the relationship between ECH wave intensifications and electron injections (accompanied by lower energy electrons resonant with ECH waves), relevant for linear growth rates, and DFs, relevant for wave propagation. Using three comprehensive databases of ECH wave events, injections, and DFs from THEMIS observations, we statistically

established a temporal correlation between ECH waves, injections, and DFs: 71% of ECH events are correlated with electron injections and 52% are correlated with DFs. ECH response time relative to injections increases from  $\sim 300$  sec at the pre-midnight region to  $\sim 800$  sec at the post-midnight region, indicating a causal relationship between ECH wave intensification and dawnward drifting electrons from injections. It may be the more dipolarized field configuration after DF passage that leads to less latitudinal confinement of the high-amplitude ECH waves around the neutral sheet.

Chapter 4 further examined the spatial distribution and the extent of ECH emissions under various plasma sheet conditions. Single-spacecraft data analysis shows that ECH waves are prevalent in the midnight and post-midnight magnetotail and that their occurrence rates decrease with increasing radial distance from Earth. Their distribution is almost symmetric across the midnight meridian within  $10 R_E$ ; excluding emissions correlated with local plasma sheet dynamics, we found that ECH emissions show a clear preference for the dawn sector. This preference suggests these waves may be related to injected electrons that drift away from their original flow channels at pre-midnight. Using simultaneous multi-probe observations, we investigated ECH waves' extent with finer scales than in single spacecraft occurrence rate studies: the  $Z$ -extent is  $\sim 0.5 R_E$ , the  $Y$ -extent is  $\sim 2 R_E$ , and the  $X$ -extent is at least  $4 R_E$ . Waves not related to injections and DFs demonstrate a smaller  $Z/X$ -extent than those in the entire wave database, but a similar  $Y$ -extent. In order to investigate the mechanism leading to the different  $Z$ -extents under various plasma sheet conditions, we also used HOTRAY ray-tracing code to model the wave power distribution as a function of distance from the neutral sheet. Our results show a linear correlation between the wave  $Z$ -extent and field line curvature radius ( $R_c$ ) and provide a realistic estimate of the wave extent for a given  $R_c$ .

In Chapter 5, we estimated the ECH wave-induced precipitation and quantitatively evaluated the contribution of ECH waves to diffuse aurora throughout the entire magnetotail. Observation-based parameters (wave, electron and magnetic field) ensure realistic quantifications of diffusion coefficients and subsequent estimations of loss cone fill ratio. By comparing the modeled precipitating energy flux to the diffuse aurora distribution mapped to the magnetotail, we found that ECH wave is the dominant driver of diffuse aurora beyond  $\sim 8 R_E$ . In the inner magnetotail, however, ECH wave scattering of plasma sheet electrons cannot account for the diffuse aurora precipitation.

The results presented in this dissertation greatly improve current understanding of the excitation mechanisms of ECH waves and their interactions with plasma sheet electrons. Excited by the loss-cone instability of the hot plasma sheet electrons, ECH waves can be intensified by local plasma sheet activity, such as electron injections and DFs, which create plasma sheet conditions favorable for wave growth in their aftermath: a dipolarized flux region following DFs, and increased energy fluxes along the dawnward-drifting paths of injected electrons. Correspondingly, low-amplitude ECH emissions could contribute to drizzle precipitation of diffuse aurora during quiet conditions; intensified ECH waves following plasma sheet activities may dominate the wave observations in the middle to outer magnetotail, contributing to enhanced diffuse auroral precipitation in higher magnetic latitudes during such active times.

Based on the above knowledge of ECH wave properties, we were able to quantify ECH waves' contribution to diffuse aurora precipitation systematically throughout the entire magnetotail. Our results resolved the long-standing issue of ECH waves' role in the diffuse aurora origin, confirming their predominance in the middle to outer magnetotail.

## 6.2 Future Work

### 6.2.1 Parametric Study on ECH Wave Growth Rate

As discussed in Section 1.5.2, due to observational limitations, we cannot directly estimate the wave growth rate using measured electron distributions. Solving the hot plasma dispersion relation has to rely on assumed cold electron distributions and electron phase space density gradients near the loss cone edge. We made generic assumptions of such parameters in this dissertation to avoid any effects due to their variations in estimating the growth rate. To fully understand the generation of ECH waves without improved instrumentations, further efforts should be devoted to how these undetectable parameters affect the wave growth in theory.

In the future, we plan to conduct a parametric study on the wave temporal and spatial growth rates driven by a loss cone distribution, for different cold electron densities ( $n_c/n_h$ ), cold electron temperatures ( $T_c/T_h$ ), and hot electron temperature anisotropies ( $T_{h,\perp}/T_{h,\parallel}$ ). This result will advance our knowledge on the generation and damping of ECH waves in the realistic space environment. It can also provide guidance for the parameter assumptions in the future work.

### 6.2.2 ECH Wave Excitation and Scattering in the Inner Magnetosphere

In this dissertation, we have investigated the wave excitation, intensification and scattering effects mainly in the middle to outer magnetotail ( $X_{\text{GSM}} \leq -6 R_E$ ). Twin Van Allen Probes were launched into an equatorial orbit with a perigee of  $\sim 1.1 R_E$ , apogee of  $5.8 R_E$  on 30 August 2012 [Mauk *et al.*, 2012]. Equipped with comprehensive particle and field instruments, measuring ions and electrons from  $\sim 1$  eV to 10's of MeV, DC magnetic fields, and electromagnetic waves from

10 Hz up to 400 kHz, the two Van Allen Probes are ideal for capturing ECH and chorus emissions in the inner equatorial magnetosphere. With sufficient database in a complete MLT survey of the inner magnetosphere, we plan to investigate the spatial distribution of ECH waves (including occurrence rate, amplitude, and extent) in the inner magnetosphere, complementary to what has been demonstrated using THEMIS database.

Using the new wave dataset from Van Allen Probes, we also intend to examine the ECH wave intensifications to verify whether they are also correlated with plasma sheet activities, such as electron injections. Investigating the wave intensification during different magnetotail dynamics in the inner magnetotail will shed light on the wave excitation mechanism under various conditions at different regions.

Similar to Chapter 5, based on the improved global distribution of ECH emissions in the inner magnetosphere, we also plan to further model the ECH wave scattering effect in that region to verify their role in driving diffuse aurora precipitation.

### **6.2.3 Improved Model of ECH Wave Scattering Plasma Sheet Electrons**

As discussed in Chapters 2 and 5, ECH wave-induced momentum diffusion rates and mixed diffusion rates are smaller than the pitch angle diffusion rates, especially near the loss cone edge (at least one order of magnitude smaller). We thus neglected mixed diffusion terms ( $D_{ap}$ ) to simplify the algorithm and reduce the computation time, while retaining the dominant diffusion process that affects plasma sheet electrons [e.g., *Albert and Young, 2005*]. Considering we are modeling the diffusion process to mainly obtain the loss cone fill ratio, dramatic differences are not expected. However, in order to verify our result presented in Chapter 5 and further adapt our

model for other wave modes (such as chorus waves), we plan to improve our model by including the cross diffusion coefficients in solving the bounce-averaged Fokker-Planck equation.

As shown by *Xiao et al.* [2009] and *Tao et al.* [2011], the alternative direction implicit method can still be used to numerically solve the 2-D bounce-averaged Fokker-Planck equation when mixed diffusion terms are added:

$$\begin{aligned} \frac{\partial f}{\partial t} = & \frac{1}{S_0 \sin \alpha_{eq} \cos \alpha_{eq}} \frac{\partial}{\partial \alpha_{eq}} [S_0 \sin \alpha_{eq} \cos \alpha_{eq} (\langle D_{\alpha\alpha} \rangle \frac{\partial f}{\partial \alpha_{eq}} + \langle D_{\alpha p} \rangle \frac{\partial f}{\partial p})] \\ & + \frac{1}{p^2} \frac{\partial}{\partial p} [p^2 (\langle D_{\alpha p} \rangle \frac{\partial f}{\partial \alpha_{eq}} + \langle D_{pp} \rangle \frac{\partial f}{\partial p})] - \frac{f}{\tau}. \end{aligned} \quad (6.1)$$

Here  $p$  is the particle momentum,  $\alpha_{eq}$  is the equatorial pitch angle,  $S_0$  is the bounce period-related term, and  $\langle D_{\alpha\alpha} \rangle$ ,  $\langle D_{\alpha p} \rangle$ , and  $\langle D_{pp} \rangle$  are the bounce-averaged pitch-angle, mixed, and momentum diffusion coefficients, respectively. The challenge of solving Equation (6.1) would be to manipulate the time step to prevent numerical instability due to the rapidly varying cross diffusion coefficients.

## APPENDIX A

### Bounce-averaged Diffusion Coefficients in a Non-dipolar Magnetic Field

The local pitch angle diffusion coefficient for electrons due to ECH waves is given by [Lyons, 1974]:

$$D_{\alpha\alpha} = \sum_{N=-\infty}^{+\infty} \int k_{\perp} dk_{\perp} [\Psi_{N,k} \left( \frac{N\Omega_e / \omega_k - \sin^2 \alpha}{\sin \alpha \cos \alpha} \right)^2]_{k_{\parallel}=k_{\parallel, \text{res}}} \quad (\text{A.1})$$

$$\text{with } \Psi_{N,k} = \frac{1}{4\pi} \frac{e^2}{m_e^2} \frac{|E_k|^2}{V} \left( \frac{\omega_k}{|k|} \right)^2 \frac{J_N^2(k_{\perp} v_{\perp} / \Omega_e)}{v^4 |v_{\parallel} - \partial \omega_k / \partial k_{\parallel}|}, \quad (\text{A.2})$$

where  $k_{\perp}$  and  $k_{\parallel}$  are the wave vector perpendicular and parallel to the ambient magnetic field  $\mathbf{B}_0$ , respectively,  $k_{\parallel, \text{res}} = (\omega_k - N\Omega_e / \gamma) / v_{\parallel}$  is the resonant parallel wave number,  $\Omega_e = |eB_0 / m_e|$  is the angular electron gyrofrequency,  $\omega_k$  is the wave frequency as a function of  $k$ ,  $\gamma = (1 - v^2 / c^2)^{-1/2}$  is the Lorentz factor with  $v$  denoting the electron velocity and  $c$  is the speed of light,  $\alpha$  is the electron pitch angle,  $V$  is the plasma volume,  $e / m_e$  is the electron charge to mass ratio, and  $J_N$  is the Bessel function of order  $N$ . Assuming that the parallel group velocity is small compared to the electron parallel velocity ( $\partial \omega_k / \partial k_{\parallel} \ll v_{\parallel}$ ) and that the electric field spectrum has the form of

$$|E_k|^2 = C k_{\perp}^2 \exp\left[-\left(\frac{k_{\perp}}{k_{0,\perp}}\right)^2\right] \cdot \left\{ \exp\left[-\left(\frac{k_{\parallel} - k_{0,\parallel}}{\delta k_{\parallel}}\right)^2\right] + \exp\left[-\left(\frac{k_{\parallel} + k_{0,\parallel}}{\delta k_{\parallel}}\right)^2\right] \right\} \quad (\text{A.3})$$

with a normalization constant

$$C = \frac{4\pi^{3/2}}{k_{0,\perp}^4 \delta k_{\parallel}} V |E_w|^2 \quad (\text{A.4})$$

obtained from

$$\int |E_w|^2 dr = \frac{1}{8\pi^3} \int |E_k|^2 dk, \quad (\text{A.5})$$

*Horne and Thorne* [2000] developed the local pitch angle diffusion coefficient into a modified version:

$$D_{\alpha\alpha} = \frac{\sqrt{\pi}}{2} \frac{e^2}{m_e^2} \frac{|E_w|^2}{k_{0,\perp}^2 \delta k_{\parallel}} \frac{\exp(-\mu)}{v^5 \cos \alpha} \cdot \sum_{N=-\infty}^{+\infty} \left( \frac{N\Omega_e / \gamma - \omega_k \sin^2 \alpha}{\sin \alpha \cos \alpha} \right)^2 \cdot I_N(\mu) \{ \exp[-(\zeta_N^-)^2] + \exp[-(\zeta_N^+)^2] \} \quad (\text{A.6})$$

where  $k_{0,\perp}$  and  $k_{0,\parallel}$  are the wave number perpendicular and parallel to the ambient magnetic field  $\mathbf{B}_0$ , respectively,  $\delta k_{\parallel}$  is the width of the wave spectrum over parallel wave number,  $N$  is the resonance order associated with the resonance condition and the summation includes all the possible resonance harmonics,  $I_N(\mu)$  is the modified Bessel function with argument

$$\mu = k_{0,\perp}^2 v_{\perp}^2 / (2\Omega_e^2), \text{ and } \zeta_N^{\pm} = \frac{\omega_k - N\Omega_e / \gamma \pm k_{0,\parallel}}{\delta k_{\parallel} v \cos \alpha}.$$

Local cross diffusion rate  $D_{\alpha p}$  and momentum

diffusion rate  $D_{pp}$  can then be obtained by [e.g., *Lyons*, 1974]:

$$D_{\alpha p} = D_{\alpha\alpha} \left[ \frac{\sin \alpha \cos \alpha}{N\Omega_e / (\gamma \omega_k) - \sin^2 \alpha} \right],$$

$$D_{pp} = D_{\alpha\alpha} \left[ \frac{\sin \alpha \cos \alpha}{N\Omega_e / (\gamma \omega_k) - \sin^2 \alpha} \right]^2. \quad (\text{A.7})$$

Following *Ni et al.* [2011d, 2012b], for non-dipolar fields, the quasi-linear bounce-averaged diffusion coefficients along the particle bounce trajectory, assuming the field line lies in a plane perpendicular to the magnetic equator, can be written as

$$\begin{aligned}
\langle D_{\alpha_0\alpha_0} \rangle &= \frac{\int_{\lambda_{m,s}}^{\lambda_{m,n}} \frac{D_{\alpha\alpha}(\alpha)}{\cos \alpha} \left( \frac{\tan \alpha_0}{\tan \alpha} \right)^2 \sqrt{r^2 + \left( \frac{\partial r}{\partial \lambda} \right)^2} d\lambda}{\int_{\lambda_{m,s}}^{\lambda_{m,n}} \sec \alpha \sqrt{r^2 + \left( \frac{\partial r}{\partial \lambda} \right)^2} d\lambda}, \\
\langle D_{\alpha_0 p} \rangle &= \frac{\int_{\lambda_{m,s}}^{\lambda_{m,n}} \frac{D_{\alpha p}(\alpha)}{\cos \alpha} \frac{\tan \alpha_0}{\tan \alpha} \sqrt{r^2 + \left( \frac{\partial r}{\partial \lambda} \right)^2} d\lambda}{\int_{\lambda_{m,s}}^{\lambda_{m,n}} \sec \alpha \sqrt{r^2 + \left( \frac{\partial r}{\partial \lambda} \right)^2} d\lambda}, \\
\langle D_{pp} \rangle &= \frac{\int_{\lambda_{m,s}}^{\lambda_{m,n}} \frac{D_{pp}(\alpha)}{\cos \alpha} \sqrt{r^2 + \left( \frac{\partial r}{\partial \lambda} \right)^2} d\lambda}{\int_{\lambda_{m,s}}^{\lambda_{m,n}} \sec \alpha \sqrt{r^2 + \left( \frac{\partial r}{\partial \lambda} \right)^2} d\lambda},
\end{aligned} \tag{A.8}$$

where  $\langle D_{\alpha_0\alpha_0} \rangle$ ,  $\langle D_{\alpha_0 p} \rangle$  and  $\langle D_{pp} \rangle$  are bounce-averaged pitch angle scattering, mixed diffusion and momentum diffusion rates,  $D_{\alpha\alpha}$ ,  $D_{\alpha p}$  and  $D_{pp}$  are local diffusion rates,  $\alpha$  and  $\alpha_0$  are local and equatorial pitch angle,  $r$  is radial distance from the Earth,  $\lambda$  is magnetic latitude, and  $\lambda_{m,s}$  and  $\lambda_{m,n}$  are the mirror latitudes on the southern and northern hemisphere, dependent on the field line configuration and the field strength of adopted magnetic field model.

## APPENDIX B

### HOTRAY Ray-Tracing Code

The ray tracing program HOTRAY is designed to trace any type of electromagnetic or electrostatic wave mode in a hot, magnetized, linearly unstable plasma containing several electron and ion species with realistic unstable distribution functions (bi-Maxwellians) at different temperatures [Horne, 1989]. The spatial gradients in the plasma are assumed to be small compared to the wavelength. The code is limited to small amplitude waves (so that linear theory applies) and non-relativistic effects. Once the frequency is specified, the ray path can be found by integrating Hamilton's equations for a hot magnetized anisotropic plasma. The form of the equations used in HOTRAY is:

$$\frac{d\mathbf{R}}{dt} = -\frac{\partial D}{\partial \mathbf{k}} / \frac{\partial D}{\partial \omega} \quad (\text{B.1})$$

$$\frac{d\mathbf{k}}{dt} = -\frac{\partial D}{\partial \mathbf{R}} / \frac{\partial D}{\partial \omega} \quad (\text{B.2})$$

where  $\mathbf{R}$  is the position vector of a point along the ray path,  $\omega$  is the angular wave frequency,  $\mathbf{k}$  is the wave vector, and  $D$  is the dispersion relation. The integration is subject to the condition that the hot plasma dispersion relation must be satisfied at every point along the ray path, i.e.,

$$D(\mathbf{R}, \mathbf{k}, \omega) = 0 \quad (\text{B.3})$$

In general, the solutions to this equation (B.3) are complex, and hence, after integration, both  $\mathbf{k}$  and  $\mathbf{R}$  are complex. However, only the real part of Equations B.1 and B.2 is used in the integration in this code. The results are therefore valid provided the imaginary part remains small.

The right-hand side of Equation B.1 can be identified as the group velocity and obtained directly from the dispersion relation at a given  $\mathbf{R}$ . Equation B.2 depends on the spatial variation of the magnetic field  $\mathbf{B}$ , plasma density  $N$ , and wave vector  $\mathbf{k}$ .  $\frac{\partial D}{\partial \mathbf{R}}$  can be expressed as:

$$\frac{\partial D}{\partial \mathbf{R}} = \frac{\partial D}{\partial \mathbf{B}} \frac{\partial \mathbf{B}}{\partial \mathbf{R}} + \frac{\partial D}{\partial N} \frac{\partial N}{\partial \mathbf{R}} + \frac{\partial D}{\partial \mathbf{k}} \frac{\partial \mathbf{k}}{\partial \mathbf{R}}. \quad (\text{B.4})$$

The first two differentials can be obtained once the magnetic field and plasma density model are defined. HOTRAY code uses dipole magnetic field originally. In order to study the ECH wave propagation in a more realistic field morphology outside the inner magnetotail, we adapted the code for a Dungey and a modified Harris sheet magnetic field topology respectively in Chapter 2 and Chapter 4. In our study, the density is assumed to be constant at all times with zero density gradients.

One of the important advantages of HOTRAY is that the path-integrated growth rate,  $\Gamma$ , can be calculated for ECH waves by:

$$\Gamma = \sum \mathbf{k}_i \cdot \Delta \mathbf{R} \quad (\text{B.5})$$

where  $\Delta \mathbf{R}$  is the change in position and  $\mathbf{k}_i$  is the spatial growth rate averaged between two successive points along the ray path. The net amplification of the wave electric field over a ray path  $\mathbf{r}$  (path-integrated gain  $G$  in dB) [Horne and Thorne, 1997; Li et al., 2009a]:

$$G = 20 \log_{10}(E / E_0) = 8.6859 \int \mathbf{k}_i \cdot d\mathbf{r} \quad (\text{B.6})$$

Since the imaginary part of Hamilton's equations is neglected during ray tracing, HOTRAY is limited to weakly damped or growing waves. Hot ray tracing is thus stopped when  $|\text{Im}(n)/\text{Re}(n)| > 0.05$ , where  $n$  is the wave refractive index. Heavily damped waves are usually of little interest, and therefore ray tracing is also stopped when the relative wave amplitude fall to less than 10% of its initial value.

In order to calculate Hamilton's equations, the particle distribution function must be defined for each particle species. The distribution function used in HOTRAY can include a temperature anisotropy, loss cone distribution, beam distribution or any combination of these three, given by:

$$f = \sum_i f_i$$

where each component  $f_i$  is expressed as:

$$f_i(v_{\parallel}, v_{\perp}) = \frac{n_i}{\pi^{2/3} \alpha_{\perp i}^2 \alpha_{\parallel i}} \exp\left[-\frac{(v_{\parallel} - v_{di})^2}{\alpha_{\parallel i}^2}\right] \cdot \left[\Delta_i \exp\left(-\frac{v_{\perp}^2}{\alpha_{\perp i}^2}\right) + \frac{(1 - \Delta_i)}{(1 - \beta_i)} \cdot \left(\exp\left(-\frac{v_{\perp}^2}{\alpha_{\perp i}^2}\right) - \exp\left(-\frac{v_{\perp}^2}{\beta_i \alpha_{\perp i}^2}\right)\right)\right]. \quad (\text{B.7})$$

Here  $n_i$  is the electron density,  $\alpha_{\perp i}$  and  $\alpha_{\parallel i}$  are the thermal velocities perpendicular and parallel to the ambient magnetic field,  $v_{di}$  is the drift velocity along the magnetic field, which is assumed to be zero in our study;  $\beta_i$  and  $\Delta_i$  determine the loss cone feature of the electron distribution.

Putting  $\Delta_i = 1$  ,  $v_{di} = 0$  , and  $\alpha_{//i} = \alpha_{\perp i}$  reduces the distribution function to a Maxwellian distribution.

## APPENDIX C

### OVATION Prime Model

OVATION Prime model was developed using 22 years (1984-2005) of energetic particle (up to 30keV) measurements from the polar-orbiting Defense Meteorological Satellite Program (DMSP) satellites [Newell *et al.*, 2010]. The model predicts the location and intensity of four types of aurora (an ion aurora and three types of electron aurora): monoenergetic, broadband, and diffuse [Newell *et al.*, 2009]. The model grid size is 0.25 h MLT by 0.5 degrees MLAT, with the latter covering 50°-89.5° for either the northern or the southern hemisphere.

Each type of aurora is given a separate linear regression fit to the solar wind coupling function [Newell *et al.*, 2007] that best predicts hemispheric global power:

$$d\Phi_{MP} / dt = v^{4/3} B_T^{2/3} \sin^{8/3}(\theta/2) \quad (C.1)$$

where  $v$  is the bulk wind speed,  $B_T = \sqrt{(B_y^2 + B_z^2)}$ , and  $\theta$  is the interplanetary magnetic field (IMF) clock angle in the  $B_y$ - $B_z$  plane. This function is used to make a linear fit of the auroral power for each type of aurora for each season:

$$\text{Auroral power}(\text{mlat\_bin}, \text{mlt\_bin}, \text{aurora\_type}, \text{season}) = a + b \cdot d\Phi_{MP} / dt \quad (C.2)$$

at each grid where the locations are given in Altitude Adjusted Corrected Geomagnetic Coordinates (AACGM).

Within each MLAT/MLT bin there are also three linear regression fits predicting the probability of observing each of three types of electron aurora, also as a function of  $d\Phi_{MP} / dt$ . Thus the energy flux of diffuse aurora at a given MLAT/MLT bin is based on the product of the fitted intensity of diffuse aurora, when it is present, with the probability of observing diffuse aurora (any spectrum not flagged as either broadband or monoenergetic is counted as diffuse).

## BIBLIOGRAPHY

- Albert, J. M., and S. L. Young (2005), Multidimensional quasi-linear diffusion of radiation belt electrons, *Geophys. Res. Lett.*, *32*, L14110, doi:10.1029/2005GL023191.
- Anderson, R. R., and K. Maeda (1977), VLF emissions associated with enhanced magnetospheric electrons, *J. Geophys. Res.*, *82*(1), 135-146.
- Angelopoulos, V., et al., (2008), First Results from the THEMIS Mission, *Space Sci. Rev.*, doi:10.1007/s11214-008-9378-4.
- Angelopoulos, V., C. F. Kennel, F. V. Coroniti, R. Pellat, M. G. Kivelson, R. J. Walker, C. T. Russell, W. Baumjohann, W. C. Feldman, and J. T. Gosling (1994), Statistical characteristics of bursty bulk flow events, *J. Geophys. Res.*, *99*(A11), 21,257-21,280, doi:10.1029/94JA01263.
- Angelopoulos, V., W. Baumjohann, C. F. Kennel, F. V. Coronti, M. G. Kivelson, R. Pellat, R. J. Walker, H. Luehr, and G. Paschmann (1992), Bursty bulk flows in the inner central plasma sheet, *J. Geophys. Res.*, *97*, 4027-4039, doi:10.1029/91JA02701.
- Angelopoulos, V., et al. (1997), Magnetotail flow bursts: Association to global magnetospheric circulation, relationship to ionospheric activity and direct evidence for localization, *Geophys. Res. Lett.*, *24*(18), 2271-2274, doi: 10.1029/97GL02355.
- Angelopoulos, V., et al. (1996), Multipoint analysis of a bursty bulk flow event on April 11, 1985, *J. Geophys. Res.*, *101*(A3), 4967-4989, doi:10.1029/95JA02722.

- Ashour-Abdalla, M., and C. F. Kennel (1978), Nonconvective and convective electron cyclotron harmonic instabilities, *J. Geophys. Res.*, 83(A4), 1531-1543.
- Ashour-Abdalla, M., C.F. Kennel, and W. Livesey (1979), A parametric study of electron multiharmonic instabilities in the magnetosphere, *J. Geophys. Res.*, 84(A11), 6540-6546, doi:10.1029/JA084iA11p06540.
- Auster, H. U., et al. (2008), The THEMIS fluxgate magnetometer, *Space Sci. Rev.*, 141, 235-264, doi:10.1007/s11214-008-9365-9.
- Belmont, G., D. Fontaine, and P. Canu (1983), Are equatorial electron cyclotron waves responsible for diffuse auroral electron precipitation?, *J. Geophys. Res.*, 88(A11), 9163-9170, doi:10.1029/JA088iA11p09163.
- Birn, J., M. F. Thomsen, J. E. Borovsky, G. D. Reeves, D. J. McComas, and R. Belian (1997a), Characteristic plasma properties during dispersionless substorm injections at geosynchronous orbit, *J. Geophys. Res.*, 102(A2), 2309-2324, doi:10.1029/96JA02870.
- Birn, J., M. F. Thomsen, J. E. Borovsky, G. D. Reeves, D. J. McComas, R. D. Belian, and M. Hesse (1997b), Substorm ion injections: Geosynchronous observations and test particle orbits in three-dimensional dynamic MHD fields, *J. Geophys. Res.*, 102(A2), 2325-2341, doi:10.1029/96JA03032.
- Birn, J., M. F. Thomsen, J. E. Borovsky, G. D. Reeves, D. J. McComas, R. D. Belian, and M. Hesse (1998), Substorm electron injections: Geosynchronous observations and test particle simulations, *J. Geophys. Res.*, 103(A5), 9235-9248, doi:10.1029/97JA02635.

- Bonnell, J. W., F. S. Mozer, G. T. Delory, A. J. Hull, R. Abiad, R. E. Ergun, C. M. Cully, V. Angelopoulos, and P. R. Harvey (2008), The Electric Field Instrument (EFI) for THEMIS, *Space Sci. Rev.*, *141*, 303-341, doi:10.1007/s11214-008-9469-2.
- Bortnik, J., L. Chen, W. Li, R. M. Thorne, and R. B. Horne (2011a), Modeling the evolution of chorus waves into plasmaspheric hiss, *J. Geophys. Res.*, *116*, A08221, doi:10.1029/2011JA016499.
- Bortnik, J., L. Chen, W. Li, R. M. Thorne, N. P. Meredith, and R. B. Horne (2011b), Modeling the wave power distribution and characteristics of plasmaspheric hiss, *J. Geophys. Res.*, *116*, A12209, doi:10.1029/2011JA016862.
- Chen, L., W. Li, J. Bortnik, and R. M. Thorne (2012), Amplification of whistler-mode hiss inside the plasmasphere, *Geophys. Res. Lett.*, *39*, L08111, doi:10.1029/2012GL051488.
- Chen, M. W., and M. Schulz (2001a), Simulations of storm time diffuse aurora with plasmashet electrons in strong pitch angle diffusion, *J. Geophys. Res.*, *106*(A2), 1873-1886, doi:10.1029/2000JA000161.
- Chen, M. W., and M. Schulz (2001b), Simulations of diffuse aurora with plasma sheet electrons in pitch angle diffusion less than everywhere strong, *J. Geophys. Res.*, *106*(A12), 28,949-28,966, doi:10.1029/2001JA000138.
- Cully, C. M., R. E. Ergun, K. Stevens, A. Nammari, and J. Westfall (2008), The THEMIS digital fields board, *Space Sci. Rev.*, *141*, 343-355, doi:10.1007/s11214-008-9417-1.

- Dungey, J. W. (1961), Interplanetary magnetic field and the auroral zones, *Phys. Rev. Letts.*, 6, 47-48.
- Eather, R. H., and S. B. Mende (1972), Systematics in auroral energy spectra, *J. Geophys. Res.*, 77(4), 660-673, doi:10.1029/JA077i004p00660.
- Fontaine, D., and M. Blanc (1983), A theoretical approach to the morphology and the dynamics of diffuse auroral zones, *J. Geophys. Res.*, 88(A9), 7171-7184.
- Gabrielse, C., V. Angelopoulos, A. Runov, and D. L. Turner (2012), The effects of transient, localized electric fields on equatorial electron acceleration and transport toward the inner magnetosphere, *J. Geophys. Res.*, 117, A10213, doi:10.1029/2012JA017873.
- Gabrielse, C., V. Angelopoulos, A. Runov, and D. L. Turner (2014), Statistical characteristics of particle injections throughout the equatorial magnetotail, *J. Geophys. Res. Space Physics*, 119, doi:10.1002/2013JA019638.
- Gendrin, R. (1981), General relationships between wave amplification and particle diffusion in a magnetoplasma, *Rev. Geophys.*, 19(1), 171-184, doi:10.1029/RG019i001p00171.
- Gilson, M. L., J. Raeder, E. Donovan, Y. S. Ge, L. Kepko (2012), Global simulation of proton precipitation due to field line curvature during substorms, *J. Geophys. Res.*, 117, A05216, doi:10.1029/2012JA017562.
- Hardy, D. A., M. S. Gussenhoven, and E. Holeman (1985), A statistical model of auroral electron precipitation, *J. Geophys. Res.*, 90(A5), 4229-4248, doi:10.1029/JA090iA05p04229.

- Hardy, D. A., M. S. Gussenhoven, and D. Brautigam (1989), A statistical model of auroral ion precipitation, *J. Geophys. Res.*, 94, 370-392, doi:10.1029/JA094iA01p00370.
- Harris, E. G. (1962), On a plasma sheath separating regions of oppositely directed magnetic field, *Nuovo Cimento*, 23, 115-121.
- Horne, R. B. (1989), Path-integrated growth of electrostatic waves: The generation of terrestrial myriametric radiation, *J. Geophys. Res.*, 94(A7), 8895-8909, doi:10.1029/JA094iA07p08895.
- Horne, R. B., R. M. Thorne, N. P. Meredith, and R. R. Anderson (2003), Diffuse auroral electron scattering by electron cyclotron harmonic and whistler mode waves during an isolated substorm, *J. Geophys. Res.*, 108(A7), 1290, doi:10.1029/2002JA009736.
- Horne, R. B., and R. M. Thorne (2000), Electron pitch angle diffusion by electrostatic electron cyclotron harmonic waves: The origin of pancake distributions, *J. Geophys. Res.*, 105(A3), 5391-5402.
- Horne, R. B., and R. M. Thorne (1997), Wave heating of He<sup>+</sup> by electromagnetic ion cyclotron waves in the magnetosphere: Heating near the H<sup>+</sup>-He<sup>+</sup> bi-ion resonance frequency, *J. Geophys. Res.*, 102, 11457-11471, doi:10.1029/97JA00749.
- Kennel, C. F. (1969), Consequences of a magnetospheric plasma, *Rev. Geophys.*, 7, 379-419.
- Kennel, C., F. Scarf, R. Fredricks, J. McGehee, and F. Coroniti (1970), VLF electric field observations in the magnetosphere, *J. Geophys. Res.*, 75(31), 6136-6152.

- Khazanov, G. V., A. Glozer, and E. W. Himwich (2014), Magnetosphere-ionosphere energy interchange in the electron diffuse aurora, *J. Geophys. Res. Space Physics*, *119*, 171-184, doi:10.1002/2013JA019325.
- Kivelson, M. G., and C. T. Russell (1995), *Introduction to space physics*, Cambridge University Press, Cambridge.
- Konradi, A. (1966), Electron and proton fluxes in the tail of the magnetosphere, *J. Geophys. Res.*, *71*(9), 2317-2325, doi:10.1029/JZ071i009p02317.
- Koons, H. C., and J. L. Roeder (1990), A survey of equatorial magnetospheric wave activity between 5 and 8  $R_E$ , *Planet. Space Sci.*, *38*(10), 1335-1341, doi:10.1016/0032-0633(90)90136-E.
- LeContel, O., et al. (2008), First results of the THEMIS searchcoil magnetometers, *Space Sci. Rev.*, doi:10.1007/s11214-008-9371-y.
- Li, S.-S., V. Angelopoulos, A. Runov, X.-Z. Zhou, J. McFadden, D. Larson, J. Bonnell, and U. Auster (2011), On the force balance around dipolarization fronts within bursty bulk flows, *J. Geophys. Res.*, *116*, A00I35, doi:10.1029/2010JA015884.
- Li, W., R. M. Thorne, V. Angelopoulos, J. W. Bonnell, J. P. McFadden, C. W. Carlson, O. LeContel, A. Roux, K. H. Glassmeier, and H. U. Auster (2009a), Evaluation of whistler-mode chorus intensification on the nightside during an injection event observed on the THEMIS spacecraft, *J. Geophys. Res.*, *114*, A00C14, doi:10.1029/2008JA013554.

- Li, W., R. M. Thorne, V. Angelopoulos, J. Bortnik, C. M. Cully, B. Ni, O. LeContel, A. Roux, U. Auster, and W. Magnes (2009b), Global distribution of whistler-mode chorus waves observed on the THEMIS spacecraft, *Geophys. Res. Lett.*, *36*, L09104, doi:10.1029/2009GL037595.
- Li, W., J. Bortnik, R. M. Thorne, and V. Angelopoulos (2011), Global distribution of wave amplitudes and wave normal angles of chorus waves using THEMIS wave observations, *J. Geophys. Res.*, *116*, A12205, doi:10.1029/2011JA017035.
- Li, W., et al. (2010), THEMIS analysis of observed equatorial electron distributions responsible for the chorus excitation, *J. Geophys. Res.*, *115*, A00F11, doi:10.1029/2009JA014845.
- Liang, J., B. Ni, E. Spanswick, M. Kubyshkina, E. F. Donovan, V. M. Uritsky, R. M. Thorne, and V. Angelopoulos (2011), Fast earthward flows, electron cyclotron harmonic waves, and diffuse auroras: Conjunctive observations and a synthesized scenario, *J. Geophys. Res.*, *116*, A12220, doi:10.1029/2011JA017094.
- Liu, J., V. Angelopoulos, A. Runov, and X.-Z. Zhou (2013), On the current sheets surrounding dipolarizing flux bundles in the magnetotail: The case for wedgelets, *J. Geophys. Res. Space Physics*, *118*, 2000-2020, doi: 10.1002/jgra.50092.
- Lyons, L. R., and R. M. Thorne (1973), Equilibrium structure of radiation belt electrons, *J. Geophys. Res.*, *78*(13), 2142-2149, doi:10.1029/JA078i013p02142.
- Lyons, L. (1974), Electron diffusion driven by magnetospheric electrostatic waves, *J. Geophys. Res.*, *79*(4), 575-580.

- Mauk, B. H., and C.-I. Meng (1983), Characterization of geostationary particle signatures based on the 'Injection Boundary' Model, *J. Geophys. Res.*, 88(A4), 3055-3071, doi:10.1029/JA088iA04p03055.
- Mauk, B. H., N. J. Fox, S. G. Kanekal, R. L. Kessel, D. G. Sibeck, and A. Ukhorskiy (2012), Science Objectives and Rationale for the Radiation Belt Storm Probes Mission, *Space Sci. Rev.*, 1-15, doi:10.1007/s11214-012-9908-y.
- McFadden, J. P., C. W. Carlson, D. Larson, M. Ludlam, R. Abiad, B. Elliott, P. Turin, M. Marckwordt, and V. Angelopoulos (2008), The THEMIS ESA Plasma Instrument and In-flight Calibration, *Space Sci. Rev.*, 141, 277-302, doi:10.1007/s11214-008-9440-2.
- Meng, C.-I., B. Mauk, and C. McIlwain (1979), Electron precipitation of evening diffuse aurora and its conjugate electron fluxes near the magnetospheric equator, *J. Geophys. Res.*, 84(A6), 2545-2558, doi:10.1029/JA084iA06p02545.
- Meredith, N. P., R. B. Horne, R. M. Thorne, D. Summers, and R. R. Anderson (2004), Substorm dependence of plasmaspheric hiss, *J. Geophys. Res.*, 109, A06209, doi:10.1029/2004JA010387.
- Meredith, N. P., R. B. Horne, R. H. A. Iles, R. M. Thorne, D. Heynderickx, and R. R. Anderson (2002), Outer zone relativistic electron acceleration associated with substorm-enhanced whistler mode chorus, *J. Geophys. Res.*, 107(A7), 1144, doi:10.1029/2001JA900146.
- Meredith, N. P., R. B. Horne, R. M. Thorne, and R. R. Anderson (2009), Survey of upper band chorus and ECH waves: Implications for the diffuse aurora, *J. Geophys. Res.*, 114, A07218, doi:10.1029/2009JA014230.

- Meredith, N. P., R. B. Horne, A. D. Johnstone, and R. R. Anderson (2000), The temporal evolution of electron distributions and associated wave activity following substorm injections in the inner magnetosphere, *J. Geophys. Res.*, *105*(A6), 12907-12917, doi:10.1029/2000JA900010.
- Moore, T. E., R. L. Arnoldy, J. Feynman, and D. A. Hardy (1981), Propagating substorm injection fronts, *J. Geophys. Res.*, *86*, 6713-6726, doi:10.1029/JA086iA08p06713.
- Nakamura, R., et al. (2002), Motion of the dipolarization front during a flow burst event observed by Cluster, *Geophys. Res. Lett.*, *29*(20), 1942, doi:10.1029/2002GL015763.
- Nakamura, R., et al. (2004), Spatial scale of high-speed flows in the plasma sheet observed by Cluster, *Geophys. Res. Lett.*, *31*, L09804, doi:10.1029/2004GL019558.
- Nakamura, R., W. Baumjohann, R. Schödel, M. Brittnacher, V. A. Sergeev, M. Kubyshkina, T. Mukai, and K. Liou (2001), Earthward flow bursts, auroral streamers, and small expansions, *J. Geophys. Res.*, *106*(A6), 10791-10802, doi:10.1029/2000JA000306.
- Newell, P. T., T. Sotirelis, and S. Wing (2009), Diffuse, monoenergetic, and broadband aurora: The global precipitation budget, *J. Geophys. Res.*, *114*, A09207, doi:10.1029/2009JA014326.
- Newell, P. T., T. Sotirelis, and S. Wing (2010), Seasonal variations in diffuse, monoenergetic, and broadband aurora, *J. Geophys. Res.*, *115*, A03216, doi:10.1029/2009JA014805.
- Newell, P. T., T. Sotirelis, K. Liou, C.-I. Meng, and F. J. Rich (2007), A nearly universal solar wind-magnetosphere coupling function inferred from 10 magnetospheric state variables, *J. Geophys. Res.*, *112*, A01206, doi:10.1029/2006JA012015.

- Ni, B., R. M. Thorne, Y. Y. Shprits, and J. Bortnik (2008), Resonant scattering of plasma sheet electrons by whistler-mode chorus: Contribution to diffuse auroral precipitation, *Geophys. Res. Lett.*, *35*, L11106, doi:10.1029/2008GL034032.
- Ni, B., R. Thorne, J. Liang, V. Angelopoulos, C. Cully, W. Li, X. Zhang, M. Hartinger, O. Le Contel, and A. Roux (2011a), Global distribution of electrostatic electron cyclotron harmonic waves observed on THEMIS, *Geophys. Res. Lett.*, *38*, L17105, doi:10.1029/2011GL048793.
- Ni, B., R. M. Thorne, R. B. Horne, N. P. Meredith, Y. Y. Shprits, L. Chen, and W. Li (2011b), Resonant scattering of plasma sheet electrons leading to diffuse auroral precipitation: 1. Evaluation for electrostatic electron cyclotron harmonic waves, *J. Geophys. Res.*, *116*, A04218, doi:10.1029/2010JA016232.
- Ni, B., R. M. Thorne, N. P. Meredith, R. B. Horne, and Y. Y. Shprits (2011c), Resonant scattering of plasma sheet electrons leading to diffuse auroral precipitation: 2. Evaluation for whistler mode chorus waves, *J. Geophys. Res.*, *116*, A04219, doi:10.1029/2010JA016233.
- Ni, B., R. M. Thorne, Y. Y. Shprits, K. G. Orlova, and N. P. Meredith (2011d), Chorus-driven resonant scattering of diffuse auroral electrons in nondipolar magnetic fields, *J. Geophys. Res.*, *116*, A06225, doi:10.1029/2011JA016453.
- Ni, B., J. Liang, R. M. Thorne, V. Angelopoulos, R. B. Horne, M. Kubyshkina, E. Spanswick, E. F. Donovan, and D. Lummerzheim (2012a), Efficient diffuse auroral electron scattering by electrostatic electron cyclotron harmonic waves in the outer magnetosphere: A detailed case study, *J. Geophys. Res.*, *117*, A01218, doi:10.1029/2011JA017095.

- Ni, B., R. M. Thorne, and Q. Ma (2012b), Bounce-averaged Fokker-Planck diffusion equation in non-dipolar magnetic fields with applications to the Dungey magnetosphere, *Ann. Geophys.*, *30*, 733-750, doi:10.5194/angeo-30-733-2012.
- Nishimura, Y., L. Lyons, S. Zou, V. Angelopoulos, and S. Mende (2010), Substorm triggering by new plasma intrusion: THEMIS all-sky imager observations, *J. Geophys. Res.*, *115*, doi:10.1029/2009JA015166.
- Ohtani, S., M. A. Shay, and T. Mukai (2004), Temporal structure of the fast convective flow in the plasma sheet: Comparison between observations and two-fluid simulations, *J. Geophys. Res.*, *109*, 3210, doi:10.1029/2003JA010002.
- Petrinec, S. M., D. L. Chenette, J. Mabilia, M. A. Rinaldi, and W. L. Imhof (1999), Statistical X ray auroral emissions-PIXIE observations, *Geophys. Res. Lett.*, *26*(11), 1565-1568, doi:10.1029/1999GL900295.
- Roeder, J. L., and H. C. Koons (1989), A survey of electron cyclotron waves in the magnetosphere and the diffuse auroral electron precipitation, *J. Geophys. Res.*, *94*(A3), 2529-2541.
- Roux, A., O. Le Contel, C. Coillot, A. Bouabdellah, B. de la Porte, D. Alison, S. Ruocco, and M. C. Vassal (2008), The search coil magnetometer for THEMIS, *Space Sci. Rev.*, *141*, 265-275, doi:10.1007/s11214-008-9455-8.
- Runov, A., V. Angelopoulos, X.-Z. Zhou, X.-J. Zhang, S. Li, F. Plaschke, and J. Bonnell (2011a), A THEMIS multicase study of dipolarization fronts in the magnetotail plasma sheet, *J. Geophys. Res.*, *116*, A05216, doi:10.1029/2010JA016316.

- Runov, A., V. Angelopoulos, M. I. Sitnov, V. A. Sergeev, J. Bonnell, J. P. McFadden, D. Larson, K.-H. Glassmeier, and U. Auster (2009), THEMIS observations of an earthwardpropagating dipolarization front, *Geophys. Res. Lett.*, *36*, L14106, doi:10.1029/2009GL038980.
- Runov, A., et al. (2011b), Dipolarization fronts in the magnetotail plasma sheet, *Planet. Space Sci.*, *59*, 517-525, doi:10.1016/j.pss.2010.06.006.
- Santolik, O., D. A. Gurnett, J. S. Pickett, M. Parrot, and N. Cornilleau-Wehrin (2003), Spatio-temporal structure of storm-time chorus, *J. Geophys. Res.*, *108*(A7), 1278, doi:10.1029/2002JA009791.
- Sarris, E.T., S. M. Krimigis, and T. P. Armstrong (1976), Observations of magnetospheric bursts of high-energy protons and electrons at 35 with Imp 7, *J. Geophys. Res.*, *81*(13), 2341-2355, doi:10.1029/JA081i013p02341.
- Schulz, M., and L. J. Lanzerotti (1974), *Particle diffusion in the radiation belts*, Physics and Chemistry in Space, Springer, New York.
- Sergeev, V., V. Angelopoulos, S. Apatenkov, J. Bonnell, R. Ergun, R. Nakamura, J. McFadden, D. Larson, and A. Runov (2009), Kinetic structure of the sharp injection/dipolarization front in the flow-braking region, *Geophys. Res. Lett.*, *36*, L21105, doi:10.1029/2009GL040658.
- Sergeev, V. A., E. Sazhina, N. Tsyganenko, J. Lundblad, and F. Soraas (1983), Pitch-angle scattering of energetic protons in the magnetotail current sheet as the dominant source of their isotropic precipitation into the nightside ionosphere, *Planet. Space Sci.*, *31*, 1147-1155.

- Shprits, Y. Y., and B. Ni (2009), Dependence of the quasi-linear scattering rates on the wave normal distribution of chorus waves, *J. Geophys. Res.*, *114*, A11205, doi:10.1029/2009JA014223.
- Sibeck, D. G., and V. Angelopoulos (2008), THEMIS science objectives and mission phases, *Space Sci Rev.*, *141*, 35-59, doi:10.1007/s11214-008-9393-5.
- Summers, D., R. M. Thorne, and F. Xiao (1998), Relativistic theory of wave-particle resonant diffusion with application to electron acceleration in the magnetosphere, *J. Geophys. Res.*, *103*(A9), 20487-20500, doi:10.1029/98JA01740.
- Tsurutani, B. T., and E. J. Smith (1974), Postmidnight chorus: A substorm phenomenon, *J. Geophys. Res.*, *79*(1), 118-127, doi:10.1029/JA079i001p00118.
- Tao, X., R. M. Thorne, W. Li, B. Ni, N. P. Meredith, and R. B. Horne (2011), Evolution of electron pitch-angle distributions following injection from the plasma sheet, *J. Geophys. Res.*, *116*, A04229, doi:10.1029/2010JA016245.
- Thorne, R. M., B. Ni, X. Tao, R. B. Horne, and N. P. Meredith (2010), Scattering by chorus waves as the dominant cause of diffuse auroral precipitation, *Nature*, *467*, 943-946, doi:10.1038/nature09467.
- Tsyganenko, N. A. (1989), A Magnetospheric Magnetic Field Model with a Warped Tail Current Sheet, *Planet. Space Sci.*, *37*, 5-20.
- Tsyganenko, N. A., and D. P. Stern (1996), Modeling the global magnetic field of the large-scale Birkeland current systems, *J. Geophys. Res.*, *101*(A12), 27187-27198, doi:10.1029/96JA02735.
- Walker, A. D. M. (1993), *Plasma Waves in the Magnetosphere*, Springer-Verlag, New York.

- Xiao, F., Z. Su, H. Zheng, and S. Wang (2009), Modeling of outer radiation belt electrons by multidimensional diffusion process, *J. Geophys. Res.*, *114*, A03201, doi:10.1029/2008JA013580.
- Young, T. S. T., J. D. Callen, and J. E. McCune (1973), High-frequency electrostatic waves in the magnetosphere, *J. Geophys. Res.*, *78*(7), 1082-1099, doi:10.1029/JA078i007p01082.
- Zhang, X.-J., V. Angelopoulos, A. Runov, X. Zhou, J. Bonnell, J. P. McFadden, D. Larson, and U. Auster (2011), Current carriers near dipolarization fronts in the magnetotail: A THEMIS event study, *J. Geophys. Res.*, *116*, doi:10.1029/2010JA015885.
- Zhang, X.-J., V. Angelopoulos, B. Ni, R. M. Thorne, and R. B. Horne (2013), Quasi-steady, marginally unstable electron cyclotron harmonic wave amplitudes, *J. Geophys. Res. Space Physics*, *118*, 3165-3172, doi:10.1002/jgra.50319.
- Zhang, X.-J., and V. Angelopoulos (2014), On the relationship of electrostatic cyclotron harmonic emissions with electron injections and dipolarization fronts, *J. Geophys. Res. Space Physics*, *119*, doi:10.1002/2013JA019540.